Non-linear static analysis of multilayered 2D beams with various contact between layers

Škec, Leo

Doctoral thesis / Disertacija

2014

Degree Grantor / Ustanova koja je dodijelila akademski / stručni stupanj: **University of Rijeka, Faculty of Civil Engineering / Sveučilište u Rijeci, Građevinski fakultet**

Permanent link / Trajna poveznica: https://urn.nsk.hr/urn:nbn:hr:188:342651

Rights / Prava: Attribution 4.0 International/Imenovanje 4.0 međunarodna

Download date / Datum preuzimanja: **2024-05-22**

UNIVERSITY OF RIJEKA

FACULTY OF CIVIL ENGINEERING

Leo Škec

NON-LINEAR STATIC ANALYSIS OF MULTILAYERED 2D BEAMS WITH VARIOUS CONTACT CONDITIONS BETWEEN LAYERS

DOCTORAL THESIS

Rijeka, 2014

UNIVERSITY OF RIJEKA

FACULTY OF CIVIL ENGINEERING

Leo Škec

NON-LINEAR STATIC ANALYSIS OF MULTILAYERED 2D BEAMS WITH VARIOUS CONTACT CONDITIONS BETWEEN LAYERS

DOCTORAL THESIS

Supervisor: prof. dr. sc. Gordan Jelenić

Rijeka, 2014

Mentor: prof. dr. sc. Gordan Jelenić

Doktorski rad obranjen je dana ————————————————————u/na

——

pred povjerenstvom u sastavu:

1. prof. dr. sc. Nenad Bićanić, Sveučilište u Rijeci, Građevinski fakultet, predsjednik povjerenstva

2. prof. dr. sc. Igor Planinc, Univerza v Ljubljani, Fakulteta za gradbeništvo in geodezijo, član

3. prof. dr. sc. Adriana Bjelanović, Sveučilište u Rijeci, Građevinski fakultet, član

Acknowledgements

Veliko hvala mojoj obitelji i Albi na beskrajnoj podršci, ljubavi i inspiraciji.

Hvala svim kolegama na prijateljstvu i suradnji, a posebno Gordanu, mentoru velikog znanja i još većeg srca, bez kojeg ovaj rad nikada ne bi ugledao svjetlo dana.

Ovaj doktorski rad posvećen je mojoj noni Meri.

Abstract

In this thesis different aspects of behaviour of layered structures are analysed and numerically modelled using beam finite elements. Three models for the layered beams are presented. All the models are expressed in a general form for an arbitrary number of layers and each layer can have individual geometrical and material properties, boundary conditions and applied loading. The first of them is an analytical model for a multi-layer beam with compliant interconnections. Kinematic and constitutive equations are linear and various interlayer contact conditions are considered (no contact, rigid interconnection, interlayer slip and/or interlayer uplift). The second model is a finite element formulation for geometrically exact multi-layer beams with a rigid interconnection. This model proves to be very efficient for modelling homogeneous structures via multi-layer beams, especially for thick beam-like structures, where cross-sectional warping is more pronounced. The third model deals with mixed-mode delamination in multi-layer beams. A damage-type bi-linear constitutive law for the interconnection is implemented for an interface finite element sandwiched between two layers. Numerical examples are presented for all models and the results of the tests are compared to representative results from the literature.

Keywords: layered beams, analytical solution, non-linear analysis, mixed-mode delamination.

Sažetak

U ovoj disertaciji obrađeni su različiti aspekti ponašanja slojevitih nosača modeliranih grednim konačnim elementima. Predstavljena su tri modela za proračun slojevitih greda. Svi predstavljeni modeli zapisani su u općenitom obliku za proizvoljan broj slojeva, gdje svaki sloj može imati zasebne geometrijske i materijalne karakteristike te opterećenje i rubne uvjete.

Prvi je analitički model za višeslojnu gredu s popustljivim kontaktom među slojevima. Kinematičke i konstitutivne jednadžbe su linearne te su u obzir uzeti različiti uvjeti na kontaktu. Tako veza među slojevima može biti apsolutno kruta, omogućavati nezavisno rotiranje jednog sloja u odnosu na drugi, omogućavati klizanje i razmicanje među slojevima ili pak slojevi mogu biti potpuno nepovezani. U numeričkim primjerima istražen je utjecaj materijalnih i geometrijskih parametara osnovnog materijala i kontakta na ponašanje slojevitih greda.

Drugi model predstavlja formulaciju konačnog elementa za geometrijski egzaktnu višeslojnu gredu s krutom vezom među slojevima. Ovaj model se pokazao vrlo efikasnim za modeliranje homogenih nosača koristeći višeslojne grede, posebno u slučaju visokih greda kod kojih je naglašeno vitoperenje poprečnog presjeka. U usporedbi s ravninskim konačnim elementima koji se često koriste za diskretizaciju ravninskih nosača, model višeslojne grede daje usporedivo dobre rezultate koristeći znatno manji broj stupnjeva slobode.

Treći model uvodi raslojavanje u višeslojne grede. Kontaktni konačni element s ugrađenim bilinearnim konstitutivnim zakonom koji uzima u obzir oštećenje umetnut je između grednih konačnih elemenata čime je omogućeno modeliranje problema s odvojenim oblicima (modovima) raslojavanja I i II te mješovitim oblikom raslojavanja. Numerički primjeri pokazuju kako ovakav gredni model, u usporedbi s modelima koji koriste ravninske konačne elemente, daje rezultate usporedive točnosti uz manji broj stupnjeva slobode.

Ključne riječi: slojevite grede, analitičko rješenje, nelinearna analiza, mješovito raslojavanje.

Contents

1 INTRODUCTION

Layered structures appear in many engineering applications as well as in nature and provide an extremely effective means of optimising functional and structural performance of diverse mechanical systems. Fibre-reinforced carbon-composite laminates are a typical example where different laminae are stacked on one another, each one with fibres oriented in a specific direction to provide a composite structure with optimised performance [43]. Examples in nature range from structural geology, e.g. the structure of the Earth itself [58], but also sedimentary rock structures [9], to the morphology of trees and plants [45]. The best example is probably the human body, where skin, blood vessels, cell membranes, to mention just a few, are all made up of thin layers [64].

In civil engineering, the use of composite structures, where two or more components from one or more different materials are used in a single cross section, is very common. The basic idea is to combine the components in such a way that each of them fulfils the function for which its material characteristics are best suited. Due to this optimised performance of their components, the composite systems are economical and have a high load-bearing capacity. Steel-concrete composite beams, wood-steel concrete floors, coupled shear walls, sandwich beams, concrete beams externally reinforced with laminates and many others are all examples of composite structures in civil engineering. The mechanical behaviour of these structures largely depends on the type of connection between the layers, which can be continuous (glue) or discrete (mechanical shear connectors such as nails, screws and bolts). Continuous glued interconnection in comparison with discrete shear connectors is considerably stiffer, but it also provides only a partial interaction between the layers with interlayer slip and uplift [73]. Therefore, a partial interaction has to be taken into consideration in the mechanical analysis of multi-layered structures.

Research and application of layered composite structures in many areas of engineering has increased considerably over the past couple of decades and continues to be a topic of undiminished interest in the computational mechanics community. Modelling such structures can have many different aspects, considering the geometry of the problem, material properties, time-dependence of the applied loading etc.

In the present work, the area of interest is reduced only to plane static problems. Thus, the state of the art for the three-dimensional models and the models which include dynamic effects will not be presented. To model the layered structures, in the present work, beam theory is used, meaning that the geometrical and material properties, the displacements and rotations, the boundary conditions and the applied loading, are reduced to a single reference axis. This concept results in a one-dimensional formulation, where all the basic variables vary only with respect to a co-ordinate along the reference axis. In comparison with two- and three-dimensional theories (see [67]), beam theory is simpler. It is true that it also neglects a number of planar and spatial effects, but, in many applications, the beam models offer a satisfactory accuracy and less computational effort in comparison with more complex 2D or 3D models.

Basic equations defining a layered beam consist of kinematic, constitutive, equilibrium and assembly equations. Kinematic equations define the relationship between the displacements and the strains of the structure, constitutive equations relate the internal forces (stress resultants) to the strains, equilibrium equations define the internal-external forces relationship, while in the assembly equations the connection between layers is defined. Kinematic equations for the plane beam problem in the exact (non-linear) form were given by Reissner [48]. If small displacements and rotations in the deformed state are assumed, which is often the case in civil engineering problems, the exact Reissner's equations can be reduced to a linear form, also known as Timoshenko's beam theory [66]. In both Reissner's and Timoshenko's beam theories the strains produced by the shear forces are considered. If they are neglected, Timoshenko's beam theory reduces to Euler-Bernoulli or classical beam theory [10], which is also given in a linear form. The constitutive equations can be also given in linear or non-linear form.

2

Only in case when both kinematic and constitutive equations as well as the equilibrium equations are given in linear form the solution of the problem can be obtained analytically. In case of geometrical or/and material non-linearity, the solution can be obtained only numerically. The method which is used most often for the problems of layered structures is the finite element method (*FEM*). Since the layered structures can have two or more layers, the layered beam models from the literature are usually given for two-, three-(sandwich) or multi-layer beams. Conditions at the interconnection of a layered beam are fundamentally important for the model. Interconnection can be defined only in discrete points, or it can be modelled as continuous, which can be either rigid or allow for interlayer slip and/or uplift.

In this thesis three different models for multi-layer beams with arbitrary number of layers and zero-thickness interlayer interface are proposed. The first model deals with linear kinematic and constitutive relations for each layer and interface enables an analytical solution. The second model focuses on geometrical non-linearity for the case of rigid connection between the layers, while the third model introduces material non-linearity at the interconnection. Since analytical solutions for the last two models cannot be obtained, a finite element formulation is proposed. A brief introduction to each of these parts with corresponding state of the art is presented next.

In the fist part of the thesis, an analytical solution for a multi-layer beam with compliant interconnections is presented. For different conditions at the interconnections (completely rigid interconnection, rigid interconnection allowing for individual rotations of layers, interlayer slip, interlayer slip and uplift) considered, four basic models with their systems of differential equations are obtained. Restraining the interlayer degrees of freedom (interlayer slip, uplift and rotation) reduces the system of differential equations, which are solved considering the corresponding boundary conditions. The number of layers is arbitrary, and each layer can have individual material and geometrical properties, as well as its own applied loading. The results for this model are presented in [72].

Considering the analytical solutions for layered beams, to this end, a large number of references exist. Among many others, a few examples are given here. McCutheon [37] proposed a simple procedure for computing the composite stiffness of a wood bending member with sheathing attached non-rigidly to one or both edges. Girhammar and Pan [21] proposed an analytical solution for a geometrically and materially linear two-layer composite beam with interlayer slip using the Bernoulli beam theory. Schnabl *et al.* [53] dealt with buckling of such beams, while Schnabl *et al.* [54, 57] and Kryžanowski *et al.* [35] used the Timoshenko beam theory for the two-layer beams/columns. In addition to interlayer slip, interlayer was introduced to a two-layer beam model by Nguyen *et al.* [39], Adekola [1], Gara [20], Ranzi *et al.* [46, 47] and Kroflič it et al. [32]. More recently, Schnabl and Planinc [55] applied both interlayer slip and uplift in the buckling analysis of two-layer composite columns where transverse shear deformation is also taken into consideration.

For the sandwich beam model with partial interaction Schnabl *et al.* [56] proposed an analytical solution, while Attard and Hunt [4] presented a hyperelastic formulation of a sandwich column buckling where interlayer slip and uplift were neglected. Frostig [19] presented the classical and the high-order computational models of unidirectional sandwich panels with incompressible and compressible cores.

An analytical model where the effect of interlayer slip and uplift on mechanical behaviour of layered structures is neglected was proposed by Bareisis [6]. Sousa Jr. *et al.* [63] proposed an analytical solution for geometrically and materially linear multi-layer beams allowing for interlayer slip, while the aforementioned model proposed by Škec *et al.* [72] introduced both the slip and the interlayer uplift.

In the second part of the thesis, a geometrically exact (non-linear) finite element formulation for a multi-layer beam with a rigid interconnection is presented. Interlayer slip and uplift are not allowed, but each layer can have individual cross-sectional rotation. Such a formulation is very suitable for modelling beams where cross-sectional warping is pronounced (like thick beams, for example), since the layers' cross-sections, in deformed state, form a piecewise-linear shape, which approximates a warped cross-section. Although this formulation allows for assigning

individual material and geometrical properties for each layer, due to its rigid interconnection, it is more suitable for modelling homogeneous beams, rather than composite beams where interlayer slip (and uplift) are influences that should not be neglected. The results from this model are presented in the work by Škec and Jelenić [71], and the formulation has been later used as a base for a layered reinforced-concrete planar beam finite element models with embedded transversal cracking proposed by Šćulac et al. [70].

Considering the layered beam models with geometrically exact formulation, two-layer models, including material non-linearity and interlayer slip and uplift, were proposed by Kroflič et al. [33, 34]. Vu-Quoc et al. [74] proposed a geometrically exact formulation for sandwich beams with a rigid interlayer connection and a generalization to multi-layered beams [75, 76]. In this formulations the equilibrium equations were derived using the Galerkin projection, in contrast to the principle of virtual work used here [71].

Another important phenomenon in the analysis of layered structures is delamination, which is introduced in the third part of the thesis. Delamination is one of the most prevalent and severe failure modes in layered composite structures, difficult to detect during routine inspections and presents one of the biggest safety challenges that the aerospace industry has been facing in the last decades [14]. Since the finite element method is commonly used to analyse composite structures, it is necessary to incorporate delamination in the FE model to assess the integrity of a damaged structure.

When initially proposed by Barenblatt [7], cohesive zone models (CZMs) provided a radically new approach to the phenomenon of crack propagation, fundamentally different from that of Griffith [22] in that they allowed the fracturing process to be governed by the stress distributed over a finite region around the crack tip, typically named 'the process zone', rather than the stress concentrated at the crack tip. This model allowed the transfer of stresses over the crack provided it remained sufficiently narrow, and could be justified by a variety of physical phenomena taking place in materials during fracture [8]. Ever since Hillerborg et al. [25] made their first FE implementation of the model, CZMs have continued to generate much interest within the computational mechanics research community

reflected by the immense literature in this field published in the last two decades (see e.g. [15, 68, 78] and the references therein).

Obviously, it can be appreciated that to model complex layered structures numerically, along the lines of the cohesive-zone theory, very sophisticated and computationally intense numerical procedures are needed, which are often too computationally expensive to be applicable as every-day design tools in engineering practice.

To bridge the gap between such expensive computational procedures and a desire of the structural analyst to have more effective and engineer-oriented design tools, in this thesis, a finite element formulation for a multi-layer beam with interconnection is presented. Here, the processes of crack occurrence and propagation, damage-type material softening, and eventual delamination are modelled using beam-type finite elements stemming from Reissner's beam theory [48] to describe structural layers and interface elements with bi-directional stiffness [2]. Beam elements are more intuitive than solid elements and in geometrically linear analysis Reissner's theory corresponds to the well-known Timoshenko theory which forms a part of every engineering education, and their behaviour is expected to be more familiar to the analyst. More importantly, they make use of a smaller number of degrees of freedom eventually reducing the overall computational burden. Finally, beam elements can be used with very good accuracy for problems such as double cantilever beam (DCB) and peel tests [31], which are widely used to characterise fracture as discussed above. The results presented in the third part of the thesis, show that modelling delamination using beam finite elements, rather than 2D plane-stress finite elements, is an alternative that should be seriously considered.

In spite of all these arguments, research in damage and delamination using beam finite elements has been rather scarce and, to the best of author's knowledge, has not addressed the dual-mode delamination. In particular, Sankar [51] proposed a geometrically linear laminated shear deformable beam finite element divided into two sublaminates connected by 'damage struts'. Roche and Accorsi [50] developed a geometrically linear finite element for laminated beams based on simplified kinematic assumptions with an additional nodal degree of freedom which is activated when the element contains delamination. Eijo *et al.* [18] proposed a beam model

6

for mode II delamination in geometrically linear laminated beams assuming an isotropic non-linear material behaviour and a piecewise linear (zigzag) displacement functions to introduce the interlayer slip into the displacement field. In the work of Kroflič *et al.* [34], geometrically exact two-layer beam finite element with uncoupled non-linear laws of interlayer contact in both tangent and normal directions is presented. In a more theoretical vein, the issues of damage and delamination in continua subject to beam-like kinematic constraints have been investigated very recently by de Morais, who proposed an analytical solution for mode II [16] and mode I delamination [17] in geometrically linear beams with bilinear cohesive law, and by Harvey and Wang, who presented analytical theories for the mixed-mode partitioning [77] of one-dimensional delamination in laminated composite beams within the context of both Euler and Timoshenko beam theories [23].

Each part of this thesis presents a procedure for the analysis of multi-layered beams with different formulation of the governing equations. Depending on the form of kinematic and constitutive equations, linear and non-linear solution procedures are presented. The final chapter of the thesis gives the conclusions and the guidelines for the future work.

2 LINEAR ANALYSIS OF MULTI-LAYER BEAMS WITH COMPLIANT INTERCONNECTIONS

2.1 Introduction

In this chapter, analytical models of multi-layer beams with various combinations of contact conditions are presented. The models take into account both inter-layer slip and uplift, different material and geometrical properties of individual layers, different transverse shear deformations of each layer, and different boundary conditions of the layers. The analytical studies are carried out to evaluate the influence of different contact conditions on the static and kinematic quantities. A considerable difference of the results between the models is obtained.

2.2 Problem description

A model of a planar multi-layer beam composed of N layers and $N - 1$ contact planes is studied with the following assumptions:

1. material is linear elastic,

2. displacements, rotations and strains are small,

3. shear strains are taken into account (the Timoshenko beam),

4. normal strains vary linearly over each layer (the Bernoulli hypothesis),

5. friction between the layers is neglected or is taken into account indirectly through the material models of the connection,

6. cross sections are symmetrical with respect to the plane of deformation and remain unchanged in the form and size during deformation,

7. both transverse and longitudinal separations between the layers are possible but they are assumed to be mutually independent and

8. loading of a multi-layer beam is symmetrical with regard to the plane of deformation.

An initially straight, planar, multi-layer beam element of undeformed length L is considered, of which two adjacent layers i and $i+1$ separated by a contact plane α are shown in Fig. 2.1. The beam is placed in the (X, Z) plane of a spatial Cartesian coordinate system with coordinates (X, Y, Z) and unit base vectors $\mathbf{E}_X, \mathbf{E}_Y$, and $\mathbf{E}_Z$. Each layer has its own reference axis which coincides with the layer's centroidal axis. The reference axis of an arbitrary layer i is denoted as x^i in the undeformed configuration and $\overline{x}^i$ in the deformed configuration. The material particles of each layer are indentified by material coordinates x^i, y^i, z^i $(i = 1, 2, \ldots, N)$. Besides, the material coordinate x^i of each layer is identical with its reference axis. In addition, it is assumed that $x^1 = x^2 = \ldots = x^N = x$.
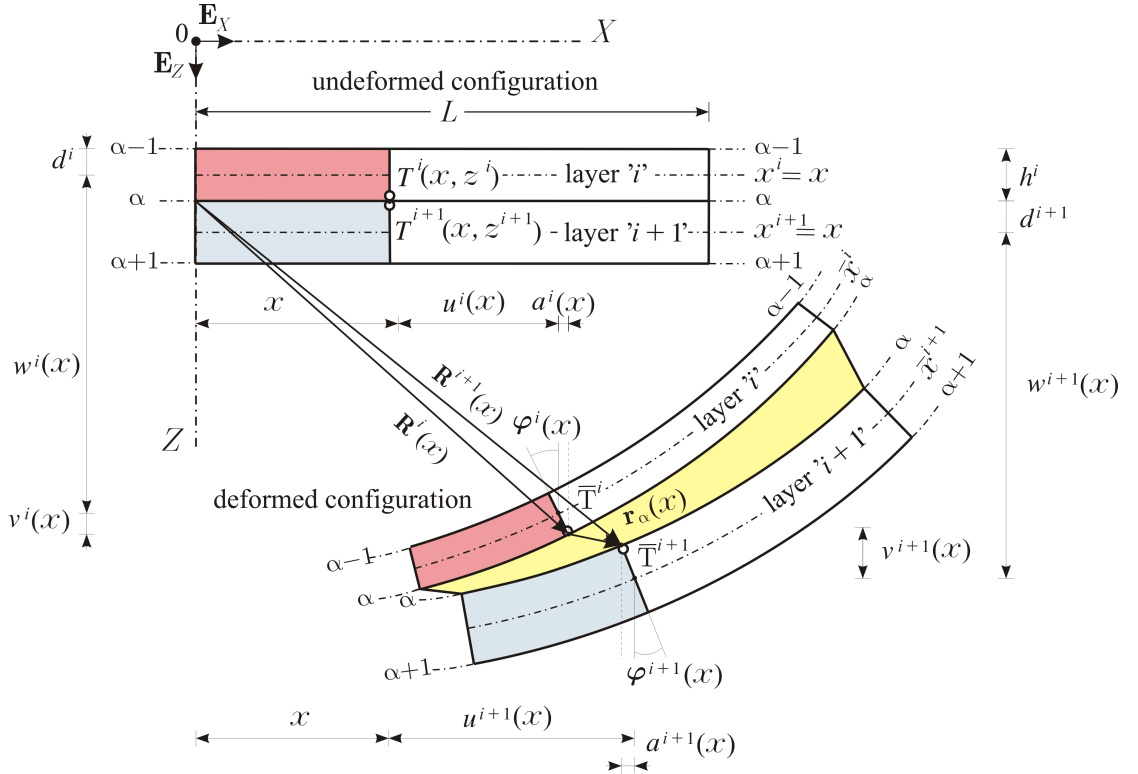
FIGURE 2.1: Undeformed and deformed configuration of a multi-layer beam.

The multi-layer beam element is subjected to the action of the distributed load $\mathbf{p}^i$ $= p_X^i \mathbf{E}_X + p_Z^i \mathbf{E}_Z$ and the distributed moment $\mathbf{m}^i = m_Y^i \mathbf{E}_Y$ along the length of each layer. A differential segment of length dx of layer i with the applied loading with respect to the reference axis, the cross-sectional equilibrium forces and bending moments, and contact tractions in tangential and normal directions $p_{t,\alpha-1}, p_{t,\alpha}$, $p_{n,\alpha-1}$, and $p_{n,\alpha}$ is shown in Fig. 2.2.
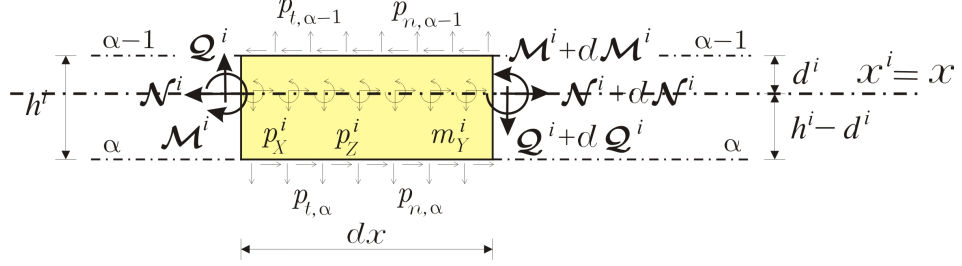
FIGURE 2.2: Internal forces and interlayer tractions in a multi-layer beam element.

External point forces and moments can be applied only at the ends of the multi-layer beam element and are introduced via boundary conditions. The system of linear governing equations of the multi-layer beam is obtained using a consistent linearization of governing non-linear equations of a Reissner planar beam in the undeformed initial configuration [48]. Thus, the linearised system of governing equations consists of equilibrium and constitutive equations with accompanying boundary conditions of each layer and the constraining equations that assemble each layer into a multi-layer beam.

2.3 Governing equations

2.3.1 Kinematic equations

The kinematic equations listed below define the relationship between the displacements and strains for an arbitrary layer i:

$$u^{i\prime} - \varepsilon^i = 0,$$
$$w^{i\prime} + \varphi^i - \gamma^i = 0, \qquad (2.1)$$
$$\varphi^{i\prime} - \kappa^i = 0.$$

In Eqs (2.1), u^i, w^i, φ^i denote the components of the displacement and rotation vector of the ith layer at the reference axis $x^i = x$ with respect to the base vectors $\mathbf{E}_X, \mathbf{E}_Y$, and $\mathbf{E}_Z$, respectively. The prime $(\bullet)'$ denotes the derivative with respect to x. The extensional strain of the reference axis of the ith layer, the shear and the bending strain of the corresponding cross section of the ith layer are denoted by ε^i, γ^i, and κ^i, respectively.

2.3.2 Equilibrium equations

The relationship between the loads applied on the layer i, the corresponding internal equilibrium forces and the distributed contact tractions are defined by the equilibrium equations derived from Fig. 2.2:

$$
\begin{aligned}
&\mathcal{N}^{i\prime} + p_X^i - p_{t,\alpha-1} + p_{t,\alpha} = 0, \\
&\mathcal{Q}^{i\prime} + p_Z^i - p_{n,\alpha-1} + p_{n,\alpha} = 0, \\
&\mathcal{M}^{i\prime} - \mathcal{Q}^i + m_Y^i + p_{t,\alpha-1}d^i + p_{t,\alpha}(h^i - d^i) = 0,
\end{aligned}
\tag{2.2}
$$

where $\mathcal{N}^i$ and $\mathcal{Q}^i$ represent the axial and shear equilibrium forces while $\mathcal{M}^i$ is the equilibrium bending moment of the ith layer. On the other hand, p_X^i, p_Z^i, and m_Y^i are the distributed loads on i^{th} layer given with respect to the reference axis $x^i = x$. The tangential and the normal interlayer contact tractions on the contact plane α are denoted by $p_{t,\alpha}$ and $p_{n,\alpha}$. On the outer planes of the multi-layer beam $(\alpha = 0$ and $\alpha = N)$ no contact exists, thus

$$
\begin{aligned}
&p_{t,0} = p_{n,0} = 0, \\
&p_{t,N} = p_{n,N} = 0.
\end{aligned}
\tag{2.3}
$$

2.3.3 Constitutive equations

The constitutive internal forces $\mathcal{N}_C^i, \mathcal{Q}_C^i$, and $\mathcal{M}_C^i$ are related to the equilibrium internal forces $\mathcal{N}^i, \mathcal{Q}^i$, and $\mathcal{M}^i$ by the following constitutive equations:

$$
\begin{aligned}
\mathcal{N}^i - \mathcal{N}_C^i &= 0, \\
\mathcal{Q}^i - \mathcal{Q}_C^i &= 0, \\
\mathcal{M}^i - \mathcal{M}_C^i &= 0.
\end{aligned}
\tag{2.4}
$$

In the case of a linear elastic material and when the layer reference axis coincides with its centroidal axis, the constitutive forces are given by the linear relations with respect to ε^i, κ^i, and γ^i [26]:

$$
\begin{aligned}
\mathcal{N}_C^i &= E^i A^i \varepsilon^i = C_1^i \varepsilon^i, \\
\mathcal{Q}_C^i &= k_y^i G^i A^i \gamma^i = C_2^i \gamma^i, \\
\mathcal{M}_C^i &= E^i J^i \kappa^i = C_3^i \kappa^i.
\end{aligned}
\tag{2.5}
$$

In Eqs (2.5), E^i and G^i are the elastic and shear modulus, A^i denotes the area of the cross section, and J^i is the second moment of area of the ith layer with respect to the reference axis $x^i = x$. The shear coefficient of the cross section of the ith layer is denoted by k_y^i. For rectangular cross sections and isotropic material this coefficient is $5/6$ [12].

2.3.4 Constraining equations

The constraining equations define the conditions by means of which an individual layer i is assembled into a multi-layer beam. When a material point on the contact plane α between layers i and $i+1$ is observed (see Fig. 2.1), it can be identified in the undeformed configuration with points $T^i(x, z^i = h^i - d^i)$ and $T^{i+1}(x, z^{i+1} = -d^i)$, the first one on the lower edge of the upper layer i and the second one on the upper edge of the lower layer $i+1$. In the deformed configuration these two points become separated due to an interlayer separation. Vectors $\mathbf{R}^i(x, z^i = h^i - d^i)$ and $\mathbf{R}^{i+1}(x, z^{i+1} = -d^i)$ determine the position of points $\overline{T}^i$ and $\overline{T}^{i+1}$ in the deformed

configuration:

$$\mathbf{R}^i(x, z^i) = \left(x + u^i(x) + a^i(x, z^i)\right) \mathbf{E}_X + \left(d^i - h^i + w^i(x) + v^i(x, z^i)\right) \mathbf{E}_Z,$$

$$\mathbf{R}^{i+1}(x, z^{i+1}) = \left(x + u^{i+1}(x) - a^{i+1}(x, z^{i+1})\right) \mathbf{E}_X + \left(d^{i+1} + w^{i+1}(x) - v^{i+1}(x, z^{i+1})\right) \mathbf{E}_Z,$$

$$(2.6)$$

where $a^i(x, z^i) = (h^i - d^i) \sin \varphi^i(x)$, $a^{i+1}(x, z^{i+1}) = d^{i+1} \sin \varphi^{i+1}(x)$, $v^i(x, z^i) = (h^i - d^i) \cos \varphi^i(x)$, and $v^{i+1}(x, z^{i+1}) = d^{i+1} \cos \varphi^{i+1}(x)$. Corresponding to the assumption of small displacements and rotations, the vector of separation of points $\overline{T}^i$ and $\overline{T}^{i+1}$, $\mathbf{r}_\alpha(x, z^i, z^{i+1}) = \mathbf{R}^{i+1}(x, z^{i+1}) - \mathbf{R}^i(x, z^i)$ ($\alpha = 1, 2, \ldots, N-1$ and $i = \alpha$), reads

$$\mathbf{r}_\alpha(x, z^i, z^{i+1}) = \left(u^{i+1}(x) - u^i(x) - d^{i+1}\varphi^{i+1}(x) - (h^i - d^i)\varphi^i(x)\right) \mathbf{E}_X +$$
$$+ \left(w^{i+1}(x) - w^i(x)\right) \mathbf{E}_Z. \qquad (2.7)$$

An interlayer slip between the adjacent layers is denoted by Δu_α and can be defined from Eq. (2.7) as

$$\Delta u_\alpha = u^{i+1} - u^i - d^{i+1}\varphi^{i+1} - (h^i - d^i)\varphi^i. \qquad (2.8)$$

Since all the quantities in Eq. (2.8) are functions of material coordinate x, the notation of the argument x is abandoned. The interlayer uplift (vertical separation) is marked by Δw_α and defined from Eq. (2.7) as

$$\Delta w_\alpha = w^{i+1} - w^i. \qquad (2.9)$$

The term interlayer distortion, $\Delta\varphi_\alpha$, is introduced as well to describe the difference between the rotation angles of adjacent layers as

$$\Delta\varphi_\alpha = \varphi^{i+1} - \varphi^i. \qquad (2.10)$$

In general, flexibility of the contact highly depends on the way the contact is enforced. A constitutive law of the connection between the layers generally assumes a non-linear relationship between contact displacements and interlayer tractions [2, 69]. In the present paper, as generally proposed in the structural engineering practice, a linear constitutive law of the incomplete connection between the layers is assumed, see e.g. [1, 32, 57]. For the contact plane α, a linear uncoupled

constitutive law of the connection between the layers can be written as

$$p_{t,\alpha} = K_{t,\alpha}\Delta u_\alpha,$$
$$p_{n,\alpha} = K_{n,\alpha}\Delta w_\alpha, \tag{2.11}$$

where $K_{t,\alpha}$ and $K_{n,\alpha}$ are the slip and uplift moduli at the interlayer surface. On the other hand, the rotational degree of freedom in the contact defined e.g. as

$$m_{Y,\alpha} = K_{\varphi,\alpha}\Delta\varphi_\alpha, \tag{2.12}$$

is in this paper not taken into account. With Eq. (2.10) only the difference of the cross sectional rotations are defined which is due to different transverse shear deformations of the layers. Eqs (2.11) can be used only in case when interlayer displacements are realised, thus $\Delta u_\alpha \neq 0$ and/or $\Delta w_\alpha \neq 0$. For example, in the case when $\Delta u_\alpha = 0$ from Eqs (2.11) it follows that $p_{t,\alpha} = 0$. That is obviously incorrect, since interlayer tractions also appear when interlayer displacements are absent. This former contradiction originates from the fact that in the limiting case, i.e. $K_{t,\alpha} \to \infty$ and $K_{n,\alpha} \to \infty$, the system of governing equations of a multi-layer composite beam becomes singular [27]. In these cases, the governing equations should be reformulated in a way that will be described below. Note that when $\Delta u_\alpha = 0$, the tangential contact tractions $p_{t,\alpha}$ are calculated from the equilibrium equations, i.e. Eqs (2.2). Similarly, when $\Delta w_\alpha = 0$, the same equilibrium equations are used to express $p_{n,\alpha}$, as well.

2.4 Basic models

The interlayer degrees of freedom can be described using Δu_α, Δw_α, and $\Delta\varphi_\alpha$. By allowing or constraining a specific degree of freedom in the contact plane, $2^3(N-1)$ different combinations of contact plane conditions are introduced. In the present paper only four basic and most common models of different connections between the layers are elaborated although models where the constraining equations are different for each contact plane can be formulated in a similar manner. These common models and their corresponding interlayer degrees of freedom are presented in Tab. 2.1.

TABLE 2.1: Basic models with corresponding interlayer degrees of freedom

MODEL	Δu	Δw	$\Delta \varphi$
$\mathbf{M_{000}}$	$\times$	$\times$	$\times$
$\mathbf{M_{001}}$	$\times$	$\times$	$\checkmark$
$\mathbf{M_{101}}$	$\checkmark$	$\times$	$\checkmark$
$\mathbf{M_{111}}$	$\checkmark$	$\checkmark$	$\checkmark$

$\times$: zero value; $\checkmark$: non-zero value;

The model $\mathbf{M_{000}}$ obviously reintroduces the Bernoulli hypothesis over the entire cross-section ($K_{t,\alpha} \to \infty$, $K_{n,\alpha} \to \infty$ and $K_{\varphi,\alpha} \to \infty$), while the $\mathbf{M_{001}}$ relaxes this hypothesis to make it hold for each layer separately, thus $K_{t,\alpha} \to \infty$ and $K_{n,\alpha} \to \infty$, but $K_{\varphi,\alpha} \in [0,\infty)$. In the models $\mathbf{M_{101}}$ (only $K_{n,\alpha} \to \infty$) and $\mathbf{M_{111}}$ the deformed cross-sections are not requested to remain continuous.

2.4.1   Model "000"

The contact plane conditions for the model $\mathbf{M_{000}}$ according to Tab. 2.1 are described by the following expressions ($i = 1, 2, \ldots, N-1$):

$$
\begin{aligned}
u^{i+1} &= u^i + (h^i - d^i + d^{i+1})\varphi^i, \\
w^i &= w^{i+1} = w^k, \\
\varphi^i &= \varphi^{i+1} = \varphi^k, \\
\varepsilon^{i+1} &= \varepsilon^i + (h^i - d^i + d^{i+1})\kappa^i, \\
\gamma^i &= \gamma^{i+1} = \gamma^k, \\
\kappa^i &= \kappa^{i+1} = \kappa^k,
\end{aligned}
\tag{2.13}
$$

where the index k marks an arbitrary layer from $i = 1, \ldots, N$. After considering relations (2.13) in the general governing equations of the multi-layer beam (2.1)-(2.5), the basic equations of the model $\mathbf{M_{000}}$ are the following:

$$u^{k\prime} - \varepsilon^k = 0, \qquad \mathcal{N}' + \sum_{i=1}^{N} p_X^i = 0,$$

$$w^{k\prime} + \varphi^k - \gamma^k = 0, \qquad \mathcal{Q}' + \sum_{i=1}^{N} p_Z^i = 0,$$

$$\varphi^{k\prime} - \kappa^k = 0, \qquad \mathcal{M}' - \mathcal{Q} + \sum_{i=1}^{N} m_Y^i + \sum_{i=1}^{N} \left(p_{t,i-1} d^i + p_{t,i}(h^i - d^i) \right) = 0 \text{ or} \tag{2.14}$$

$$\mathcal{M}'_{\text{TOT}} - \mathcal{Q} + \sum_{i=1}^{N} m_Y^i = 0,$$

$$\mathcal{N} = \sum_{i=1}^{N} C_1^i \varepsilon^i, \qquad \mathcal{Q} = \sum_{i=1}^{N} C_2^i \gamma^i, \qquad \mathcal{M} = \sum_{i=1}^{N} C_3^i \kappa^i,$$

where

$$\mathcal{N} = \sum_{i} \mathcal{N}^i, \qquad \mathcal{Q} = \sum_{i} \mathcal{Q}^i, \qquad \mathcal{M} = \sum_{i} \mathcal{M}^i.$$

Since every layer has its own separate reference axis, $\mathcal{M}$ is not the total cross-sectional bending moment of a composite beam because the axial forces $\mathcal{N}^i$, that are mutually dislocated, contribute to the total bending moment as well. Thus, $\mathcal{M}_{\text{TOT}} = \mathcal{M} + \sum_{i}^{N} \mathcal{N}^i \ r^i$, where r^i is the distance between the reference axis of the ith layer and the arbitrary axis with respect to whom the total bending moment is computed. The system (2.14) is a system of nine equations for nine unknown functions u^k, w^k, φ^k, $\mathcal{N}$, $\mathcal{Q}$, $\mathcal{M}$ or $\mathcal{M}_{\text{TOT}}$, ε^k, γ^k, and κ^k where the additional functions $p_{t,i}$ are expressed in terms of strains ε^k and γ^k using (2.2), (2.4) and (2.5). Using the last three equations of system (2.13), we express ε^k, γ^k and κ^k in the system (2.14) in terms of u^k, w^k and φ^k, finally obtaining a system of six ordinary linear differential equations with constant coefficients for six unknown functions u^k, w^k, φ^k, $\mathcal{N}$, $\mathcal{Q}$, and $\mathcal{M}$ or $\mathcal{M}_{\text{TOT}}$. This reduced system can be solved analytically with the following boundary conditions from which six constants of

integration are found:

$$f_1^0 \, \mathcal{N}(0) + (1 - f_1^0) \, u^k(0) = f_1^0 \, S_1^0 + (1 - f_1^0) \, U_1^k(0),$$

$$f_2^0 \, \mathcal{Q}(0) + (1 - f_2^0) \, w^k(0) = f_2^0 \, S_2^0 + (1 - f_2^0) \, U_2^k(0),$$

$$f_3^0 \, \mathcal{M}(0) + (1 - f_3^0) \, \varphi^k(0) = f_3^0 \, S_3^0 + (1 - f_3^0) \, U_3^k(0),$$

$$f_1^L \, \mathcal{N}(L) + (1 - f_1^L) \, u^k(L) = f_1^L \, S_1^L + (1 - f_1^L) \, U_1^k(L), \qquad (2.15)$$

$$f_2^L \, \mathcal{Q}(L) + (1 - f_2^L) \, w^k(L) = f_2^L \, S_2^L + (1 - f_2^L) \, U_2^k(L),$$

$$f_3^L \, \mathcal{M}(L) + (1 - f_3^L) \, \varphi^k(L) = f_3^L \, S_3^L + (1 - f_3^L) \, U_3^k(L),$$

where $S_n^0 = \sum_{i=1}^{N} S_n^{0,i}$ and $S_n^L = \sum_{i=1}^{N} S_n^{L,i}$ $(n = 1, 2, 3)$, are the external end point forces and moments of the beam, while U_n^0 and U_n^L are the displacements and the rotations at the beam ends that are identical for all layers. The coefficients f_n^0 and f_n^L have values 1 or 0 depending on the type of the support at the beam ends.

2.4.2 Model "001"

This model is defined by the contact plane conditions described below:

$$u^{i+1} = u^i + d^{i+1}\varphi^{i+1} + (h^i - d^i)\varphi^i,$$

$$w^i = w^{i+1} = w^k,$$

$$\varepsilon^{i+1} = \varepsilon^i + d^{i+1}\kappa^{i+1} + (h^i - d^i)\kappa^i, \qquad (2.16)$$

$$\gamma^{i+1} = \gamma^i + \varphi^{i+1} - \varphi^i,$$

where $i = 1, 2, \ldots, N - 1$. The basic equations of the model are written by considering relations (2.16) as $(i = 1, ..., N)$

$$u^{k\prime} - \varepsilon^k = 0, \qquad \mathcal{N}' + \sum_{i=1}^{N} p_X^i = 0,$$

$$w^{k\prime} + \varphi^k - \gamma^k = 0, \qquad \mathcal{Q}' + \sum_{i=1}^{N} p_Z^i = 0, \qquad (2.17)$$

$$\varphi^{i\prime} - \kappa^i = 0, \qquad \mathcal{M}^{i\prime} - \mathcal{Q}^i + m_Y^i + p_{t,i-1}d^i + p_{t,i}(h^i - d^i) = 0,$$

$$\mathcal{N} = \sum_{i=1}^{N} C_1^i \varepsilon^i, \qquad \mathcal{Q} = \sum_{i=1}^{N} C_2^i \gamma^i, \qquad \mathcal{M}^i = C_3^i \kappa^i.$$

Similarly as in the model $\mathbf{M_{000}}$, the contact tractions $p_{t,\alpha}$ ($\alpha = 1, 2, \ldots, N - 1$) are expressed via the strains ε^k, γ^k, and κ^i which are further expressed via displacements u^k, w^k, and φ^i, ($i = 1, 2, \ldots, N$). This allows reducing the system (2.17) to a system of $4 + 2N$ linear first-order ordinary differential equations with constants coefficients for the same number of unknown functions: u^k, w^k, $\mathcal{N}$, $\mathcal{Q}$, φ^i, and $\mathcal{M}^i$ ($i = 1, 2, \ldots, N$). These functions are determined after the system is solved in conjunction with the following boundary conditions:

$$
\begin{aligned}
f_1^0 \, \mathcal{N}(0) + (1 - f_1^0) \, u^k(0) &= f_1^0 \, S_1^0 + (1 - f_1^0) \, U_1^0, \\
f_2^0 \, \mathcal{Q}(0) + (1 - f_2^0) \, w^k(0) &= f_2^0 \, S_2^0 + (1 - f_2^0) \, U_2^0, \\
f_3^{0,i} \, \mathcal{M}^i(0) + (1 - f_3^{0,i}) \, \varphi^i(0) &= f_1^{0,i} \, S_3^{0,i} + (1 - f_3^{0,i}) \, U_3^{0,i}, \\
f_1^L \, \mathcal{N}(L) + (1 - f_1^L) \, u^k(L) &= f_1^L \, S_1^L + (1 - f_1^L) \, U_1^L, \\
f_2^L \, \mathcal{Q}(L) + (1 - f_2^L) \, w^k(L) &= f_2^L \, S_2^L + (1 - f_2^L) \, U_2^L, \\
f_3^{L,i} \, \mathcal{M}^i(L) + (1 - f_3^{L,i}) \, \varphi^i(L) &= f_3^{L,i} \, S_3^{L,i} + (1 - f_3^{L,i}) \, U_3^{L,i},
\end{aligned}
\tag{2.18}
$$

where $S_n^0 = \sum_{i=1}^N S_n^{0,i}$ and $S_n^L = \sum_{i=1}^N S_n^{L,i}$ ($n = 1, 2$) and $f_3^{0,i}$ and $f_3^{L,i}$ are the boundary conditions coefficients at the beam ends for each layer. They have values 1 or 0 depending on the type of the support at the both ends of each layer. External moments and rotations at the ends of each layer are denoted by $S_3^{0,i}$, $S_3^{L,i}$ and $U_3^{0,i}$, $U_3^{L,i}$, respectively. In addition, note that $U_1^0, U_2^0, U_1^L,$ and U_2^L are the same for all layers.

2.4.3 Model "101"

Using the contact conditions from Tab. 2.1, the following relations are derived ($\alpha = 1, 2, \ldots, N - 1$ and $i = \alpha$)

$$
\begin{aligned}
w^i &= w^{i+1} = w^k \\
\gamma^{i+1} &= \gamma^i + \varphi^{i+1} - \varphi^i, \\
p_{t,\alpha} &= K_{t,\alpha} \Delta u_\alpha.
\end{aligned}
\tag{2.19}
$$

The basic equations for the model $\mathbf{M_{101}}$ are presented below $(i = 1, 2, \ldots, N)$:

$$u^{i\prime} - \varepsilon^i = 0, \qquad\qquad \mathcal{N}^{i\prime} + p_X^i - p_{t,i-1} + p_{t,i} = 0,$$

$$w^{k\prime} + \varphi^k - \gamma^k = 0, \qquad \mathcal{Q}' + \sum_{i=1}^N p_Z^i = 0, \tag{2.20}$$

$$\varphi^{i\prime} - \kappa^i = 0, \qquad\qquad \mathcal{M}^{i\prime} - \mathcal{Q}^i + m_Y^i + p_{t,i}d^i + p_{t,i-1}(h^i - d^i) = 0,$$

$$\mathcal{N}^i = C_1^i \varepsilon^i, \qquad \mathcal{Q} = \sum_{i=1}^N C_2^i \gamma^i, \qquad \mathcal{M}^i = C_3^i \kappa^i.$$

The strains ε^i, γ^k and κ^i are expressed via internal forces $\mathcal{N}^i$, $\mathcal{Q}$ and $\mathcal{M}^i$ from the constitutive equations (last $2N + 1$ equations of the system (2.20)). The contact tractions $p_{t,\alpha}$ are expressed via displacements u^i and rotations φ^i from Eqs (2.19) and (2.8). The system (2.20) is reduced to a system of $2 + 4N$ linear first-order ordinary differential equations with constant coefficients for the same number of unknown functions: u^i, w^k, φ^i, $\mathcal{N}^i$, $\mathcal{Q}$, and $\mathcal{M}^i$ $(i = 1, 2, \ldots, N)$. To solve this system the corresponding boundary conditions are considered:

$$f_1^{0,i} \mathcal{N}^i(0) + (1 - f_1^{0,i}) u^i(0) = f_1^{0,i} S_1^{0,i} + (1 - f_1^{0,i}) U_1^{0,i},$$

$$f_2^0 \mathcal{Q}(0) + (1 - f_2^0) w^k(0) = f_2^0 S_2^0 + (1 - f_2^0) U_2^0,$$

$$f_3^{0,i} \mathcal{M}^i(0) + (1 - f_3^{0,i}) \varphi^i(0) = f_3^{0,i} S_3^{0,i} + (1 - f_3^{0,i}) U_3^{0,i},$$

$$f_1^{L,i} \mathcal{N}^i(L) + (1 - f_1^{L,i}) u^i(L) = f_1^{L,i} S_1^{L,i} + (1 - f_1^{L,i}) U_1^{L,i}, \tag{2.21}$$

$$f_3^L \mathcal{Q}(L) + (1 - f_2^L) w^k(L) = f_2^L S_2^L + (1 - f_2^L) U_2^L,$$

$$f_5^{L,i} \mathcal{M}^i(L) + (1 - f_3^{L,i}) \varphi^i(L) = f_3^{L,i} S_3^{L,i} + (1 - f_3^{L,i}) U_3^{L,i},$$

where $S_2^0 = \sum_{i=1}^N S_2^{0,i}$ and $S_2^L = \sum_{i=1}^N S_2^{L,i}$ and $f_1^{0,i}$ and $f_1^{L,i}$ are the boundary conditions coefficients with values 0 or 1 depending on the type of support the ends of each layer. The external longitudinal point forces and horizontal displacements at the ends of each layer are denoted as $S_1^{0,i}$, $S_1^{L,i}$ and $U_1^{0,i}$, $U_1^{L,i}$, respectively. Again, note that U_2^0 and U_2^L are the same for all layers.

2.4.4 Model "111"

The contact plane conditions for this model are expressed using only the constraining equations (2.11). The basic equations of this model are presented below

$(i = 1, 2, \ldots, N)$:

$$u^{i\prime} - \varepsilon^i = 0, \qquad \mathcal{N}^{i\prime} + p_X^i - p_{t,i-1} + p_{t,i} = 0,$$
$$w^{i\prime} + \varphi^i - \gamma^i = 0, \qquad \mathcal{Q}^{i\prime} + p_Z^i - p_{n,i-1} + p_{n,i} = 0, \qquad (2.22)$$
$$\varphi^{i\prime} - \kappa^i = 0, \qquad \mathcal{M}^{i\prime} - \mathcal{Q}^i + m_Y^i + p_{t,i-1}d^i + p_{t,i}(h^i - d^i) = 0,$$

$$\mathcal{N}^i = C_1^i \varepsilon^i, \qquad \mathcal{Q}^i = C_2^i \gamma^i, \qquad \mathcal{M}^i = C_3^i \kappa^i.$$

The strains ε^i, γ^i, and κ^i are expressed via internal forces $\mathcal{N}^i$, $\mathcal{Q}^i$, and $\mathcal{M}^i$ from the constitutive equations (last $3N$ equations in the system (2.22)) and the contact tractions $p_{t,\alpha}$ and $p_{n,\alpha}$ from Eqs (2.11). System (2.22) is reduced to a system of $6N$ linear first-order ordinary differential equations with constant coefficients for the same number of unknown functions: u^i, w^i, φ^i, $\mathcal{N}^i$, $\mathcal{Q}^i$, and $\mathcal{M}^i$ $(i = 1, 2, \ldots, N)$. The corresponding boundary conditions are:

$$f_1^{0,i} \mathcal{N}^i(0) + (1 - f_1^{0,i}) u^i(0) = f_1^{0,i} S_1^{0,i} + (1 - f_1^{0,i}) U_1^{0,i},$$
$$f_2^{0,i} \mathcal{Q}^i(0) + (1 - f_2^{0,i}) w^i(0) = f_2^{0,i} S_2^{0,i} + (1 - f_2^{0,i}) U_2^{0,i},$$
$$f_3^{0,i} \mathcal{M}^i(0) + (1 - f_3^{0,i}) \varphi^i(0) = f_3^{0,i} S_3^{0,i} + (1 - f_3^{0,i}) U_3^{0,i},$$
$$f_1^{L,i} \mathcal{N}^i(L) + (1 - f_1^{L,i}) u^i(L) = f_1^{L,i} S_1^{L,i} + (1 - f_1^{L,i}) U_1^{L,i}, \qquad (2.23)$$
$$f_2^{L,i} \mathcal{Q}^i(L) + (1 - f_2^{L,i}) w^i(L) = f_2^{L,i} S_2^{L,i} + (1 - f_2^{L,i}) U_2^{L,i},$$
$$f_3^{L,i} \mathcal{M}^i(L) + (1 - f_3^{L,i}) \varphi^i(L) = f_3^{L,i} S_3^{L,i} + (1 - f_3^{L,i}) U_3^{L,i},$$

where $f_n^{0,i}$ and $f_n^{L,i}$ $(n = 1, 2, 3)$ are the boundary conditions coefficients for each layer, while $S_n^{0,i}$, $S_n^{L,i}$ and $U_n^{0,i}$, $U_n^{L,i}$ are the external transverse point forces and vertical displacements at the ends of each layer, respectively.

2.5 Analytical solution

The reduced system of generalised equilibrium equations (2.14), (2.17), (2.20), and (2.22) are the systems of linear first-order ordinary differential equations with constant coefficients. Similarly, the systems of generalised equations of other mathematical models not introduced in the paper are also systems of linear first-order ordinary differential equations with constant coefficients. In general, such systems

of equations can be written in the following compact form as

$$\boldsymbol{Y}'(x) = \boldsymbol{B}\boldsymbol{Y}(x) + \boldsymbol{g}, \quad \boldsymbol{Y}(0) = \boldsymbol{Y}_0, \tag{2.24}$$

where $\boldsymbol{Y}$ is the vector of unknown functions, $\boldsymbol{g}$ is the vector of external loading, $\boldsymbol{B}$ is the matrix of constant coefficients, and $\boldsymbol{Y}_0$ is the vector of boundary parameters that are determined from the boundary conditions of the multi-layer beam. The solution of the inhomogeneous system of differential equations (2.24) is composed of homogeneous and particular solutions [44].

$$\boldsymbol{Y}(x) = \exp(\boldsymbol{B}x)[\boldsymbol{Y}_0 + \int_0^x \exp(-\boldsymbol{B}\xi)\boldsymbol{g}\,\mathrm{d}\xi] \tag{2.25}$$

When a multi-layer beam is subjected only to point forces and moments, i.e $\boldsymbol{g} = \boldsymbol{0}$, the solution of (2.24) is composed of a homogeneous solution only

$$\boldsymbol{Y}(x) = \exp(\boldsymbol{B}x)\boldsymbol{Y}_0 \tag{2.26}$$

Similarly as in the case of homogeneous structures, the multi-layer structures are composed of multi-layer beams. In such cases, the analytical solution is obtained from the analytical solution of individual multi-layer beam. The procedure is very similar to the finite element method.

2.6   Numerical results and discussion

Two numerical examples are analysed in detail in order to illustrate the present theory. In the first example the influence of various parameters on the midspan vertical displacement of a sandwich beam has been investigated. The influence of contact discontinuity between the layers of a composite beam on its bearing capacity has been illustrated in the second example.

2.6.1 Simply supported sandwich beam with uniformly distributed load

A parametric study for this example has been performed on a simply supported sandwich beam subjected to a uniformly distributed load (see Fig. 2.3). The sandwich beam layers are denoted by $i = a, b, c$ and the contact planes by $\alpha = 1, 2$, respectively. The geometrical and material characteristics are the following: $L^i = L = 100\,\mathrm{mm}, h^a = h^c = 1\,\mathrm{mm}, h^b = 18\,\mathrm{mm}, b^i = 60\,\mathrm{mm}, E^a = E^c = 2 \cdot 10^4\,\mathrm{N/mm^2}, E^b = E^a/50, G^a = E^a/8, G^b = 3/4\,E^b, G^c = E^c/8, k_y^i = 5/6$. The uniformly distributed load, $p_Z^a = 2$ N/mm, is applied on the layer a.
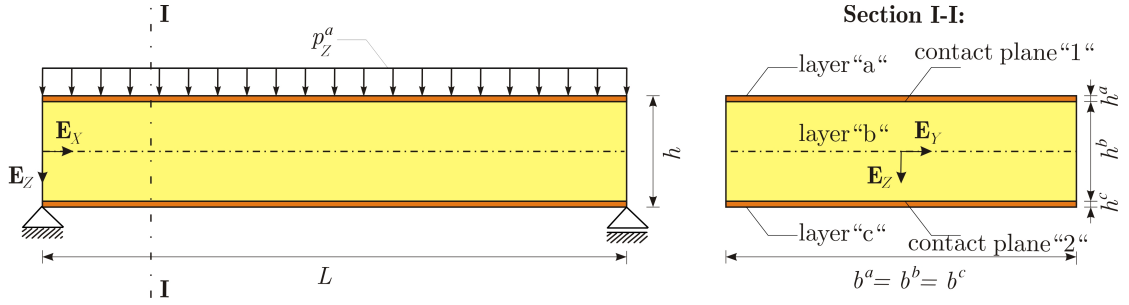
FIGURE 2.3: Simply supported sandwich beam with uniformly distributed vertical load.

Note that the values of the shear moduli fall outside the range of possible values for an isotropic material, but are perfectly acceptable e.g. for timber [57]. Due to symmetry, only one half of the sandwich beam has been analysed, so that the boundary conditions are given as:

$$\mathcal{N}^i(0) = \mathcal{N}^b(0) = 0, \quad w^i(0) = 0 \quad \mathcal{M}^i(0) = 0, \tag{2.27}$$

on the left-hand side of the beam, and

$$u^i(L/2) = 0, \quad \mathcal{Q}^i(L/2) = 0, \quad \varphi^i(L/2) = 0, \tag{2.28}$$

on the middle of the beam, where $(i = a, b, c)$. Defining the boundary conditions in this manner allows us to solve the problem where $K_{t,\alpha} = 0, (\alpha = 1, 2)$. In Tab. 2.2 the vertical displacements of the centroid axis at the midspan of the sandwich beam for different multi-layer beam models are presented depending on the L/h ratio. For $L/h = 5$ the same characteristics as given above have been used, while for other

L/h ratios only the length of the beam has been modified accordingly. A vertical displacement of a homogeneous beam according to the classical engineering theory proposed by Timoshenko [66], $w_\infty = \dfrac{5p_Z^a L^4}{384EI_\infty} + \dfrac{p_Z^a L^2}{8k_y GA_\infty}$, has been used as a reference vertical displacement, where $EI_\infty = EI_0 + E^a A^a \dfrac{(h^a + h^b)^2}{4} + E^c A^c \dfrac{(h^b + h^c)^2}{4}$, $EI_0 = \sum\limits_{i=a}^{c} E^i I^i$ and $k_y GA_\infty = \sum\limits_{i=a}^{c} k_y^i G^i A^i$. The non-dimensional vertical displacement, $\overline{w}_M = \dfrac{w_M}{w_\infty}$, is introduced, where w_M is the vertical displacements at the midspan of a sandwich beam for an arbitrary model M. Four values of the slip modulus $K_{t,\alpha}$ for $\alpha = 1, 2$ are analysed: $0, 1, 10$ and $100\,\mathrm{N/mm^2}$. The model **M_{000}** shows exactly the same behaviour as the homogeneous beam, which is due to its rigid interlayer connection ($\Delta u_\alpha = \Delta w_\alpha = \Delta\varphi_\alpha = 0$ where $\alpha = 1, 2$). The differences between the results of the models **M_{000}** and **M_{001}** range between approximately 7% for a moderately thick beam ($L/h = 10$) to more than about 53% for a very thick beam ($L/h = 2$). By allowing the interlayer slip to occur, the vertical displacements at the midspan increase more considerably, especially as interaction between the layers gets weaker ($K_{t,\alpha} \to 0$). In the last column in Tab. 2.2 the non-dimensional vertical displacement for a sandwich beam with no interaction between the layers is given according to the Bernoulli beam theory as $\overline{w}_0 = \dfrac{w_0}{w_\infty}$ with $w_0 = \dfrac{5\,p_Z^a\,L^4}{384EI_0}$, where index 0 refers to completely separate layers. As expected, the results of the model **M_{101}** with $K_{t,\alpha} = 0$ approach this solution as the beam becomes thinner.

TABLE 2.2: Non-dimensional vertical displacement ($\overline{w}_M = w_M/w_\infty$) at the midspan for various contact plane conditions depending on L/h ratio.

L/h	w_∞ [mm]	M_{000}	M_{001}	M_{101} $K_{t,\alpha^\star} = 100^*$	$K_{t,\alpha^\star} = 10^*$	$K_{t,\alpha^\star} = 1^*$	$K_{t,\alpha^\star} = 0^*$	$\overline{w}_0$
2	0.00106	1.00000	1.53262	5.58215	6.51117	6.62796	6.64128	5.29600
5	0.01621	1.00000	1.21944	6.09954	12.28912	13.88957	14.09633	13.54423
7	0.05321	1.00000	1.13108	4.69571	12.52822	15.71016	16.17645	15.84678
10	0.20161	1.00000	1.07063	3.24534	11.06386	16.58495	17.59765	17.42006

$\star\ \alpha = a, b;\ *$ in $\mathrm{N/mm^2}$

The core thickness ratio influence is described by h^b/h, where h^b is the core's height while h is the total height of the sandwich beam cross-section. By changing the core height but keeping the total height constant ($h = 20$ mm) the vertical displacement at the midspan is studied (see Fig. 2.4). The values of $K_{t,\alpha}$ are written in the parentheses next to **M_{101}** in the legend to Fig. 2.4. It is noticed that w increases monotonically with h^b/h ratio for the models **M_{000}** and **M_{001}**, but

for the model $\mathbf{M_{101}}$ an extreme value of w appears for the presented values of $K_{t,\alpha}$. For $K_{t,\alpha} = 0$, the maximum vertical displacement at the midspan is obtained for $h^c/h \approx 0.8$, while for the higher stiffnesses $K_{t,\alpha}$ the maximum vertical displacement occurs at lower h_b/h ratios. From the expression for w_0, it can be easily shown that the beam stiffness EI_0 has a maximum at $h^b/h = 0.7795$ which coincides very well with the present result for the model $\mathbf{M_{101}}$ with $K_{t,\alpha} = 0$.
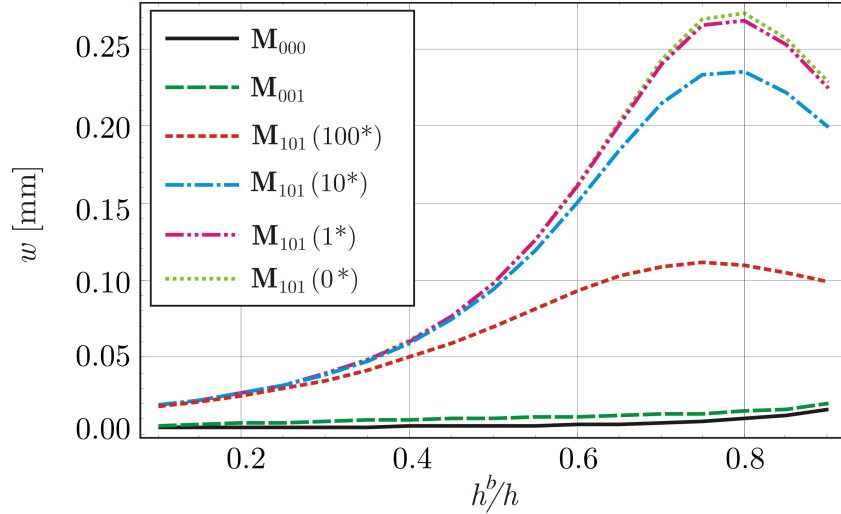
FIGURE 2.4: w vs. h_b/h for different contact plane conditions (* represents $K_{t,\alpha}$ in N/mm^2).

The influence of the core elastic-to-shear modulus ratio, E^b/G^b, on midspan vertical displacements is displayed in Fig.2.5. The range $0 < E^b/G^b < 100$ is reasonable only for anisotropic materials. A considerable difference of the results between the models $\mathbf{M_{000}}$ and $\mathbf{M_{001}}$ is observed by the interlayer distortion which is dependent on the layer's shear modulus. In case when $\Delta w_\alpha = 0$ it follows that $\Delta\varphi_\alpha = \gamma^{i+1} - \gamma^i = \mathcal{Q}^{i+1}/C_2^{i+1} - \mathcal{Q}^i/C_2^i$ (see Eqs 2.5), which means that the higher values of the shear moduli produce smaller values of the interlayer distortion and thus smaller vertical displacements. Obviously, as the E^b/G^b ratio increases the differences between the models $\mathbf{M_{000}}$ and $\mathbf{M_{001}}$ become more pronounced. For models $\mathbf{M_{101}}$ the interlayer slip (depending on different $K_{t,\alpha}$ values) causes a considerable increase in the vertical displacements in comparison to model $\mathbf{M_{001}}$. It is noticed that all models have almost linear $E_b/G_b - w$ relationship.
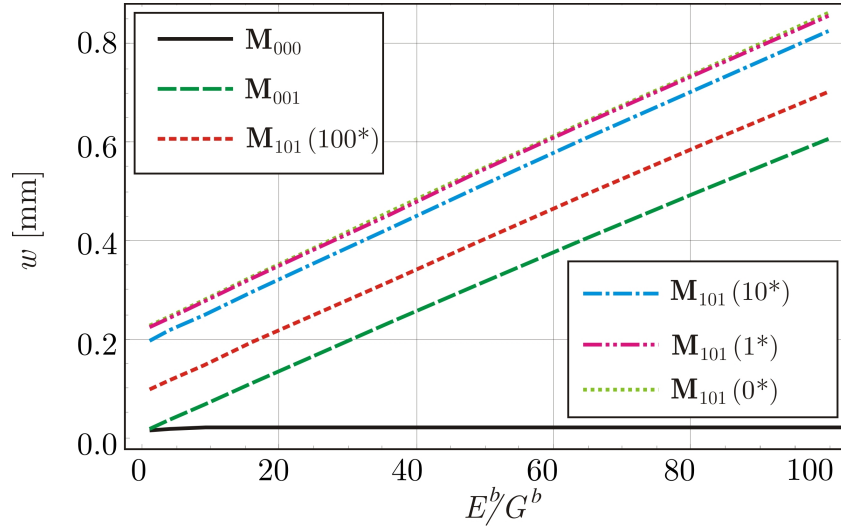
FIGURE 2.5: w vs. E^b/G^b for different contact plane conditions (* represents $K_{t,\alpha}$ in N/mm^2).

2.6.2 Contact discontinuity influence studies

A simply supported two-layer beam is analysed in this example (see Fig. 2.6). Layers are marked by $i = a, b$. The geometrical and material characteristics are as follows: $L^i = L = 200$ cm, $h^i = 10$ cm, $b^i = 20$ cm, $E^i = 800$ kN/cm^2, $G^i = E^i/16$, $k^i_y = 5/6$. The uniformly distributed load, $p^b_Z = 0.2$ kN/cm, is applied at the reference layer of the lower layer b.
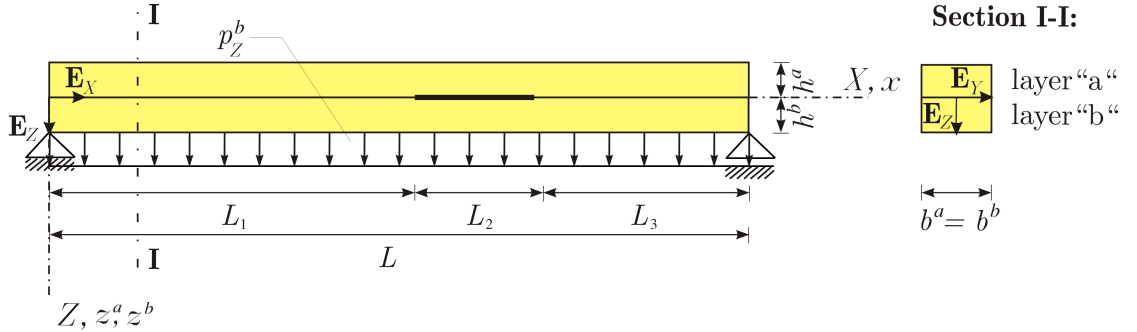
FIGURE 2.6: Simply supported two-layer beam.

The beam is divided into three segments, namely e_1, e_2 and e_3, whose lengths are L_1, L_2, and L_3, respectively. The central segment is made of two completely separate layers, hence model $\mathbf{M_{111}}$ with $K_t = K_n = 0$ is used. The relative mid-segment length is defined by $\beta = L_2/L$. The outer segments' layers are connected according to the model $\mathbf{M_{101}}$. The connection between the segments is defined by the following continuity conditions: $\eta^i_{e_1}(L_1) = \eta^i_{e_2}(0)$ and $\eta^i_{e_2}(L_2) = \eta^i_{e_3}(0)$, where $\eta^i_j = u^i_j$, w^i_j, φ^i_j, $\mathcal{N}^i_j$, $\mathcal{M}^i_j$, where $i = a, b$, and $j = e_1, e_2, e_3$.

The conditions for transverse equilibrium at the connection of the segments are $\mathcal{Q}_{e_1}(L_1) = \mathcal{Q}_{e_2}^a(0) + \mathcal{Q}_{e_2}^b(0)$ and $\mathcal{Q}_{e_2}^a(L_2) + \mathcal{Q}_{e_2}^b(L_2) = \mathcal{Q}_{e_3}(0)$. The influence of the interlayer slip modulus K_t between the layers with the segment lengths L_1 and L_3, and separation length L_2, on the beam displacements and equilibrium forces has been examined next. It is noticed that although the slip modulus has an influence on all displacements, the interlayer uplift (Δw) and distortion ($\Delta \varphi$), remain unchanged for a given value of β under a variation of K_t (Fig. 2.7a).
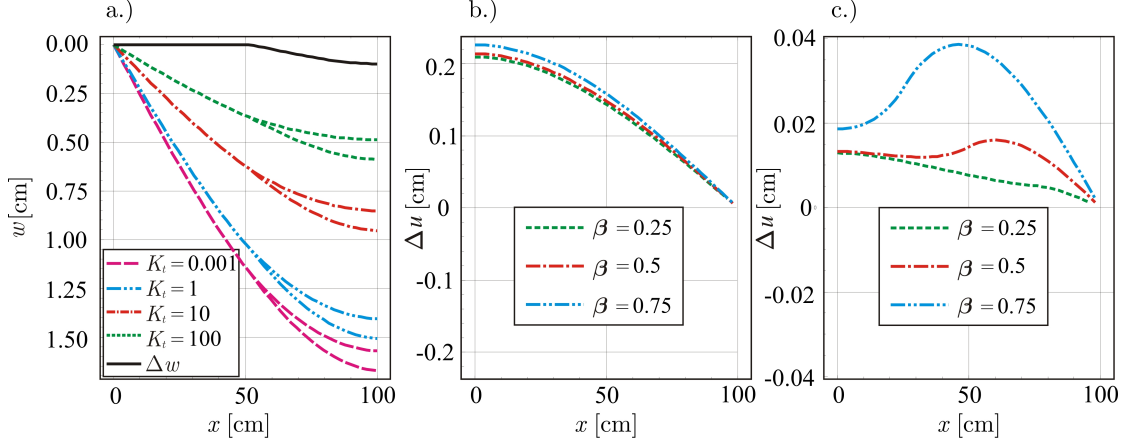
FIGURE 2.7: a.) Vertical displacements for $\beta = 0.5$ and various K_ts; b.) Interlayer slip for $K_t = 1$ kN/cm² and various βs; c.) Interlayer slip for $K_t = 100$ kN/cm² and various βs.

The interlayer uplift occurs only at the central segment where other than the applied loading, w^i depends on φ^i at the contact with the outer segments, since the segments on a single layer are rigidly connected. By expanding the expression for the interlayer distortion as $\Delta \varphi = \varphi^b - \varphi^a = \gamma^b - w^{b\prime} - (\gamma^a - w^{a\prime}) = \mathcal{Q}^b/C_2^b - \mathcal{Q}^a/C_2^a - \Delta w'$, no dependence between $\Delta \varphi$ and K_t is noticed, since shear forces are independent of K_t (see Eqs (2.22)). This means that Δw is independent of K_t and so is $\Delta \varphi$ (on the entire length of the beam). Vertical displacement along the span has been plotted for $\beta = 0.5$ and different values of K_t in Fig. 2.7a. The interlayer slip, Δu, for $\beta = 0.25, 0.5, 0.75$, and $K_t = 1, 100$ kN/cm² has been shown in Figs. 2.7b and c. As expected, Δu, increases with decreasing of K_t and increasing the separation length.

The slip modulus K_t affects the distribution of the axial equilibrium forces and the tangential contact tractions p_t, which can be observed again for $\beta = 0.25, 0.5, 0.75$, and $K_t = 1, 100$ kN/cm² in Figs. 2.8–2.9.
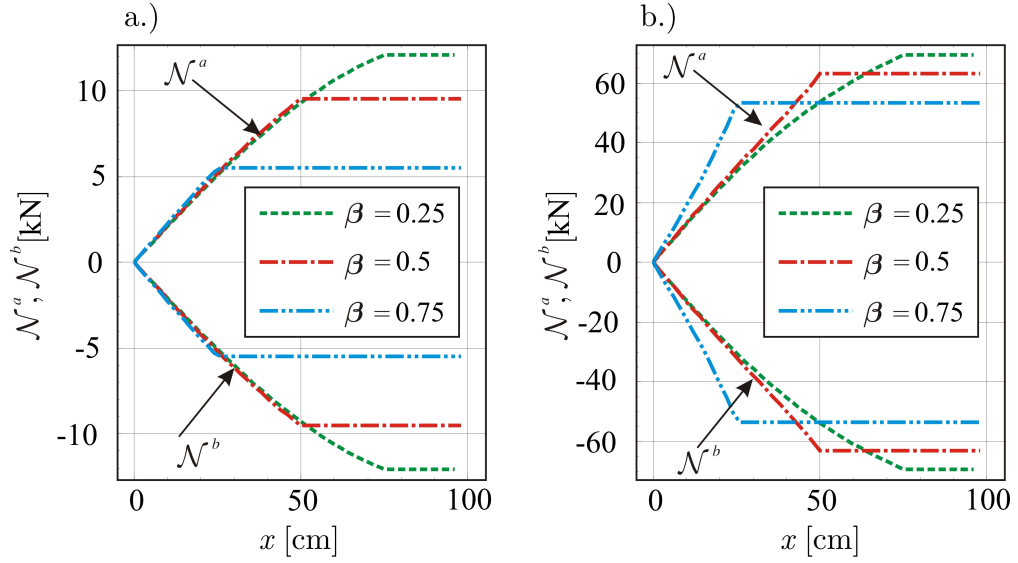
FIGURE 2.8: Axial equilibrium forces: a.) $K_t = 1$ kN/cm^2.; b.) $K_t = 100$ kN/cm^2.
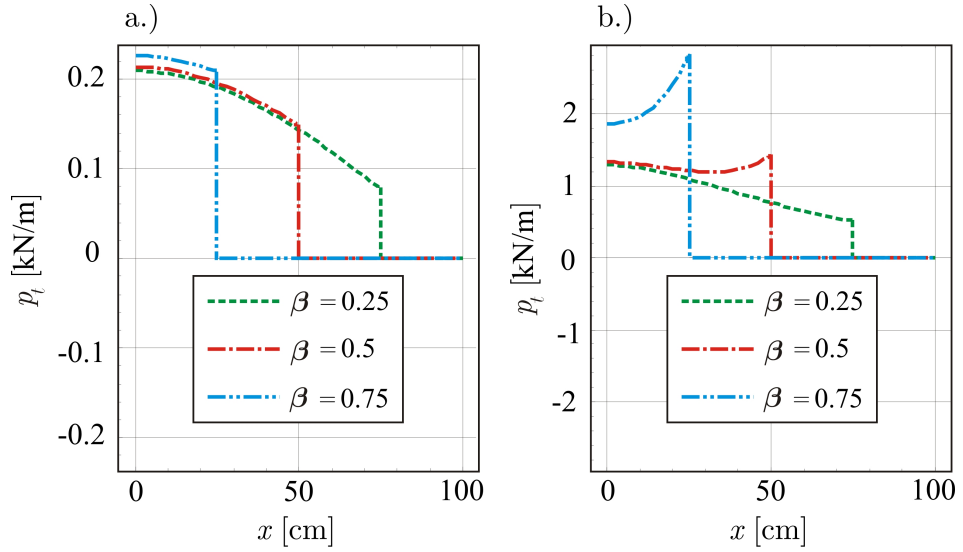
FIGURE 2.9: Tangential contact tractions: a.) $K_t = 1$ kN/cm^2; b.) $K_t = 100$ kN/cm^2.

In case of $K_t = 1$ kN/cm^2, the layers behave almost independently (not much difference between the inner and the outer segments) and the variation of β has little effect. In the latter case the slip modulus is high and the influence of β is more pronounced. The shear forces are, as stated earlier, independent of K_t, and so are the normal interlayer tractions (see Eqs (2.11) and (2.9)). Their distributions are for different values of β shown in Fig. 2.10.
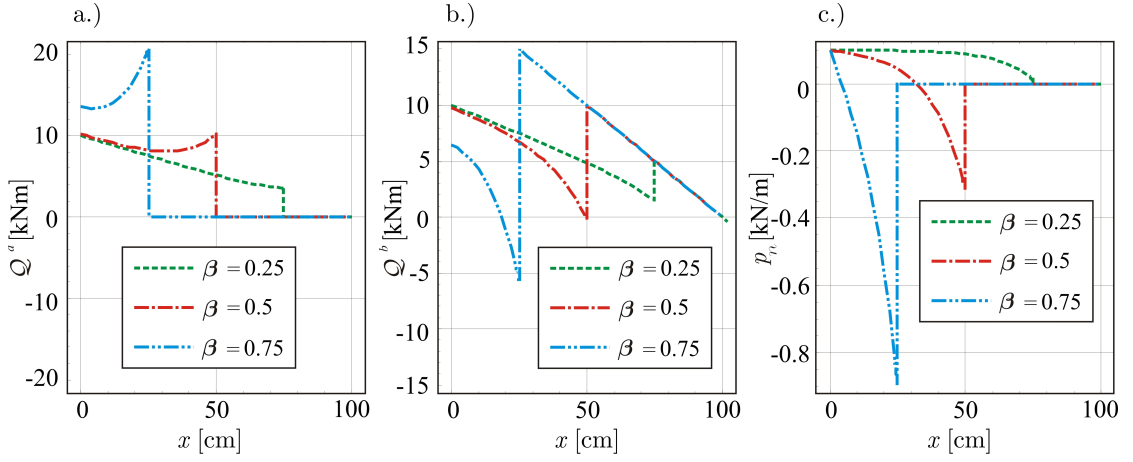
FIGURE 2.10: Shear forces: a.) layer a; b.) layer b; and c.) normal contact tractions. All quantities are K_t independent.

2.6.3 Comments on the boundary layer effect

In the context of composite beams with interlayer slip, the boundary layer effect appears in the case of bending due to boundary moments M_0 and becomes increasingly pronounced with growing shear stiffness of the interlayer connection. When each individual layer of a two-layer beam is subjected to an end moment ($\mathcal{M}^a(0) + \mathcal{M}^b(0) = M_0$ and $\mathcal{M}^a(L) + \mathcal{M}^b(L) = M_0$) with zero axial load ($\mathcal{N}^a(0) = \mathcal{N}^b(0) = 0$ and $\mathcal{N}^a(L) = \mathcal{N}^b(L) = 0$), the normal forces in each layer and the tangential tractions at the interlayer connection emerge between the beam boundaries even though at the boundaries they do not exist.

This problem was investigated by Challamel and Girhammar [11] for a two-layer beam with interlayer slip using the Euler-Bernoulli beam theory. In the present work the same problem is investigated using the Timoshenko beam theory. Substituting $\mathcal{M}^a = C_3^a \varphi^{a\prime}$ and $\mathcal{M}^b = C_3^b \varphi^{b\prime}$ from (2.20) into overall equilibrium along the beam $M_0 = \mathcal{M}^a + \mathcal{M}^b - \mathcal{N}^a \frac{h^a+h^b}{2}$ yields

$$M_0 = C_3^a \varphi^{a\prime} + C_3^b \varphi^{b\prime} - \mathcal{N}_a \frac{h^a + h^b}{2} \tag{2.29}$$

while substituting $u^{a\prime} = \frac{\mathcal{N}^a}{C_1^a}$ and $u^{b\prime} = \frac{\mathcal{N}^b}{C_1^b}$ from (2.20) into the derivative of (2.8) and the result into into the derivative of $(2.19)_3$ and then into the derivative of $\mathcal{N}^{a\prime} + p_{t,a} = 0$ from (2.20) yields

$$\mathcal{N}^{a\prime\prime} = K_t \left[\mathcal{N}^a \left(\frac{1}{C_1^a} + \frac{1}{C_1^b} \right) + \frac{h^a}{2} \varphi^{a\prime} + \frac{h^b}{2} \varphi^{b\prime} \right]. \tag{2.30}$$

28

Likewise, substituting $\gamma^a = \frac{C_3^a \varphi^{a\prime\prime} - \mathcal{N}^{a\prime} \frac{h^a}{2}}{C_2^a}$ and $\gamma^b = \frac{C_3^b \varphi^{b\prime\prime} - \mathcal{N}^{b\prime} \frac{h^b}{2}}{C_2^b}$ from (2.20) into $(2.19)_2$ yields

$$\varphi^1 - \varphi^2 - \frac{C_3^a \varphi^{a\prime\prime} - \mathcal{N}^{a\prime} \frac{h^a}{2}}{C_2^a} + \frac{C_3^b \varphi^{b\prime\prime} - \mathcal{N}^{b\prime} \frac{h^b}{2}}{C_2^b} = 0. \tag{2.31}$$

Solving (2.29) and (2.30) for $\varphi^{a\prime}$ and $\varphi^{b\prime}$ and substituting the result into the derivative of (2.31) we obtain the following fourth-order differential equation

$$c_1 \frac{\mathrm{d}^4 \mathcal{N}^a}{\mathrm{d}x^4} + c_2 \frac{\mathrm{d}^2 \mathcal{N}^a}{\mathrm{d}x^2} + c_3 \mathcal{N}^a + c_4 M_0 = 0, \tag{2.32}$$

where

$$c_1 = \frac{2 C_3^a C_3^b}{K_t (C_3^a h^b - C_3^b h^a)} \left(\frac{1}{C_2^a} + \frac{1}{C_2^b} \right), \tag{2.33}$$

$$c_2 = \frac{2}{C_3^b h^a - C_3^a h^b} \left\{ \frac{C_3^a + C_3^b}{K_t} + \left(\frac{1}{C_2^a} + \frac{1}{C_2^b} \right) \left[C_3^a C_3^b \left(\frac{1}{C_1^a} + \frac{1}{C_1^b} \right) + \right. \right.$$
$$\left. \left. + \frac{C_3^b (h^a)^2 + C_3^a (h^b)^2}{4} \right] \right\}, \tag{2.34}$$

$$c_3 = \frac{2(C_3^a + C_3^b)}{C_3^a h^b - C_3^b h^a} \left[\frac{1}{C_1^a} + \frac{1}{C_1^b} + \frac{(h^a + h^b)^2}{4(C_3^a + C_3^b)} \right], \tag{2.35}$$

$$c_4 = \frac{h^a + h^b}{C_3^a h^b - C_3^b h^a}. \tag{2.36}$$

For the Euler-Bernoulli beam theory, shear moduli $G^i \to \infty$ and $C_2^i = k_y^i G^i A^i \to \infty$, $(i = a, b)$, reducing equation (2.32) to exactly the same form as given by Challamel and Girhammar [11]:

$$\frac{\mathrm{d}^2 \mathcal{N}^a}{\mathrm{d}x^2} - \alpha_T^2 \mathcal{N}_1 = \beta_T M_0, \tag{2.37}$$

where

$$\alpha_T^2 = \frac{c_3}{c_2} = K_t \left[\frac{1}{C_1^a} + \frac{1}{C_1^b} + \frac{(h^a + h^b)^2}{4(C_3^a + C_3^b)} \right], \tag{2.38}$$

$$\beta_T = \frac{c_4}{c_2} = \frac{K_t (h^a + h^b)}{2(C_3^a + C_3^b)}. \tag{2.39}$$

Using the model $\mathbf{M_{101}}$ and considering a simply supported two layer beam with identical geometrical and material properties as in the previous exmple without discontinuity in the interlayer connection ($L_2 = 0$, see Fig.2.11), a numerical

analysis is performed according to Challamel and Girhammar [11].

FIGURE 2.11: Beam model for the boundary-effect analysis

Since for the case of pure bending no transverse forces appear, the results obtained using model $\mathbf{M_{101}}$ are exactly the same as the results proposed by Challamel and Girhammar [11]. Following the notation due to these authors, the dimensionless quantities are introduced

$$\hat{x} = \frac{x}{L}, \text{ and } n = \frac{\mathcal{N}^a}{\mathcal{N}^a_\infty} = \frac{\mathcal{N}^b}{\mathcal{N}^b_\infty}, \tag{2.40}$$

where

$$\mathcal{N}^a_\infty = -\mathcal{N}^b_\infty = -\left(1 - \frac{C^a_3 + C^b_3}{C^a_3 + C^b_3 + \frac{C^a_1 C^b_1 (h^a + h^b)^2}{4(C^a_1 + C^b_1)}}\right) \frac{2M_0}{h^a + h^b} \tag{2.41}$$

is the normal force associated with the full composite beam. In Fig. 2.12, the $\hat{x} - n$ diagram is shown for various values of parameter $\hat{\alpha}$, which is defined as $\hat{\alpha} = \alpha_T L$ and is proportional to the interlayer tangential stinesses. The results shown in Fig.2.12 correspond perfectly with the results proposed by Challamel and Girhammar [11]. It is also noticed that for this example the distribution of the total moment M_0 between the layers has no influence on the normal forces, axial strains and tangential interlayer traction in the composite beam.

2.7 Conclusions

Different mathematical models for analytical studying the mechanical behaviour of linear elastic multi-layer Reissner's composite beam with interlayer slip and uplift between the layers have been presented. The analytical studies have been carried out to evaluate the influence of different parameters on static and kinematic quantities of multi-layer beams with different combinations of contact conditions.
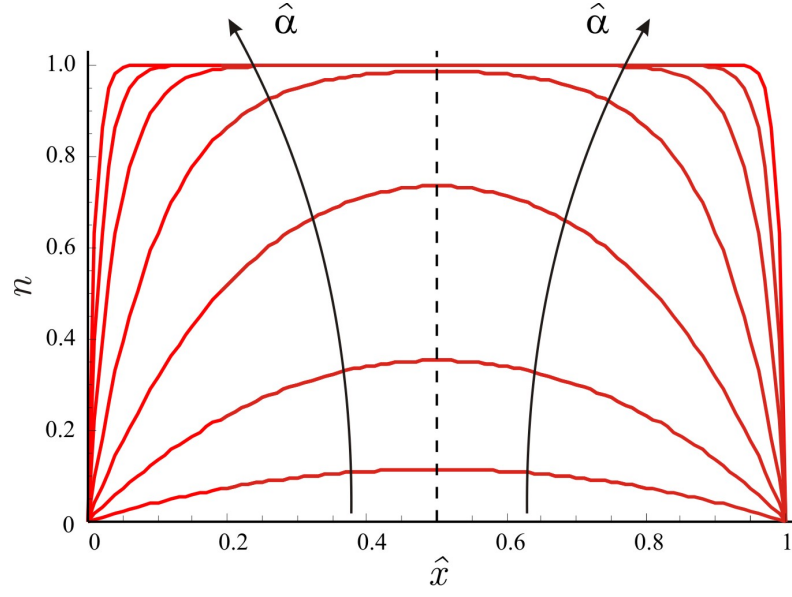
FIGURE 2.12: Influence of the dimensionless connection parameter $\hat{\alpha}$ on the dimensionless normalforce n, where $\hat{\alpha} \in \{1, 2, 4, 10, 25, 50, 100\}$

Based on the results of this analytical study and the parametric evaluations undertaken, the following conclusions can be drawn:

1. Different interlayer contact conditions have a considerably different influence on static and kinematic quantities of multi-layer beams. As a results, considerable differences in results between the models have been obtained.

2. The slip modulus has an influence on all displacements, while the interlayer uplift (Δw) and distortion ($\Delta \varphi$), remain unchanged for a given separation length under a variation of K_t.

3. The slip (Δu) increases with decreasing K_t and increasing the separation length. The shear forces are independent of K_t, and so are the normal interlayer tractions.

3 NON-LINEAR ANALYSIS OF MULTI-LAYER BEAMS WITH A RIGID INTERCONNECTION

3.1 Introduction

In this chapter, a finite-element formulation for geometrically exact multi-layer beams with a rigid interconnection is proposed. The number of layers is arbitrary and they are assembled in a composite beam with the interlayer connection allowing only for the occurrence of independent rotations of each layer. The interlayer slip and uplift are not considered, which results in the assembly equations that significantly simplify the problem. Instead of having horizontal and vertical displacement plus the cross-sectional rotation for each layer ($3n$, where n is the total number of layers), the basic unknown functions of the problem are reduced only to the horizontal and vertical displacement of the composite beam's reference axis and the cross-sectional rotation of each layer ($2 + n$). Due to the geometrically exact definition of the problem, the governing equations are non-linear in terms of basic unknown functions and the solution is obtained numerically. In general, each layer can have different geometrical and material properties, but since the layers are rigidly connected, the main application of this model is on homogeneous layered beams.

This model is very similar to the model presented by Vu Quoc *et al.* [75, 76] who used the Galerkin projection (see [61] and [74] for details) to obtain the computational formulation of the resulting non-linear equations of equilibrium in the static case (the formulation of the equations of motion in the general dynamic case was proposed, too), while in the present work the equilibrium equations are derived from the principle of virtual work. While the resulting numerical procedure is of necessity equal, here we focus on the actual transformation of the displacement

vector for each layer to the displacement vector of the beam reference line and show that it may be written in a remarkably elegant form allowing for simple numerical implementation. Furthermore, in the present work the problems with large number of layers are specifically analysed and the performance of the elements derived on the thick beam problems with pronounced cross-sectional warping is compared to the analytical results and the finite-element results obtained using 2D plane-stress elements.

3.2 Problem description

3.2.1 Position of the composite beam in the material co-ordinate system

An initially straight layered beam of length L and a cross-section composed of n parts with heights h_i and areas A_i, where i is an arbitrary layer $(i = 1, 2, \ldots, n)$, is shown in Fig. 3.1.
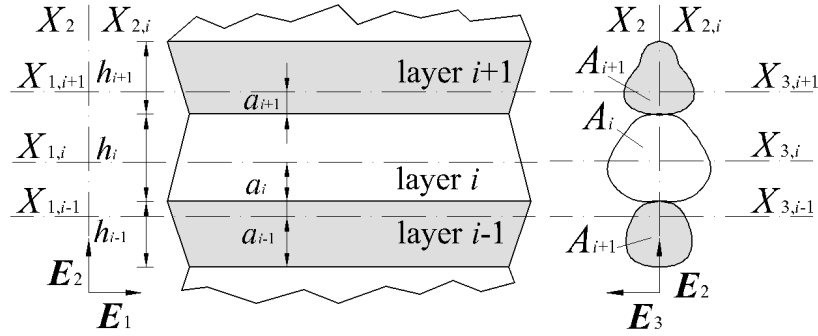
FIGURE 3.1: Material co-ordinate system of the composite beam

The layers are made of linear elastic material with E_i and G_i acting as Young's and shear moduli of each layer's material. Each layer has its own material co-ordinate system defined by an orthonormal triad of vectors $\boldsymbol{E}_{1,i}$, $\boldsymbol{E}_{2,i}$, $\boldsymbol{E}_{3,i}$, with axes $X_{1,i}, X_{2,i}, X_{3,i}$. Axes $X_{1,i}$ coincide with reference axes of each layer which are chosen arbitrarily (they can pass through the corresponding layer, but also fall outside of it) and are mutually parallel. Thus, a base vector $\boldsymbol{E}_1 = \boldsymbol{E}_{1,i}$ and a coordinate $X_1 = X_{1,i}$ can be introduced. The cross-sections of the layers have a common vertical principal axis X_2 defined by a base vector $\boldsymbol{E}_2 = \boldsymbol{E}_{2,i}$ (a condition

33

for a plane problem). However, for any chosen point on the beam, the co-ordinate $X_{i,2}$ changes for each layer i. Axes $X_{3,i}$ are mutually parallel but do not necessarily correspond with the horizontal principal axes of the layers' cross-sections, thus $X_3 = X_{3,i}$ and $\boldsymbol{E}_3 = \boldsymbol{E}_{3,i}$. The height of an arbitrary layer is denoted as h_i and the cross-sectional area by A_i. The distance from the bottom of a layer to the layer's reference axis is denoted as a_i (see Fig. 4.1). The first and the second moment of area of the cross-section A_i with respect to axis $X_{3,i}$ are defined as

$$S_i = \int\limits_{A_i} X_{2,i}\mathrm{d}A, \quad I_i = \int\limits_{A_i} (X_{2,i})^2 \mathrm{d}A. \tag{3.1}$$

3.2.2 Position of a layer of the composite beam in the spatial co-ordinate system

The reference axes of all layers in the initial undeformed state are defined by the unit vector $\boldsymbol{t}_{01}$ which closes an angle ψ with respect to the axis defined by the base vector $\boldsymbol{e}_1$ of the spatial co-ordinate system (see Fig. 3.2). The position of a material point $T(X_1, X_{2,i})$ in the undeformed initial configuration is defined at any layer by the vector

$$\boldsymbol{x}_{0,i}(X_1, X_{2,i}) = \boldsymbol{r}_{0,i}(X_1) + X_{2,i}\boldsymbol{t}_{02}, \tag{3.2}$$

where $\boldsymbol{r}_{0,i}(X_1)$ is the position of the intersection of the plane of the cross-section containing point T and the reference axis of the layer i in the undeformed state. Vector $\boldsymbol{t}_{0j}$ is defined as

$$\boldsymbol{t}_{0j} = \boldsymbol{\Lambda}_0 \boldsymbol{e}_j = \begin{bmatrix} \cos\psi & -\sin\psi \\ \sin\psi & \cos\psi \end{bmatrix} \boldsymbol{e}_j, \tag{3.3}$$

where $j = 1, 2$.

During the deformation the cross-sections of the layers remain planar but not necessarily orthogonal to their reference axes (Timoshenko beam theory with the Bernoulli hypothesis). The material base vector $\boldsymbol{E}_3$ remains orthogonal to the plane spanned by the spatial base $\boldsymbol{e}_1, \boldsymbol{e}_2$. Orientation of the cross-section of each
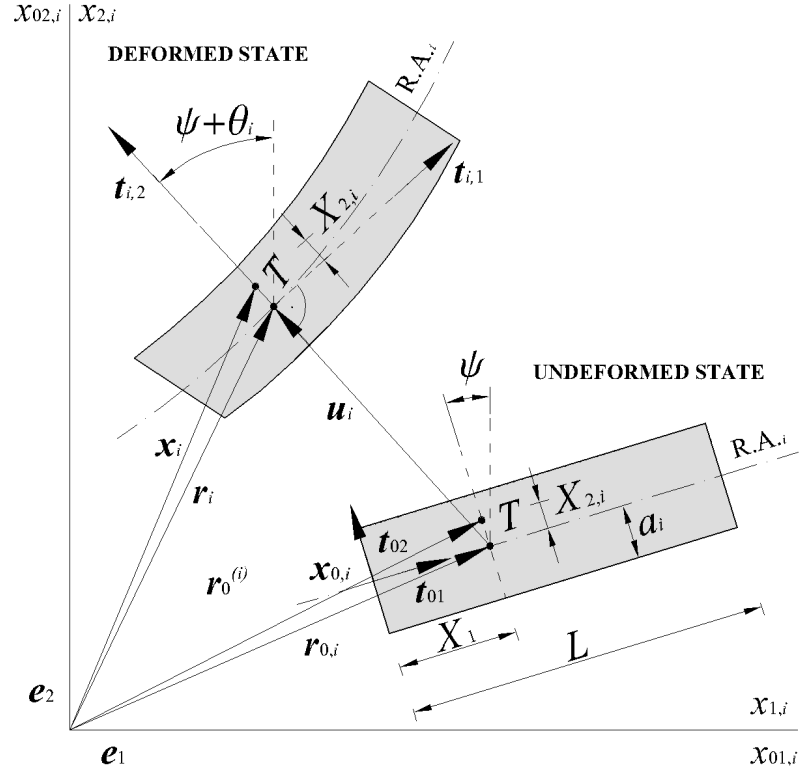
FIGURE 3.2: Position of a layer of the composite beam in undeformed and in deformed state

layer in the deformed state is defined by the base vectors

$$\boldsymbol{t}_{i,j} = \boldsymbol{\Lambda}_i \boldsymbol{e}_j = \begin{bmatrix} \cos(\psi + \theta_i) & -\sin(\psi + \theta_i) \\ \sin(\psi + \theta_i) & \cos(\psi + \theta_i) \end{bmatrix} \boldsymbol{e}_j, \qquad (3.4)$$

where index i denotes a layer and $j = 1, 2$. Rotation of the cross-section of each layer, denoted by θ_i, is entirely dependent on X_1, thus $\theta_i = \theta_i(X_1)$. The position of a material point T in the deformed state from Fig. 3.2 can be expressed as

$$\boldsymbol{x}_i(X_1, X_{2,i}) = \boldsymbol{r}_i(X_1) + X_{2,i}\boldsymbol{t}_{i,2}(X_1), \qquad (3.5)$$

where $\boldsymbol{r}_i(X_1)$ is the position of the intersection of the plane of the cross-section containing point T and the reference axis of layer i in the deformed state. The displacement between the undeformed and the deformed state is defined for each layer with respect to its reference axis, thus

$$\boldsymbol{r}_i(X_1) = \boldsymbol{r}_{0,i}(X_1) + \boldsymbol{u}_i(X_1). \qquad (3.6)$$

where $\boldsymbol{u}_i(X_1)$ is the vector of displacement of the layer's reference axis.

3.3   Governing equations

Since the layers are assumed to be connected rigidly, the displacements of each layer ($\boldsymbol{u}_i$) may be expressed in terms of some basic unknown functions $\boldsymbol{u}$ and θ_i, where $\boldsymbol{u}$ is a vector of displacements of an axis taken to be the whole beam's reference axis. The equations relating $\boldsymbol{u}_i$ to $\boldsymbol{u}$ and $\theta_1 \ldots \theta_n$ will be called the assembly equations and will be derived first. For each layer, the kinematic and constitutive equations are given next. Finally, the equilibrium equations are derived from the principle of virtual work.

3.3.1   Assembly equations

A section of a composite beam with arbitrary number of layers is shown in Fig. 3.3.
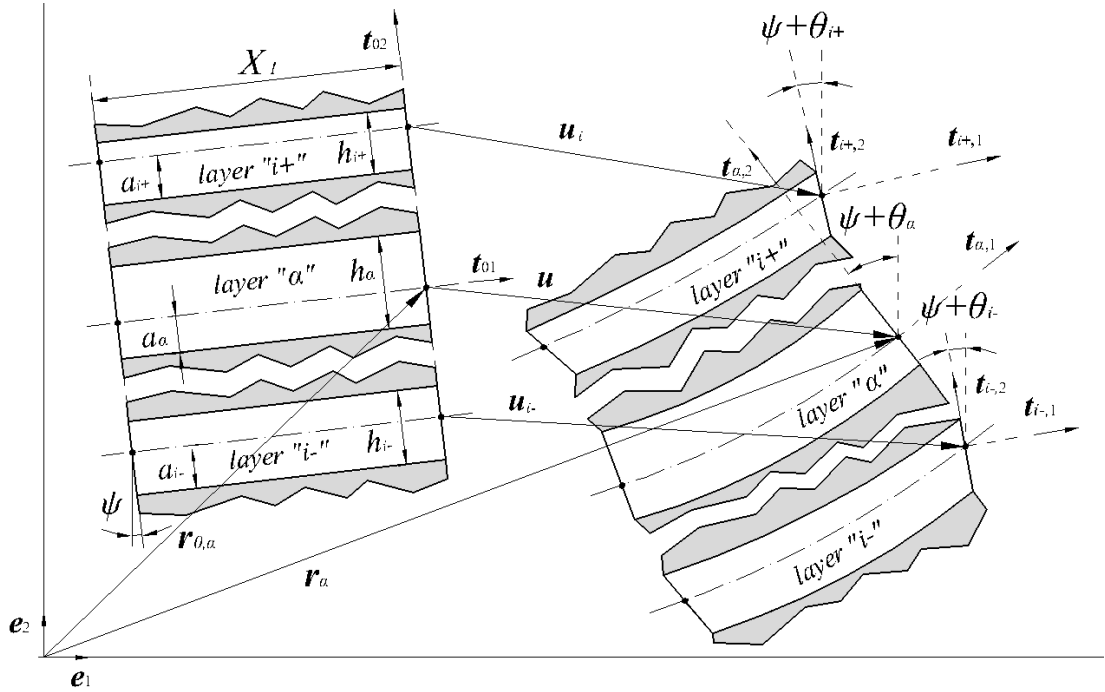
FIGURE 3.3: Undeformed and deformed state of the multilayer composite beam

Since in the present formulation no slip nor uplift are allowed between the layers of the composite beam, we can easily express displacement of each layer in terms of the displacement of an arbitrarily chosen main layer α (denoted by $\boldsymbol{u}$) and corresponding rotations θ_i. The reference axis of layer α then becomes the reference

axis of the composite beam. In Fig. 3.3 we observe the main layer α, an arbitrarily chosen layer lying above α, denoted by $i+$, and another layer lying below α, denoted by $i-$. In the deformed state the reference axes deform and the layers' cross-sections rotate, which is defined by the unit vectors $\boldsymbol{t}_{\alpha,2}$, $\boldsymbol{t}_{i+,2}$, $\boldsymbol{t}_{i-,2}$. Thus, for $i > \alpha$, which according to Fig. 3.3 corresponds to the layer $i+$, we obtain

$$\boldsymbol{u}_i = \boldsymbol{u} + a_i(\boldsymbol{t}_{i,2} - \boldsymbol{t}_{02}) - a_\alpha(\boldsymbol{t}_{\alpha,2} - \boldsymbol{t}_{02}) + \sum_{j=\alpha}^{i-1} h_j(\boldsymbol{t}_{j,2} - \boldsymbol{t}_{02}). \tag{3.7}$$

Similarly for $i < \alpha$, which corresponds to the layer $i-$ according to Fig. 3.3, we obtain

$$\boldsymbol{u}_i = \boldsymbol{u} + a_i(\boldsymbol{t}_{i,2} - \boldsymbol{t}_{02}) - a_\alpha(\boldsymbol{t}_{\alpha,2} - \boldsymbol{t}_{02}) + \sum_{j=i}^{\alpha-1} h_j(\boldsymbol{t}_{j,2} - \boldsymbol{t}_{02}). \tag{3.8}$$

Obviously, if $i = \alpha$

$$\boldsymbol{u}_i = \boldsymbol{u}, \tag{3.9}$$

and both equation (3.7) and equation (3.8) give the desired result (3.9) since a sum with the upper summation value smaller than the lower one is zero by definition. For an arbitrary layer i (lying below or above or coinciding with layer α) we thus have

$$\boldsymbol{u}_i = \boldsymbol{u} + a_i(\boldsymbol{t}_{i,2} - \boldsymbol{t}_{0,2}) - a_\alpha(\boldsymbol{t}_{\alpha,2} - \boldsymbol{t}_{0,2}) + \operatorname{sgn}(i - \alpha) \sum_{s=\zeta}^{\xi-1} h_s(\boldsymbol{t}_{s,2} - \boldsymbol{t}_{0,2}), \tag{3.10}$$

where

$$\operatorname{sgn}(i - \alpha) = \begin{cases} 1 & \text{if } i > \alpha, \\ 0 & \text{if } i = \alpha, \\ -1 & \text{if } i < \alpha, \end{cases} \tag{3.11}$$

and $\xi = \max(i; \alpha)$, $\zeta = \min(i; \alpha)$.

Using this relation we can express $\boldsymbol{u}_i$ in terms of our basic unknown functions $\boldsymbol{u}$ and θ_j, where $j \in [\zeta, \ldots, \xi]$. In other words the basic unknown functions of the problem are two components of the vector $\boldsymbol{u}$ and the rotations of each layer θ_i, making the number of total unknown functions $n + 2$. We can further express relation (3.10) in terms of ζ and ξ as

$$\boldsymbol{u}_i = \boldsymbol{u} + d_{i,\zeta}(\boldsymbol{t}_{\zeta,2} - \boldsymbol{t}_{0,2}) + d_{i,\xi}(\boldsymbol{t}_{\xi,2} - \boldsymbol{t}_{0,2}) + \sum_{s=\zeta+1}^{\xi-1} d_{i,s}(\boldsymbol{t}_{s,2} - \boldsymbol{t}_{0,2}), \tag{3.12}$$

where

$$d_{i,\zeta} = \text{sgn}(i-\alpha)(h_\zeta - a_\zeta), \quad d_{i,\xi} = \text{sgn}(i-\alpha)a_\xi \text{ and } d_{i,s} = \text{sgn}(i-\alpha)h_s. \quad (3.13)$$

3.3.2 Kinematic equations

Non-linear kinematic equations according to Reissner [48] are

$$\boldsymbol{\gamma}_i = \begin{Bmatrix} \epsilon_i \\ \gamma_i \end{Bmatrix} = \boldsymbol{\Lambda}_i^\mathsf{T} \boldsymbol{r}_i' - \boldsymbol{E}_1 = \boldsymbol{\Lambda}_i^\mathsf{T}(\boldsymbol{t}_{01} + \boldsymbol{u}_i') - \boldsymbol{E}_1, \quad (3.14)$$

$$\kappa_i = \theta_i', \quad (3.15)$$

where $\epsilon_i, \gamma_i, \kappa_i$ are the axial and shear strain of the reference axis of i-th layer as well as the rotational strain (infinitesimal change of the cross-sectional rotation) as functions of only X_1. The differentiation with respect to X_1 is denoted as $(\bullet)'$. In relations (3.14) and (3.15), the strains of each layer are expressed in terms of the unknown functions $\boldsymbol{u}_i$ and θ_i or, using (3.12), in terms of the basic unknown functions $\boldsymbol{u}$ and θ_j $(j \in [\zeta, \ldots, \xi])$.

A relationship between these strain measures and the continuum-based strain tensors may be established by incorporating the Bernoulli hypothesis into a specific strain tensor through an appropriate definition of the deformation gradient (see e.g. [28, 29, 62] for details). As shown in [28] the relationship becomes particularly clear for the case of vanishing shear strains (as it does in the Euler–Bernoulli beam theory), whereby the translational strain measures of (3.14) coincide with the first column of the Biot strain tensor.

When the shear strains do not vanish, the above Reissner's strain measures become more difficult to relate to the Biot strain tensor, as that tensor by definition depends on the rotation obtained from the deformation gradient by polar decomposition (see e.g. [40]), rather than the rotation of the cross section and in this case the two rotations differ. Also, it becomes additionally difficult to reconcile the classical theory of simple materials in which the strain tensors depend only on the deformation gradient with the fact that the shear-deformable Reissner's beam theory is in fact a unidimensional example of a generalised Cosserat continuum.

As is well-known (see e.g. [40]) all the strain tensor definitions reduce to the same linear strain-displacement result when higher-terms in the deformation gradient are set to vanish.

3.3.3 Constitutive equations

The normal strain of a fibre at the distance $X_{2,i}$ from the reference axis of the layer i is defined as

$$\varepsilon_i = \varepsilon_i(X_1, X_{2,i}) = \epsilon_i(X_1) - X_{2,i}\kappa_i(X_1), \tag{3.16}$$

and the normal stress for a linear elastic material is defined as

$$\sigma_i = \sigma_i(X_1, X_{2,i}) = E_i\varepsilon_i(X_1, X_{2,i}), \tag{3.17}$$

where E_i is Young's modulus of the material of layer i. From (3.16) and (3.17) it is obvious that the distribution of normal stresses over the layer's height is linear. The stress resultants read

$$N_i = \int_{A_i} \sigma_i \mathrm{d}A, \tag{3.18}$$

$$T_i = G_i k_i A_i \gamma_i, \tag{3.19}$$

$$M_i = -\int_{A_i} X_{2,i}\sigma_i \mathrm{d}A, \tag{3.20}$$

where N_i, T_i, M_i are the axial force, shear force and bending moment with respect to the reference axis of layer i, respectively. G_i is the shear modulus of material of layer i and k_i is the shear correction coefficient [12]. Combining relations (3.16-3.20) we finally obtain

$$\begin{Bmatrix} N_i \\ T_i \\ M_i \end{Bmatrix} = \begin{Bmatrix} \boldsymbol{N}_i \\ M_i \end{Bmatrix} = \boldsymbol{C}_i \begin{Bmatrix} \boldsymbol{\gamma}_i \\ \kappa_i \end{Bmatrix}, \tag{3.21}$$

where S_i and I_i are the first and the second moment of area of the cross-section of layer i, and

$$
\boldsymbol{C}_i = \begin{bmatrix} E_i A_i & 0 & -E_i S_i \\ 0 & G_i k_i A_i & 0 \\ -E_i S_i & 0 & E_i I_i \end{bmatrix},
\tag{3.22}
$$

is the constitutive matrix of layer i. By substituting (3.14), (3.15) and (3.12) in (3.21) we can express the internal forces and bending moments of each layer in terms of basic unknown functions $\boldsymbol{u}$ and θ_s ($s \in [\zeta, \ldots, \xi]$).

Clearly, the above exposition of linear elasticity may be intuitively acceptable, but a question may be posed as to whether this is a result which may be obtained by introducing the Bernoulli hypothesis into a continuum-based linear elasticity.

As shown in [28], the answer to this question is affirmative if (i) the beam theory considered is shear-rigid and (ii) the linear relationship on the continuum level is established between the Biot strain thensor and the Biot stress tensor. In contrast, the popular Saint Venant–Kirchhoff material in which the Green–Lagrange strain tensor is linearly related to the second Piola–Kirchhoff stress tensor would not result in the linear elastic relationships between Reissner' strain measures and the cross-sectional stress resultants as defined above. Still, the first-order approximation of the Saint Venant–Kirchhoff material as applied to Reissner's beam, in which the higher order terms in the strain measures are neglected, indeed coincides with the linear elastic beam material as given here.

For a shear-deformable beam, as explained in the previous section, it is more difficult to establish an energy-conjugate stress–strain couple which enjoys a linear elastic relationship and results in the linear elastic relationship between Reissner's strain measures and the stress resultants (3.21). Nonetheless, such an attempt is made in [30], while in [29], manifestations of a Saint Venant–Kirchhoff material and a specific hyperelastic material on the loss of linearity between Reissner's strain measures and the beam stress resultants have been investigated in detail. Again, as long as the Reissner's strain measures are small enough so that the non-linearities between them and the stress resultants may be neglected, the resulting linear elastic relationship is precisely the one in which the two elasticity parameters (say Young's modulus and Poisson's ratio) take their correct physical meaning.

3.3.4 Equilibrium equations - the principle of virtual work

According to the principle of virtual work for a static problem, the work of internal forces over virtual strains is equal to the work of external forces over virtual displacements:

$$V \equiv V^{int} - V^{ext} = 0, \tag{3.23}$$

where, for a multilayer beam composed of n layers, the virtual work of internal and external forces are defined as

$$V^{int} = \sum_{i=1}^{n} \int_0^L \left(\overline{\boldsymbol{\gamma}}_i \cdot \boldsymbol{N}_i + \overline{\kappa}_i M_i \right) \mathrm{d}X_1, \tag{3.24}$$

$$V^{ext} = \sum_{i=1}^{n} \left[\int_0^L \left(\overline{\boldsymbol{u}}_i \cdot \boldsymbol{f}_i + \overline{\theta}_i w_i \right) \mathrm{d}X_1 + \overline{\boldsymbol{u}}_{i,0} \cdot \boldsymbol{F}_{i,0} + \overline{\theta}_{i,0} W_{i,0} + \right.$$
$$\left. + \overline{\boldsymbol{u}}_{i,L} \cdot \boldsymbol{F}_{i,L} + \overline{\theta}_{i,L} W_{i,L} \right]. \tag{3.25}$$

The summation counter i represents the beam layers while indices 0 and L represent the beam ends where the boundary point forces $\boldsymbol{F}_{i,0}$, $\boldsymbol{F}_{i,L}$ and bending moments $W_{i,0}$, $W_{i,L}$ are applied. The distributed force and moment loads are denoted by $\boldsymbol{f}_i$ and w_i. The virtual strains and curvature are denoted by $\overline{\boldsymbol{\gamma}}_i$ and $\overline{\kappa}_i$, and virtual displacements and rotations by $\overline{\boldsymbol{u}}_i$ and $\overline{\theta}_i$. Since

$$\overline{\sin(\psi + \theta_i)} = \overline{\theta}_i \cos(\psi + \theta_i) \tag{3.26}$$

$$\overline{\cos(\psi + \theta_i)} = -\overline{\theta}_i \sin(\psi + \theta_i) \tag{3.27}$$

from (3.4) it follows that

$$\overline{\boldsymbol{t}}_{i,1} = \overline{\theta}_i \boldsymbol{t}_{i,2}, \tag{3.28}$$

$$\overline{\boldsymbol{t}}_{i,2} = -\overline{\theta}_i \boldsymbol{t}_{i,1}, \tag{3.29}$$

$$\overline{\boldsymbol{\Lambda}}_i = \overline{\theta}_i \boldsymbol{t}_3 \boldsymbol{\Lambda}_i, \tag{3.30}$$

where $\hat{t}_3 = \begin{bmatrix} 0 & -1 \\ 1 & 0 \end{bmatrix}$. Using (3.30), from (3.14) and (3.15) we can then obtain

$$\left\{ \begin{array}{c} \overline{\gamma}_i \\ \overline{\kappa}_i \end{array} \right\} = \left\{ \begin{array}{c} \mathbf{\Lambda}_i^\mathsf{T} \left[\overline{\boldsymbol{u}}_i' - \overline{\theta}_i \hat{\boldsymbol{t}}_3 (\boldsymbol{t}_{01} + \boldsymbol{u}_i') \right], \\ \overline{\theta}_i', \end{array} \right\} = \boldsymbol{L}_i \boldsymbol{D}_i \left\{ \begin{array}{c} \overline{\boldsymbol{u}}_i \\ \overline{\theta}_i \end{array} \right\} \qquad (3.31)$$

where

$$\boldsymbol{L}_i = \begin{bmatrix} \mathbf{\Lambda}_i^\mathsf{T} & \mathbf{0} \\ \mathbf{0}^\mathsf{T} & 1 \end{bmatrix}, \qquad (3.32)$$

$$\boldsymbol{D}_i = \begin{bmatrix} \frac{\mathrm{d}}{\mathrm{d}X_1} \boldsymbol{I} & -\hat{\boldsymbol{t}}_3 \left(\boldsymbol{t}_{01} + \boldsymbol{u}_i' \right) \\ \mathbf{0}^\mathsf{T} & \frac{\mathrm{d}}{\mathrm{d}X_1} \end{bmatrix}, \qquad (3.33)$$

and $\boldsymbol{I}$ represents the 2×2 unity matrix. Using this relation, the virtual work becomes

$$V \equiv \sum_{i=1}^{n} \left[\int_0^L \left(\left\langle \overline{\boldsymbol{u}}_i^\mathsf{T} \quad \overline{\theta}_i \right\rangle \boldsymbol{D}_i^\mathsf{T} \boldsymbol{L}_i^\mathsf{T} \left\{ \begin{array}{c} \boldsymbol{N}_i \\ M_i \end{array} \right\} - \left\langle \overline{\boldsymbol{u}}_i^\mathsf{T} \quad \overline{\theta}_i \right\rangle \left\{ \begin{array}{c} \boldsymbol{f}_i \\ w_i \end{array} \right\} \right) \mathrm{d}X_1 - \right.$$
$$\left. - \left\langle \overline{\boldsymbol{u}}_i^\mathsf{T} \quad \overline{\theta}_i \right\rangle_0 \left\{ \begin{array}{c} \boldsymbol{F}_{i,0} \\ W_{i,0} \end{array} \right\} - \left\langle \overline{\boldsymbol{u}}_i^\mathsf{T} \quad \overline{\theta}_i \right\rangle_L \left\{ \begin{array}{c} \boldsymbol{F}_{i,L} \\ W_{i,L} \end{array} \right\} \right] = 0. \qquad (3.34)$$

Since, using (3.28) and (3.29) from (3.12), it follows that

$$\overline{\boldsymbol{u}}_i = \overline{\boldsymbol{u}} - d_{i,\zeta} \overline{\theta}_\zeta \boldsymbol{t}_{\zeta,1} - d_{i,\xi} \overline{\theta}_\xi \boldsymbol{t}_{\xi,1} - \sum_{s=\zeta+1}^{\xi-1} d_{i,s} \overline{\theta}_s \boldsymbol{t}_{s,1}, \qquad (3.35)$$

we can perform the transformation

$$\left\langle \overline{\boldsymbol{u}}_i^\mathsf{T} \quad \overline{\theta}_i \right\rangle = \left\langle \overline{\boldsymbol{u}}^\mathsf{T} \quad \overline{\theta}_1 \quad \overline{\theta}_2 \quad \dots \quad \overline{\theta}_{n-1} \quad \overline{\theta}_n \right\rangle \boldsymbol{B}_i^\mathsf{T} = \overline{\boldsymbol{p}}_f^\mathsf{T} \boldsymbol{B}_i^\mathsf{T}, \qquad (3.36)$$

where $\overline{\boldsymbol{p}}_f$ is the vector of basic virtual unknown functions $\overline{\boldsymbol{u}}$ and $\overline{\theta}_i$ and $\boldsymbol{B}_i$ is the matrix of transformation defined as

$$\boldsymbol{B}_i = \begin{bmatrix} \boldsymbol{I} & \mathbf{0} & \dots & \mathbf{0} & -d_{i,\zeta} \boldsymbol{t}_{\zeta,i} & \dots & -d_{i,\xi} \boldsymbol{t}_{\xi,1} & \mathbf{0} & \dots & \mathbf{0} \\ \mathbf{0}^\mathsf{T} & 0 & \dots & 0 & \delta_{i\zeta} & \dots & \delta_{i\xi} & 0 & \dots & 0 \end{bmatrix}, \qquad (3.37)$$

where δ_{ij} is the Kronecker symbol defined as

$$\delta_{ij} = \begin{cases} 1 & \text{if } i = j, \\ 0 & \text{otherwise.} \end{cases} \tag{3.38}$$

Using (3.36) expression (3.34) becomes

$$V \equiv \sum_{i=1}^{n} \left[\int_0^L \overline{\boldsymbol{p}}_f^\mathsf{T} \boldsymbol{B}_i^\mathsf{T} \left(\boldsymbol{D}_i^\mathsf{T} \boldsymbol{L}_i^\mathsf{T} \boldsymbol{C}_i \left\{ \begin{matrix} \gamma_i \\ \kappa_i \end{matrix} \right\} - \left\{ \begin{matrix} \boldsymbol{f}_i \\ w_i \end{matrix} \right\} \right) \mathrm{d}X_1 - \overline{\boldsymbol{p}}_{f,0}^\mathsf{T} \boldsymbol{B}_{i,0}^\mathsf{T} \left\{ \begin{matrix} \boldsymbol{F}_{i,0} \\ W_{i,0} \end{matrix} \right\} - \right.$$
$$\left. - \overline{\boldsymbol{p}}_{f,L}^\mathsf{T} \boldsymbol{B}_{i,L}^\mathsf{T} \left\{ \begin{matrix} \boldsymbol{F}_{i,L} \\ W_{i,L} \end{matrix} \right\} \right] = 0. \tag{3.39}$$

Matrices $\boldsymbol{B}_{i,0}$ and $\boldsymbol{B}_{i,L}$ are evaluated for $X_1 = 0$ and $X_1 = L$, respectively.

3.4 Solution procedure

The presented governing equations are highly non-linear and cannot be solved in a closed form. Thus, it is necessary to choose in advance the shape of test functions $(\overline{\boldsymbol{u}}, \overline{\theta}_i)$, and later also the shape of trial functions $(\boldsymbol{u}, \theta_i)$. For a finite number of nodes (N) on the beam it is assumed that the virtual displacements and rotations are known at the nodes $(\overline{\boldsymbol{u}}_j, \overline{\theta}_{i,j})$ and interpolated between the nodes. The interpolation of functions of virtual displacements and rotations can be written as

$$\overline{\boldsymbol{p}}_f = \left\{ \begin{matrix} \overline{\boldsymbol{u}}(X_1) \\ \overline{\theta}_1(X_1) \\ \vdots \\ \overline{\theta}_n(X_1) \end{matrix} \right\} = \sum_{j=1}^{N} \boldsymbol{\Psi}_j(X_1) \left\{ \begin{matrix} \overline{\boldsymbol{u}}_j \\ \overline{\theta}_{1,j} \\ \vdots \\ \overline{\theta}_{n,j} \end{matrix} \right\} = \sum_{j=1}^{N} \boldsymbol{\Psi}_j(X_1) \overline{\boldsymbol{p}}_j, \tag{3.40}$$

where $\boldsymbol{\Psi}_j(X_1)$ is a $(2+n) \times (2+n)$ matrix containing interpolation functions and $\overline{\boldsymbol{p}}_j$ is a vector containing virtual nodal displacements and rotations at node j. Using interpolations (3.40) we can write the expression for the virtual work (3.39) as

$$V \equiv \sum_{j=1}^{N} \overline{\boldsymbol{p}}_j^\mathsf{T} \boldsymbol{g}_j = 0, \tag{3.41}$$

where

$$g_j = \sum_{i=1}^{n} \left[\int_0^L \mathbf{\Psi}_j^\mathsf{T} \mathbf{B}_i^\mathsf{T} \left(\mathbf{D}_i^\mathsf{T} \mathbf{L}_i^\mathsf{T} \mathbf{C}_i \begin{Bmatrix} \gamma_i \\ \kappa_i \end{Bmatrix} - \begin{Bmatrix} f_i \\ w_i \end{Bmatrix} \right) \mathrm{d}X_1 - \left(\delta_{j1} \mathbf{B}_{i,0}^\mathsf{T} \begin{Bmatrix} \mathbf{F}_{i,0} \\ W_{i,0} \end{Bmatrix} + \right.$$
$$\left. + \delta_{jN} \mathbf{B}_{i,L}^\mathsf{T} \begin{Bmatrix} \mathbf{F}_{i,L} \\ W_{i,L} \end{Bmatrix} \right) \right] \tag{3.42}$$

is the vector of residual forces for the node j. Since $\overline{\mathbf{p}}_j$ is arbitrary, from (3.41) it follows that for any node j

$$g_j = \mathbf{0}. \tag{3.43}$$

Note that vector g_j is expressed only in terms of the unknown functions $\mathbf{u}, \theta_1, \theta_2, \ldots$ $\ldots, \theta_{n-1}, \theta_n$, which are contained in matrices $\mathbf{D}_i$, $\mathbf{B}_i$, $\mathbf{L}_i$ and in vector $\begin{Bmatrix} \gamma_i \\ \kappa_i \end{Bmatrix}$. Relation (3.43) is highly non-linear and is not solvable analytically in terms of the unknown functions. Thus, to solve the problem numerically the nodal vector of residual forces is first expanded in Talyor's series up to a linear term as

$$g_j + \Delta g_j = \mathbf{0}, \quad j = 1, 2, \ldots, N. \tag{3.44}$$

The linearization of the nodal vector of residual forces Δg_j and element tangent stiffness matrix $\mathbf{K}$ derivation is shown in detail in Appendix A. We finally obtain

$$\Delta \mathbf{p} = -\mathbf{K}^{-1} \mathbf{g}, \tag{3.45}$$

where $\Delta \mathbf{p}$ is the vector of element nodal increments of the unknown functions produced in the process of linearization of the nodal vectors of residual forces g_j (see Appendix) and $\mathbf{g}$ is the element vector of residual forces. The global stiffness matrix and the vector of residual forces are assembled from $\mathbf{K}$ and $\mathbf{g}$ given here using the standard finite-element assembly procedure (see [80]). The solution is obtained iteratively using Newton-Raphson method until a satisfying accuracy is achieved.

3.5 Numerical Examples

In this section we compare the presented formulation to a non-linear formulation for multilayer beams proposed by Vu Quoc *et al.* [76] and to the plane elasticity theory [67] in linear analysis or the solutions obtained using non-linear plane-stress elements. As explained earlier, a linear elastic continuum relationship as defined by the Saint Venant–Kirchoff material is consistent with the linear elastic relationship in the Reissner beam only for small strains, even though the actual displacements and rotations may be large. The examples presented here, therefore, are either of the small strain–small displacement-rotation type or the small strain–large displacement-rotation type. All results presented in these examples have been obtained using computer package *"Wolfram Mathematica"*.

3.5.1 Roll-up manoeuvre

A comparison of the presented formulation with [74] and [76] is given for the roll-up manoeuvre. A cantilever beam is subjected to a pure bending by applying a moment $W = 2EI\pi/L$ at the beam tip, where EI is the bending stiffness and L is the length of the beam. Such a bending moment forces the beam to roll up into an exact circle and the beam tip is displaced to coincide exactly with the clamped end, with the displacement having a component $u(L) = -L$ along the beam length, a zero transverse component $(v(L) = 0)$, and a rotation $\theta(L) = 2\pi$. The results for a single-layer beam and a sandwich beam are shown below.

3.5.1.1 Single-layer beam

Material and geometrical properties are chosen according to [76], where only stiffnesses $EA = 2$, $GkA = 2$, $EI = 2$ were given. Thus, $h = \sqrt{12}$, $b = \frac{1}{\sqrt{12}}$, $A = bh = 1$, $I = \frac{bh^3}{12} = 1$, $E = Gk = 2$ are used in the present work for a rectangular cross-section, which give exactly the stiffnesses from [76]. The beam of length $L = 1$ is divided in five linear elements. Table 3.1 shows the results obtained using the presented formulation, the results from [76] and the analytical solution. Only

three iterations in the non-linear Newton-Raphson solution procedure with displacement tolerance 10^{-6} are needed to obtain convergence. Improved accuracy of the present formulation in comparison with [76] is probably due to different arithmetic precision. However, the results show excellent agreement with the analytical solution. The finite-element deformed shape is a pentagon with the nodes lying on the circle of the exact deformed shape [76].

TABLE 3.1: Comparison of the results for the roll-up manoeuvre for a single-layer beam

	$u(L)$	$v(L)$	$\theta(L)$
Present formulation	-0.99999	1.9415E-17	6.28319
Vu-Quoc *et al.*	-1.00003	2.92110E-09	6.28300
Exact solution	-1	0	6.28319

3.5.1.2 Sandwich beam

A sandwich beam of length $L = 1$ with three identical layers of height $h_i = 0.02\sqrt{3}$, $i = 1, 2, 3$ [74] is considered. Using the so-called "normal" moment distribution over the layers [74]

$$W_1 : W_2 : W_3 = 7 : 13 : 7, \tag{3.46}$$

where $W = W_1 + W_2 + W_3$ is the tip bending moment for the roll-up manoeuvre, the sandwich beam behaves as a single-layer beam with a plane cross-section in the deformed state, thus, at the free end, $\theta_1 = \theta_2 = \theta_3 = \theta = 2\pi$. Using the stiffnesses from [74] $E_i A_i = 2 \cdot 10^6$, $G_i k_i A_i = 2 \cdot 10^6$, $E_i I_i = 200$, $(i = 1, 2, 3)$, and height h_i, the following geometrical and material properties are chosen $b_i = \frac{\sqrt{3}}{3}$, $A_i = b_i h_i$, $I_i = \frac{b_i h_i^3}{12}$, $E_i = G_i k_i = 10^8$, $(i = 1, 2, 3)$. The bending stiffness of the entire beam is $EI = E_i b_i (3h_i)^3 / 12 = 5400$. In Table 3.2 the results obtained by the present formulation, the formulation proposed by [74] and the analytical solution are shown. Five linear elements and three iterations are needed for the displacement convergence tolerance 10^{-6}.

Both the present formulation, as well as [74] show excellent agreement with the analytical results.

TABLE 3.2: Comparison of the results for the roll-up manoeuvre for a sandwich beam, $(i = 1, 2, 3)$

	$u(L)$	$v(L)$	$\theta_i(L)$
Present formulation	-0.999999	3.29089E-17	6.28319
Vu-Quoc and Deng	-0.999999	-2.15292E-09	6.28319
Exact solution	-1	0	6.28319

3.5.2 Thick cantilever beam tests

The presented multi-layer beam model can be applied to a homogeneous beam divided into a finite number of equal laminae. In that case all layers have identical geometrical and material properties with no interlayer slip and uplift. Since independent cross-sectional rotations of each layer are allowed, the initially straight cross-sections are allowed to turn into a piecewise linear cross-section in the deformed state. According to the 2D plane-stress theory of elasticity [67], the cross-sections in the deformed state do not remain planar and the cross-sectional warping indeed occurs. Obviously, the present multi-layer beam model is capable of simulating this effect piece-wise and here we test how well it may reproduce the actual 2D plane-stress results.

The comparison is additionally made with 2D plane-stress finite-element solution for various numbers of layers and finite elements. The analysis is first performed for a geometrically linear problem (small displacements and rotations). After that, a comparison between the multi-layer beam and the 2D plane-stress finite-element solution is presented for the non-linear problem with large displacements and rotations.

3.5.2.1 Thick cantilever beam - Linear analysis

A thick cantilever beam with a narrow rectangular cross-section of unit width subjected to a transverse force F at the free end is considered as shown in Fig. 3.4.
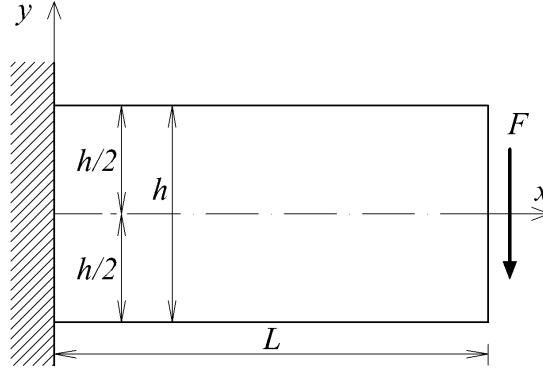
FIGURE 3.4: Cantilever beam loaded at the free end

According to [67] the boundary conditions for this problem read

$$\tau_{xy}(x, \pm\frac{h}{2}) = 0, \tag{3.47}$$

$$\sigma_{yy}(x, \pm\frac{h}{2}) = 0, \tag{3.48}$$

$$\sigma_{xx}(L, y) = 0, \tag{3.49}$$

$$\int_{-\frac{h}{2}}^{\frac{h}{2}} \sigma_{xx}(0, y)\mathrm{d}y = 0, \tag{3.50}$$

$$\int_{-\frac{h}{2}}^{\frac{h}{2}} \tau_{xy}(x, y)\mathrm{d}y = -F, \text{ for } x = 0, L, \tag{3.51}$$

and the corresponding stress distribution is

$$\sigma_{xx}(x, y) = \frac{Fy}{I}(L - x), \tag{3.52}$$

$$\sigma_{yy}(x, y) = 0, \tag{3.53}$$

$$\tau_{xy}(x, y) = \frac{Fy^2}{2I} - \frac{3}{2}\frac{F}{A}. \tag{3.54}$$

A linear distribution of normal stresses in the x-direction over the beam's height, zero normal stresses in the y-direction and a parabolic distribution of shear stresses over the beam's height is obtained. Normal stresses in the x-direction decrease linearly from $x = 0$ to $x = L$, while the shear stresses remain constant over the beam's length. This stress distribution is invariant to the displacement boundary conditions, which are introduced afterwards. According to [5], if the displacement

48

boundary conditions are given as

$$u(0, y) = v(0, y) = 0, \tag{3.55}$$

the displacement functions cannot be determined. The displacement boundary conditions have to be defined at discrete points with specified x and y co-ordinates. There are several possibilities to approximately model fully clamped end, and here we use

$$u(0, 0) = 0, \tag{3.56}$$

$$v(0, 0) = 0, \tag{3.57}$$

$$\left(\frac{\partial u}{\partial y} \right)_{\substack{x=0 \\ y=0}} = 0, \tag{3.58}$$

where the displacements and the cross-sectional rotation are inhibited only at the point (0,0). Then, the displacement functions read

$$u(x, y) = \frac{Fy}{EI} \left[Lx - \frac{x^2}{2} + \frac{y^2}{6}(2 + \nu) \right], \tag{3.59}$$

$$v(x, y) = \frac{F}{EI} \left[-\frac{Lx^2}{2} + \frac{x^3}{6} + \frac{\nu y^2}{2}(x - L) \right] - \frac{3}{2} \frac{Fx}{GA}. \tag{3.60}$$

Obviously, the cross-sectional warping is allowed over the height of the "clamped" end, as of course is also over all the other cross-sections. To model this problem numerically using the multi-layer beam elements, the beam from Fig. 3.4 is divided in N linear beam elements and n equal laminae to obtain a multilayer beam. Also, the mesh for 2D plane-stress finite-element analysis is made of N columns and n rows, and the calculation is carried out using the package FEAP [80]. The boundary conditions for the multi-layer composite beam and for the two-dimensional finite-element analysis are given according to (3.47)-(3.51) and (3.56)-(3.58). The distributed load at the beam ends is applied as the corresponding nodal load, while inhibiting the displacements and the cross-sectional rotation of the middle layer(s) at the left end of the beam. Positions of the reference axes for layers are $a_i = h_i/2$, except for the two middle layers where $a_{\frac{n}{2}} = h_{\frac{n}{2}}$ and $a_{\frac{n}{2}+1} = 0$ (even number of layers is used). It was shown that different choices of the main layer α do not affect the results. Shear correction coefficient $k_i = 1$ is

used for the multi-layer beam model in all examples.

For the numerical values $L = 100$, $h = 50$, $b = 1$, $F = -0.1$, $E = 1$, $\nu = 0$, the displacements at the edges of the left-hand end cross-section $(0, \pm\frac{h}{2})$ and at the beam's axis at the free end $(L, 0)$ for the multi-layer beam and 2D plane-stress finite-element models are shown in Tables 3.3 and 3.4. Two types of 2D plane-stress finite elements from the FEAP library are used; the displacement based element [80] and the element based on the enhanced strain concept [59, 80]. The analytical solutions read $u(0, \pm\frac{h}{2}) = \pm0.05$, $v(0, \pm\frac{h}{2}) = 0$, $u(L, 0) = 0$ and $v(L, 0) = -3.8$ [67]. It can be noticed that with considerably smaller number of degrees of freedom (D.O.F.), in comparison with the 2D plane stress finite-element models, the multilayer beam model presents a better approximation of the analytical solution. Since in this example the transverse strain is not considered ($\nu = 0$), the two-dimensional domain can be accurately modelled using the multi-layer beam model, which, just as the theory of elasticity solution, gives zero vertical displacements over the entire left-hand end cross-section. The 2D plane-stress finite-element models give zero vertical displacement at the left-hand end cross-section only at the beam's axis $(0, 0)$, while for the other positions in the cross-section only converge towards this result as the finite-element mesh is refined. Fig. 3.5 shows the warping of the left-hand end cross-section of the beam for the models considered.

TABLE 3.3: Displacements at the left-hand end of the beam for the multilayer beam model and the 2D plane-stress finite-element models for $\nu = 0$ (analytical solution: $u = \pm0.05$, $v = 0$)

Mesh	Multi-layer beam			2D displacement-based elements			2D enhanced-strain elements		
$n \times N$	D.O.F.	$u(0, \pm\frac{h}{2})$	$v(0, \pm\frac{h}{2})$	D.O.F.	$u(0, \pm\frac{h}{2})$	$v(0, \pm\frac{h}{2})$	D.O.F.	$u(0, \pm\frac{h}{2})$	$v(0, \pm\frac{h}{2})$
4×2	18	± 0.0375	0	30	±0.1022	0.0013	30	±0.0374	-0.0018
8×4	50	± 0.0469	0	90	±0.0950	0.0070	90	±0.0463	-0.0012
16×8	162	± 0.0492	0	306	±0.0715	0.0061	306	±0.0489	-0.0005
32×16	578	± 0.0498	0	1122	±0.0578	0.0029	1122	±0.0497	-0.0002

TABLE 3.4: Displacements at the free end of the beam's axis for the multilayer beam model and the 2D plane-stress finite-element models for $\nu = 0$ (analytical solution: $u = 0$, $v = -3.8$)

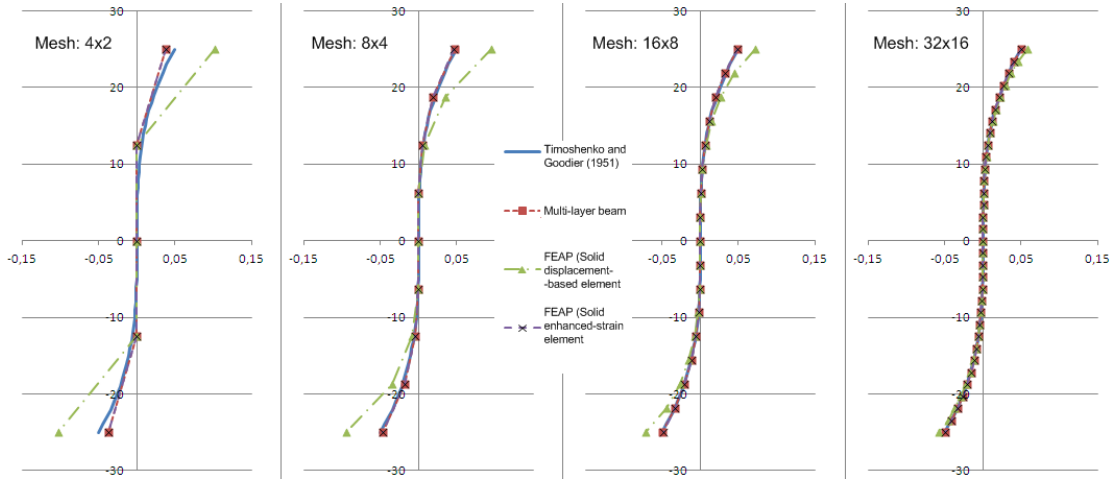| Mesh	Multi-layer beam			2D displacement-based elements			2D enhanced-strain elements		
$n \times N$	D.O.F.	$u(L, 0)$	$v(L, 0)$	D.O.F.	$u(L, 0)$	$v(L, 0)$	D.O.F.	$u(L, 0)$	$v(L, 0)$
4×2	18	0	-3.5500	30	0	-2.7471	30	0	-3.5506
8×4	50	0	-3.7375	90	0	-3.5035	90	0	-3.7368
16×8	162	0	-3.7844	306	0	-3.7310	306	0	-3.7840
32×16	578	0	-3.7961	1122	0	-3.7837	1122	0	-3.7960

FIGURE 3.5: Shape of the warped cross-section of the left-hand end at the beam according to the theory of elasticity, the multi-layer beam model and the 2D plane-stress finite-element models for different meshes and $\nu = 0$

TABLE 3.5: Displacements at the left-hand end of the beam for the multilayer beam model and 2D plane-stress finite-element models for $\nu = 0.25$ (analytical solution: $u = \pm 0.05625$, $v = -0.075$)

Mesh	Multi-layer beam			2D displacement-based elements			2D enhanced-strain elements		
$n \times N$	D.O.F.	$u(0, \pm\frac{h}{2})$	$v(0, \pm\frac{h}{2})$	D.O.F.	$u(0, \pm\frac{h}{2})$	$v(0, \pm\frac{h}{2})$	D.O.F.	$u(0, \pm\frac{h}{2})$	$v(0, \pm\frac{h}{2})$
4×2	18	± 0.0469	0	30	±0.1080	-0.0438	30	±0.0392	-0.0630
8×4	50	± 0.0586	0	90	±0.0957	-0.0711	90	±0.0538	-0.0830
16×8	162	± 0.0615	0	306	±0.0731	-0.0837	306	±0.0552	-0.0901
32×16	578	± 0.0623	0	1122	±0.0614	-0.0899	1122	±0.0550	-0.0926

The same comparison is also given for a more realistic value of the Poisson's ratio of $\nu = 0.25$. The displacements at the left-hand end cross-section and the free-end displacements at the beam's axis are given in Tables 3.5 and 3.6. The corresponding values according to the theory of elasticity are $u(0, \pm\frac{h}{2}) = \pm 0.05625$, $v(0, \pm\frac{h}{2}) = -0.075$, $u(L, 0) = 0$ and $v(L, 0) = -3.95$. In this example the multi-layer beam gives even better results at the free-end, but at the left-hand end it cannot return the non-zero vertical displacements because in the beam theory the transverse strains are not considered. The 2D plane-stress finite-element models give a rather good approximation of the horizontal displacements at the left-hand end cross-section, while the vertical displacements do not converge to the analytical solution.

An additional comparison between the multi-layer beam and the 2D plane-stress finite elements is given for the case of a fully clamped thick beam (see Fig. 3.4). The left-hand end cross-section is fully clamped ($u(0, y) = v(0, y) = 0$) and the force is applied exactly on the beam's centroidal axis. Since the solution of this

TABLE 3.6: Displacements at the free end of the beam's axis for the multilayer beam model and 2D plane-stress finite-element models for $\nu = 0.25$ (analytical solution: $u = 0$, $v = -3.95$)

Mesh	Multi-layer beam			2D displacement-based elements			2D enhanced-strain elements		
$n \times N$	D.O.F.	$u(L,0)$	$v(L,0)$	D.O.F.	$u(L,0)$	$v(L,0)$	D.O.F.	$u(L,0)$	$v(L,0)$
4×2	18	0	-3.6875	30	0	-2.8961	30	0	-3.4673
8×4	50	0	-3.8844	90	0	-3.5244	90	0	-3.6842
16×8	162	0	-3.9336	306	0	-3.6984	306	0	-3.7342
32×16	578	0	-3.9459	1122	0	-3.7383	1122	0	-3.7461

problem according to the theory of elasticity does not exist (see [5]), the 2D plane-stress finite-element solution using enhanced-strain elements with a fine (400×200) mesh is taken as a reference result. The reference displacements of the beam's axis at the free end for $\nu = 0$ and $\nu = 0.25$ read $v(L,0) = -3.9447$ and $v(L,0) = -3.8039$, respectively, while $u(L,0) = 0$ in both cases. The values of the vertical displacements of the beam's axis of the free end of the beam are given in Table 3.7 for the multi-layer beam model and the 2D plane-stress finite-element models using the displacement-based and enhanced-strain formulations for $\nu = 0$ and $\nu = 0.25$. The horizontal displacements of the beam's axis for the multi-layer beam model as well as for the 2D plane-stress finite-element models are zero. Figure 3.6 shows the deformed cross-section at the free end for $\nu = 0.25$ for the multilayer beam model and two-dimensional finite-element models. It is noticed that the multi-layer beam model presents a better approximation of the reference solution for rough meshes in comparison with the 2D plane-stress finite-element models, with considerably smaller number of degrees of freedom. For finer meshes, it is obvious that the multi-layer beam model expectedly converges to a different solution than the two-dimensional finite-element solutions.

TABLE 3.7: Vertical displacements at the free end of the beam's axis for the multilayer beam model and two-dimensional finite-element models (reference solution: $v = -3.9447$ for $\nu = 0$, $v = -3.8039$ for $\nu = 0.25$)

Mesh	Multi-layer beam			2D displacement-based elements			2D enhanced-strain elements		
$n \times N$	D.O.F.	$\nu = 0$	$\nu = 0.25$	D.O.F.	$\nu = 0$	$\nu = 0.25$	D.O.F.	$\nu = 0$	$\nu = 0.25$
4×2	18	-3.4532	-3.5658	30	-2.4414	-2.5104	30	-3.4723	-3.2711
8×4	50	-3.6195	-3.7362	90	-3.2923	-3.2242	90	-3.6587	-3.4925
16×8	162	-3.6616	-3.7795	306	-3.6293	-3.5076	306	-3.7323	-3.5872
32×16	578	-3.6722	-3.7904	1122	-3.7545	-3.6200	1122	-3.7823	-3.6450

For the same example, a comparison between the results obtained using the reduced and the full numerical integration is shown n Table 3.8. For the reduced integration $N - 1$ and for the full integration N integration points are used (where
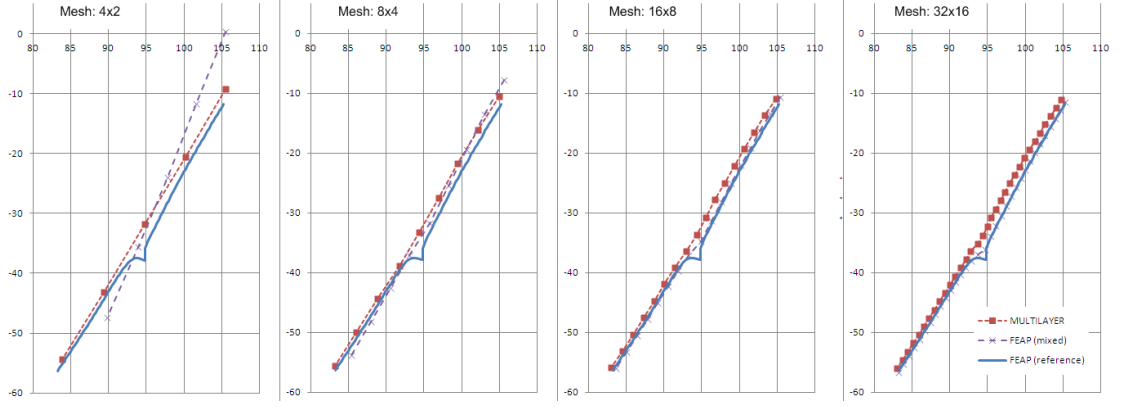
FIGURE 3.6: A comparison between the deformed cross-section of the free end of the beam according to the theory of elasticity and the multi-layer beam model and the 2D plane-stress finite-element models for different meshes and $\nu = 0.25$

N is the number of interpolation nodes). Using full integration usually causes the so-called shear locking, which is more pronounced in case of very thin beams. Since in this example the beam is thick ($L/h = 2$), the results obtained using the full integration are still worse than using the reduced integration (especially for the most coarse meshes), although the "locking" (very small displacements) does not occur. The shear locking problem can be avoided by using the linked interpolation for the unknown functions with the full integration. Papa and Jelenić [41] have derived the linked interpolation for an arbitrary number of nodes. According to [41], the interpolation functions for the displacements of a two noded plane beam element can be derived as

$$\boldsymbol{u}(X_1) = \begin{Bmatrix} u(X_1) \\ v(X_1) \end{Bmatrix} = \frac{L - X_1}{L} \begin{Bmatrix} u_1 \\ v_1 \end{Bmatrix} + \frac{X_1}{L} \begin{bmatrix} u_2 \\ v_2 \end{bmatrix} - \frac{X_1(L - X_1)}{2L} \begin{Bmatrix} 0 \\ \theta_2 - \theta_1 \end{Bmatrix}$$
(3.61)

where u_1, v_1, θ_1 and u_2, v_2, θ_2 denote the displacements and the cross-sectional rotation at the first and the second node, respectively. The cross-sectional rotations are interpolated using the Lagrangian interpolation. In the case of a multi-layer beam with a rigid interconnection, the displacements of the main layer α are interpolated using the nodal cross-sectional rotations $\theta_{\alpha,1}$ and $\theta_{\alpha,2}$, which can be written as

$$\boldsymbol{u}_{(\alpha)} = I_1(X_1)\boldsymbol{u}_{\alpha,1} + I_2(X_1)\boldsymbol{u}_{\alpha,2} + I_3(X_1)\delta\boldsymbol{\theta}_\alpha,$$
(3.62)

where

$$I_1(X_1) = \frac{L-X_1}{L}, \quad I_2(X_1) = \frac{X_1}{L}, \quad I_3(X_1) = \frac{X_1(L-X_1)}{2L}, \quad \delta\boldsymbol{\theta}_\alpha = \left\{ \begin{array}{c} 0 \\ \theta_{\alpha,1} - \theta_{\alpha,2} \end{array} \right\}.$$
(3.63)

Table 3.8 shows that, in comparison with the Lagrangian interpolation, the linked interpolation for the full integration gives significantly better results, although they are still worse than the results obtained using the reduced integration. The same phenomenon was also observed in non-linear analysis of homogeneous beams [42]

TABLE 3.8: Vertical displacent at the free end of a cantilever beam, $v(L)$, obtained using the Lagrangian and the linked interpolation for reduced and full integration ($\nu = 0$).

	Lagrangian interpolation		Linked interpolation	
Mesh	Red. int.	Full int.	Red. int.	Full int.
4×2	-3.4532	-2.4209	-3.4532	-3.4446
8×4	-3.6195	-3.2526	-3.6195	-3.6154
16×8	-3.6616	-3.5595	-3.6616	-3.6602
32×16	-3.6722	-3.6459	-3.6722	-3.6717

3.5.2.2 Thick cantilever beam - Non-linear analysis

In this section we investigate the behaviour of the thick cantilever beam from Fig. 3.4 under a load causing large displacements and rotations ($F = 1$). The left-hand end cross-section is fully clamped ($u(0, y) = v(0, y) = 0$) and the force is applied exactly on the beam's axis. Since the theory of elasticity gives a solution only in case of small deformations and rotations, for non-linear analysis a fine ($n \times N = 400 \times 200$) two-dimensional finite-element mesh is used as a reference. Solid two-dimensional element based on the mixed three-field displacement–pressure–volume ($\boldsymbol{u} - p - \theta$) formulation [60, 79] from the FEAP element library is used to solve the problem with large deformations. A comparison between the multi-layer beam solution and the solution for the 2D plane-stress finite element is shown in Table 3.9 for the free end displacements at the beam's axis with $\nu = 0$. The reference results read $u(L, 0) = -5.1629$ and $v(L, 0) = -37.894$. In Fig. 3.7 are shown the shapes of the cross-sections for the compared models. The local deformation

around the point of the load application $(L, 0)$ is in this example quite pronounced. It is noticed that for coarse meshes the multi-layer beam solution gives a better approximation of the reference solution, while for the finer meshes it expectedly converges to the values different from those proposed by the 2D plane-stress finite-element solution. Again, the number of degrees of freedom for the multi-layer beam is considerably smaller than for the 2D plane-stress finite-element mesh.

TABLE 3.9: Displacements at the free end of the beam for the multilayer beam model and 2D plane-stress finite-element model for $\nu = 0$ (reference solution: $u = -5.1629$, $v = -37.894$)

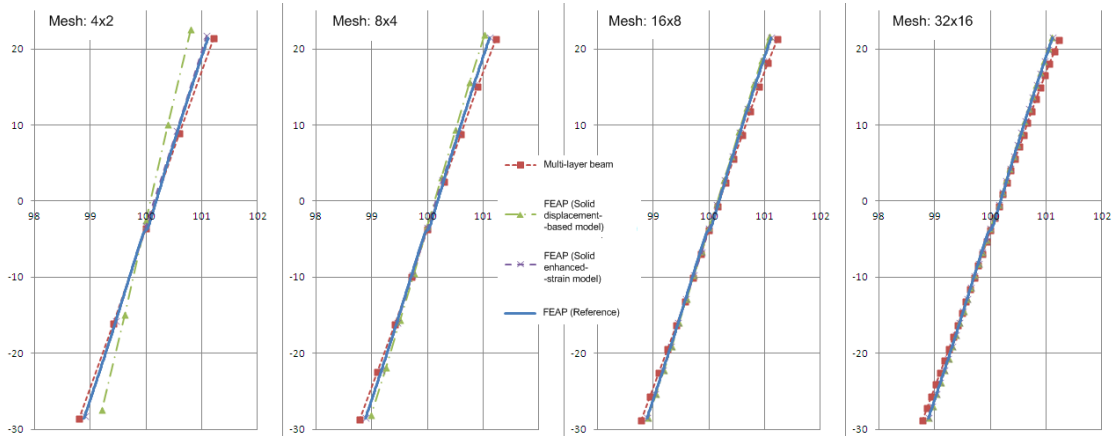| Mesh	Multi-layer beam			2D mixed $\boldsymbol{u} - p - \theta$ element		
$n \times N$	D.O.F.	$u(L,0)$	$v(L,0)$	D.O.F.	$u(L,0)$	$v(L,0)$
4×2	18	-5.1656	-31.8751	30	-2.1812	-23.995
8×4	50	-5.6118	-33.1968	90	-4.2232	-31.696
16×8	162	-5.6546	-33.5993	306	-5.0835	-34.761
32×16	578	-5.6084	-33.7709	1122	-5.3001	-36.091

FIGURE 3.7: A comparison between the deformed cross-section of the free end of the beam according to the the multi-layer beam model and the two-dimensional finite-element model for different meshes

If we introduce the Poisson's ratio $\nu = 0.25$, we obtain the results presented in Table 3.10. The reference results, obtained with the 2D plane-stress finite element based on the mixed $\boldsymbol{u} - p - \theta$ formulation for the large deformations and mesh $n \times N = 80 \times 40$ read $u(L,0) = -5.0326$ and $v(L,0) = -37.202$. The multi-layer beam formulation with relatively small number of degrees of freedom again proves to be a good approximation of the 2D plane-stress solution obtained with considerably more degrees of freedom.

The actual deformation of the cantilever for different meshes of the multi-layer beams is shown in Fig.3.8.

TABLE 3.10: Displacements at the right-hand end of the beam for the multilayer beam model and the 2D plane-stress finite-element models for $\nu = 0.25$ (reference solution: $u = -5.0326$, $v = -37.202$)

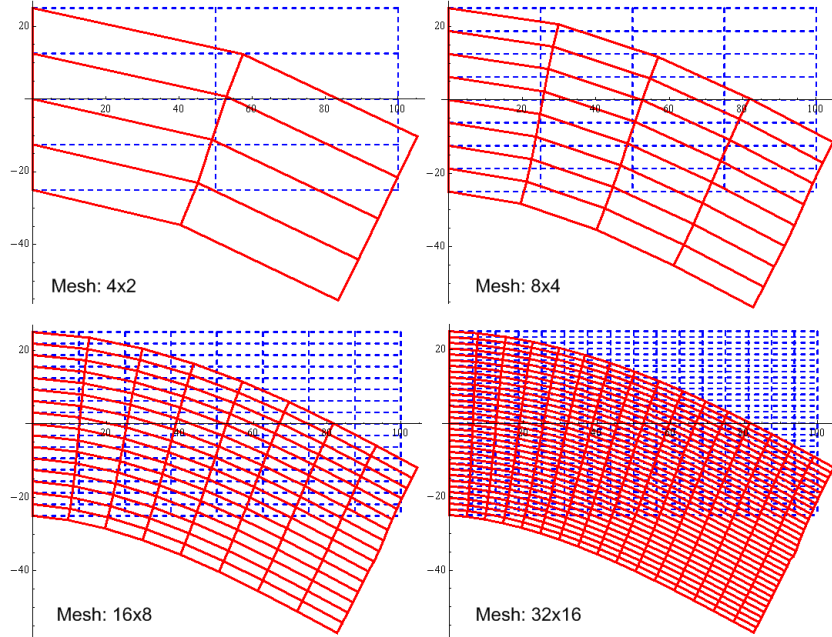| Mesh	Multi-layer beam			2D mixed $\boldsymbol{u} - p - \theta$ elements		
$n \times N$	D.O.F.	$u(L,0)$	$v(L,0)$	D.O.F.	$u(L,0)$	$v(L,0)$
4×2	18	-5.4475	-32.8602	30	-2.3515	-25.348
8×4	50	-5.8894	-34.2202	90	-4.0217	-31.63
16×8	162	-5.9232	-34.6380	306	-4.6672	-34.157
32×16	578	-5.8729	-34.8275	1122	-4.8179	-35.342

FIGURE 3.8: The deformed shape of the multi-layer beam model for different meshes and $\nu = 0.25$

3.6 Conclusions

A geometrically exact multi-layer beam finite element with rigid connection between the layers has been presented. Arbitrary position of the layers' and the composite beam's reference axes allows for arbitrary positioning of the applied loading. It have been shown that the kinematic constraint relating the displacement vector of an arbitrary layer and the displacement vector of the beam reference line may be written in a unique way regardless of the positions of the layer and the beam reference axes. This expression, in which the rotations of all the layers between the two reference lines also take place, makes it very easy to assemble the composite beam element from the original Reissner's beam theory using the principle of virtual work and perform the linearization needed for the Newton-Raphson

solution procedure.

The element has been verified against the results in [75, 76] and its capabilities tested on a thick beam example against analytical and numerical results coming from 2D elasticity. While the beam theory utilised obviously cannot recognise the existence of the transverse normal stresses and strains, it shows remarkable ability to capture the cross-sectional warping effect and give good approximation of 2D elasticity results using far less degrees of freedom.

4 NON-LINEAR ANALYSIS OF MULTI-LAYER BEAMS WITH COMPLIANT INTERCONNECTIONS

4.1 Introduction

In this section, a model for multi-layer beams with interconnection allowing for delamination between the layers is presented. Bulk material is modelled using beam finite elements, while the cohesive zone model embedded into interface elements [2], which allows single- and mixed-mode delamination, is used for the interconnection. The number of layers and interconnections is arbitrary, where each layer and interconnection can have different material and geometrical properties. A linear-elastic constitutive law is used for the bulk material and the geometrically exact Reissner's kinematic equations are linearised (small displacements and rotations) reducing to the Timoshenko's beam theory equations for each layer. Since the the constitutive law for the interconnection is non-linear, the problem is solved numerically using the Newton-Raphson solution procedure with the modified arc-length method. After the problem description, the governing equations are derived, the solution procedure is explained in detail and the results from the numerical examples are compared to the results from the literature , where 2D plane-stress elements for the bulk material are used.

4.2   Problem description

4.2.1   Position of a layer of the composite beam in the material co-ordinate system

An initially straight multi-layer beam of length L in which the layers are allowed to move with respect to one another depending on the properties of the interconnection is considered. The beam is composed of n layers and $n-1$ interconnections. An arbitrary layer is denoted as i, while an arbitrary interconnection, placed between layers i and $i+1$, is denoted as α (see Fig. 4.1).
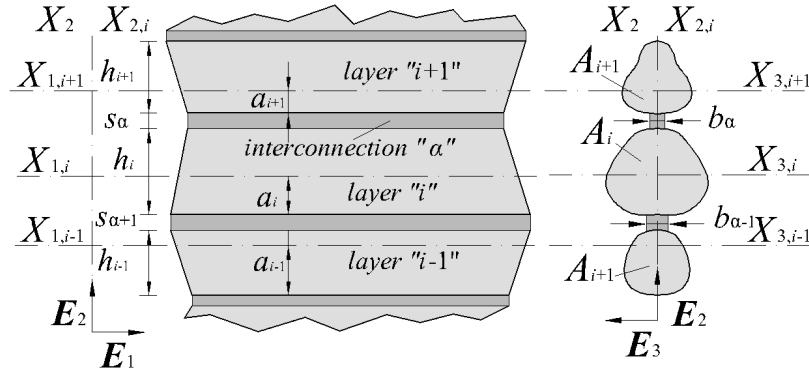

FIGURE 4.1: Position of a segment of a multi-layer beam with interface in the material co-ordinate system

Position of the layers with respect to the axes X_1, X_2 and X_3 is explained in detail in section 3.2.1 according to Fig. 4.1. Definition of geometrical and material properties of layers is also already explained in section 3.2.1. The height and the width of an interconnection are denoted as s_α and b_α, respectively. Thus, it is assumed that the interconnections have rectangular cross-sections, while the layer's cross-sections are arbitrary, but with a common principal axis X_2.

4.2.2   Position of a layer of the composite beam in the spatial co-ordinate system

According to Fig. 3.2 from section 3.2.2, the reference axes of all layers in the initial undeformed state are defined by the unit vector $\boldsymbol{t}_{01}$ which closes an angle ψ with respect to the axis defined by the base vector $\boldsymbol{e}_1$ of the spatial co-ordinate

system. Definition of the base vectors $\boldsymbol{t}_{0j}$, $\boldsymbol{t}_{i,j}$, and transformation matrices $\boldsymbol{\Lambda}_0$ and $\boldsymbol{\Lambda}_i$, where i denotes the layer and $j = 1, 2$, is given in expressions 3.3 and 3.4 from section 3.2.2. For the geometrically linear case ($\sin\theta_i \approx \theta_i$ and $\cos\theta_i \approx 1$) $\boldsymbol{\Lambda}_i$ becomes

$$\boldsymbol{\Lambda}_i = \begin{bmatrix} 1 & -\theta_i \\ \theta_i & 1 \end{bmatrix} \boldsymbol{\Lambda}_0. \tag{4.1}$$

Finally, the vector of displacement of the layer's reference axis, $\boldsymbol{u}_i(X_1)$, is defined as (3.6) according to Fig. 3.2.

4.3 Governing equations

Governing equations of the model consist of:

1. **Assembly equations**, which define how the layers and the interconnections are assembled into a multi-layer beam,

2. **Governing equations for the layers**, where kinematic, constitutive and equilibrium relations for the layers are defined and

3. **Governing equations for the interconnection**, where kinematic, constitutive and equilibrium relations for the interconnection are defined.

The derivation of the governing equations is explained in detail in the following sections.

4.3.1 Assembly equations

Undeformed and deformed state of a segment of the multi-layer beam is shown in Fig. 4.2.

The following relationships between the displacements of the layers can be deduced from Fig. 4.2:

$$\boldsymbol{u}_{T,\alpha} = \boldsymbol{u}_{i+1} + (\boldsymbol{t}_{02} - \boldsymbol{t}_{i+1,2})a_{i+1}, \tag{4.2}$$

$$\boldsymbol{u}_{B,\alpha} = \boldsymbol{u}_i + (\boldsymbol{t}_{i,2} - \boldsymbol{t}_{02})(h_i - a_i), \tag{4.3}$$
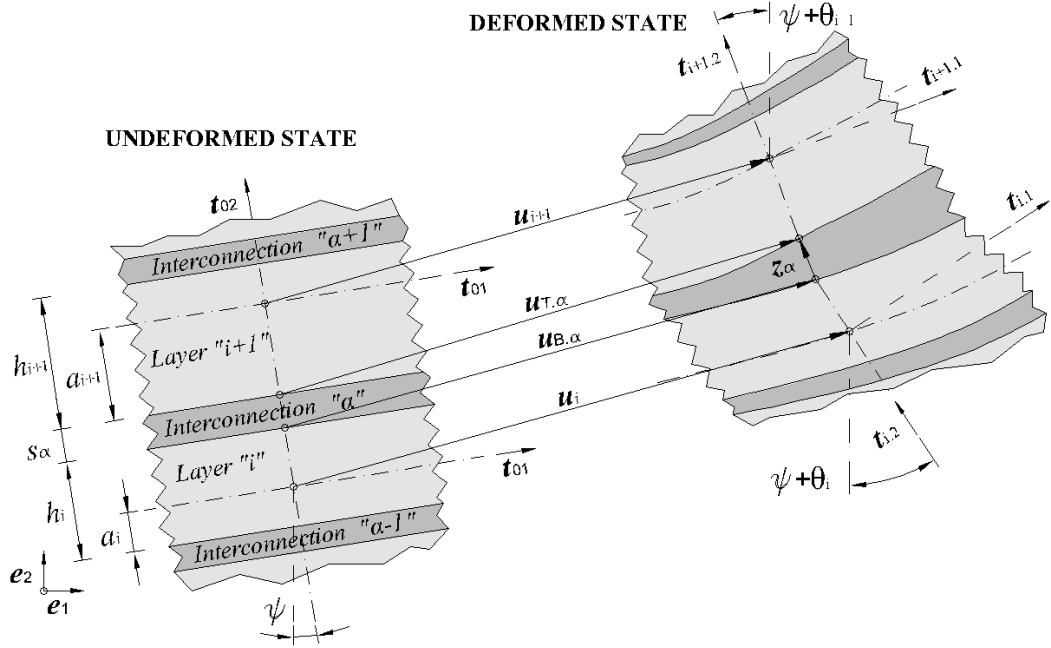
FIGURE 4.2: Undeformed and deformed state of a multi-layer beam with inter-connection segment

where $\boldsymbol{u}_i$ and $\boldsymbol{u}_{i+1}$ denote the displacements of the reference axes of the layers lying above and below the interconnection α, while $\boldsymbol{u}_{T,\alpha}$ and $\boldsymbol{u}_{B,\alpha}$ denote the displacements of the top and the bottom of the interconnection α. According to Fig. 4.2, vector $\boldsymbol{z}_\alpha$ can be expressed using (4.2) and (4.3) as

$$\boldsymbol{z}_\alpha = s_\alpha \boldsymbol{t}_{02} + \boldsymbol{u}_{T,\alpha} - \boldsymbol{u}_{B,\alpha} =$$
$$= \boldsymbol{u}_{i+1} - \boldsymbol{u}_i + a_{i+1}(\boldsymbol{t}_{02} - \boldsymbol{t}_{i+1,2}) + (h_i - a_i)(\boldsymbol{t}_{02} - \boldsymbol{t}_{i,2}) + s_\alpha \boldsymbol{t}_{02}. \qquad (4.4)$$

4.3.2 Governing equations for layers

4.3.2.1 Kinematic equations

Non-linear kinematic equations according to Reissner's beam theory [48] are already presented in (3.14) and (3.15) from section 3.3.2. For the geometrically linear case ($\sin\theta_i \approx \theta_i$ and $\cos\theta_i \approx 1$) expression (3.14) reduces to

$$\boldsymbol{\gamma}_i = \boldsymbol{\Lambda}_0^\mathsf{T}(\boldsymbol{u}_i' - \theta_i \boldsymbol{t}_{02}), \qquad (4.5)$$

showing that, in this case, Reissner's beam theory coincides with Timoshenko's.

4.3.2.2 Constitutive equations

Constitutive law for the layers in linear elastic and it is, together with the definition of stress resultants and the constitutive matrix $\boldsymbol{C}_i$, already presented in section 3.3.3.

4.3.2.3 Equilibrium equations

Equilibrium equations are derived from the principle of virtual work as:

$$
V_i^L \equiv V_i^{int} - V_i^{ext} = \int_0^L \left(\overline{\boldsymbol{\gamma}}_i \cdot \boldsymbol{N}_i + \overline{\kappa}_i M_i \right) \mathrm{d}X_1 - \int_0^L \left(\overline{\boldsymbol{u}}_i \cdot \boldsymbol{f}_i + \overline{\theta}_i w_i \right) \mathrm{d}X_1 -
$$
$$
- \overline{\boldsymbol{u}}_i(0) \cdot \boldsymbol{F}_{i,0} - \overline{\theta}_i(0) W_{i,0} - \overline{\boldsymbol{u}}_i(L) \cdot \boldsymbol{F}_{i,L} - \overline{\theta}_i(L) W_{i,L}, \tag{4.6}
$$

where V_i^L is the virtual work of the layer i composed of the virtual work of internal forces V_i^{int} and the virtual work of external forces V_i^{ext} on layer i. $\overline{\boldsymbol{\gamma}}_i$ and $\overline{\kappa}_i$ denote the virtual strains, while $\overline{\boldsymbol{u}}_i$ and $\overline{\theta}_i$ denote the virtual displacements and rotations, which are functions of X_1. The distributed external loads over the beam's length are denoted as $\boldsymbol{f}_i$ and w_i, while the loads concentrated on the beam ends by $\boldsymbol{F}_{i,j}$ and $W_{i,j}$, $j = 0, L$. According to expressions (4.5) and (3.15) for a geometrically linear problem, the virtual strains become

$$
\left\{ \begin{matrix} \overline{\boldsymbol{\gamma}}_i \\ \overline{\kappa}_i \end{matrix} \right\} = \begin{bmatrix} \boldsymbol{\Lambda}_0^\mathsf{T} & \boldsymbol{0} \\ \boldsymbol{0}^\mathsf{T} & 1 \end{bmatrix} \left(\begin{bmatrix} \frac{\mathrm{d}}{\mathrm{d}X_1} \boldsymbol{I} & -\boldsymbol{t}_{02} \\ \boldsymbol{0}^\mathsf{T} & \frac{\mathrm{d}}{\mathrm{d}X_1} \end{bmatrix} \left\{ \begin{matrix} \overline{\boldsymbol{u}}_i \\ \overline{\theta}_i \end{matrix} \right\} \right) = \boldsymbol{L}(\boldsymbol{D}\overline{\boldsymbol{p}}_i), \tag{4.7}
$$

and expression (4.6) can be written as

$$
V_i^L = \int_0^L \left[(\boldsymbol{D}\overline{\boldsymbol{p}}_i)^\mathsf{T} \boldsymbol{L}^\mathsf{T} \left\{ \begin{matrix} \boldsymbol{N}_i \\ M_i \end{matrix} \right\} - \overline{\boldsymbol{p}}_i^\mathsf{T} \left\{ \begin{matrix} \boldsymbol{f}_i \\ w_i \end{matrix} \right\} \right] \mathrm{d}X_1 - \overline{\boldsymbol{p}}_i^\mathsf{T}(0) \left\{ \begin{matrix} \boldsymbol{F}_{i,0} \\ W_{i,0} \end{matrix} \right\} - \overline{\boldsymbol{p}}_i^\mathsf{T}(L) \left\{ \begin{matrix} \boldsymbol{F}_{i,L} \\ W_{i,L} \end{matrix} \right\}.
$$
$$
\tag{4.8}
$$

The resulting expression is non-linear in terms of the basic unknown functions ($\boldsymbol{u}_i$ and θ_i) and cannot be solved in a closed form. Thus, the shape of virtual (test) functions ($\overline{\boldsymbol{u}}_i$ and $\overline{\theta}_i$)is chosen in advance assuming that for a finite number of nodes N the virtual displacements and rotations are known at the nodes ($\overline{\boldsymbol{u}}_{i,j}$ and

$\overline{\theta}_{i,j}, j \in \{1, N\}$) and interpolated between them as

$$\overline{\boldsymbol{p}}_i \doteq \sum_{j=1}^{N} \boldsymbol{\Psi}_j(X_1) \begin{Bmatrix} \overline{\boldsymbol{u}}_{i,j} \\ \overline{\theta}_{i,j} \end{Bmatrix} = \sum_{j=1}^{N} \boldsymbol{\Psi}_j(X_1) \overline{\boldsymbol{p}}_{i,j}, \qquad (4.9)$$

where $\boldsymbol{\Psi}_j$ is the matrix of interpolation functions of dimensions 3×3. Further,

$$\overline{\boldsymbol{p}}_i = \begin{bmatrix} \delta_{i1}\boldsymbol{I} & \delta_{i2}\boldsymbol{I} & \dots & \delta_{in}\boldsymbol{I} \end{bmatrix} \begin{Bmatrix} \overline{\boldsymbol{p}}_1 \\ \overline{\boldsymbol{p}}_2 \\ \vdots \\ \overline{\boldsymbol{p}}_n \end{Bmatrix} \doteq \begin{bmatrix} \delta_{i1}\boldsymbol{I} & \delta_{i2}\boldsymbol{I} & \dots & \delta_{in}\boldsymbol{I} \end{bmatrix} \sum_{j=1}^{N} \boldsymbol{\Psi}_j \begin{Bmatrix} \overline{\boldsymbol{p}}_{1,j} \\ \overline{\boldsymbol{p}}_{2,j} \\ \vdots \\ \overline{\boldsymbol{p}}_{n,j} \end{Bmatrix} =$$

$$= \sum_{j=1}^{N} \begin{bmatrix} \delta_{i1}\boldsymbol{\Psi}_j & \delta_{i2}\boldsymbol{\Psi}_j & \dots & \delta_{in}\boldsymbol{\Psi}_j \end{bmatrix} \overline{\boldsymbol{p}}_{G,j} = \sum_{j=1}^{N} \boldsymbol{P}_{i,j} \overline{\boldsymbol{p}}_{G,j}, \qquad (4.10)$$

where $\overline{\boldsymbol{p}}_{G,j} = \langle \overline{\boldsymbol{p}}_{1,j} \quad \overline{\boldsymbol{p}}_{2,j} \quad \dots \overline{\boldsymbol{p}}_{n,j} \rangle^{\mathsf{T}}$ is the nodal global vector of virtual unknown functions and δ_{ij} is the Kronecker delta defined in (3.38). Now, expression (4.8) becomes

$$V_i^L = \sum_{j=1}^{N} \overline{\boldsymbol{p}}_{G,j}^{\mathsf{T}} \Bigg\{ \int_0^L \Bigg[(\boldsymbol{D}\boldsymbol{P}_{i,j})^{\mathsf{T}} \boldsymbol{L}^{\mathsf{T}} \begin{Bmatrix} \boldsymbol{N}_i \\ M_i \end{Bmatrix} - \begin{Bmatrix} \boldsymbol{f}_i \\ w_i \end{Bmatrix} \Bigg] \mathrm{d}X_1 -$$

$$- \boldsymbol{P}_{i,j}^{\mathsf{T}}(0) \begin{Bmatrix} \boldsymbol{F}_{i,0} \\ W_{i,0} \end{Bmatrix} - \boldsymbol{P}_{i,j}^{\mathsf{T}}(L) \begin{Bmatrix} \boldsymbol{F}_{i,L} \\ W_{i,L} \end{Bmatrix} \Bigg\} = \sum_{j=1}^{N} \overline{\boldsymbol{p}}_{G,j}^{\mathsf{T}} \boldsymbol{g}_{i,j}^L, \qquad (4.11)$$

where $\boldsymbol{g}_{i,j}^L$ it the nodal vector of residual forces for the layer i which will be later introduced to the global equilibrium equation of the multi-layer beam with interconnection.

4.3.3 Governing equations for the interconnection

Interface finite elements by Alfano and Crisfield [2]with embedded cohesive zone model (CZM) are adopted in the present multi-layer beam model. The interface is a zero-thickness ($s_\alpha = 0$) layer with a non-linear constitutive law allowing for delamination in modes I and II including a mixed-mode delamination. Thus, depending on the conditions on the interface, the connection between layers can

be linear-elastic and after the softening of the interconnection material a complete damage may occur.

4.3.3.1 Kinematic equations

For a zero-thickness interconnection α, from Fig. 4.2, the vector of relative displacements between the upper and the lower edge of the interconnection follows as $\boldsymbol{z}_\alpha = \boldsymbol{u}_{T,\alpha} - \boldsymbol{u}_{B,\alpha}$, from where the vector of the local relative displacements is defined as

$$\boldsymbol{d}_\alpha = \begin{Bmatrix} d_{1,\alpha} \\ d_{2,\alpha} \end{Bmatrix} = \boldsymbol{\Lambda}_\alpha \boldsymbol{z}_\alpha = \boldsymbol{\Lambda}_\alpha (\boldsymbol{u}_{T,\alpha} - \boldsymbol{u}_{B,\alpha}), \qquad (4.12)$$

where $d_{1,\alpha}$ and $d_{2,\alpha}$ are relative displacements of the interconnection in tangential and normal direction, respectively, while $\boldsymbol{\Lambda}_\alpha$ is an orientation that has to be defined based on the orientations $\boldsymbol{\Lambda}_i$ and $\boldsymbol{\Lambda}_{i+1}$. In a geometrically linear setting $\boldsymbol{\Lambda}_\alpha = \boldsymbol{\Lambda}_0$ and $\boldsymbol{d}_\alpha = \boldsymbol{\Lambda}_0 (\boldsymbol{u}_{T,\alpha} - \boldsymbol{u}_{B,\alpha})$.

4.3.3.2 Constitutive equations

For the interconnection, a constitutive law allowing for delamination is adopted. In general, any deformation of the crack surfaces can be viewed as a superposition of three basic delamination modes [8], which are defined as follows:

1. **Opening mode, I**. The crack surfaces separate perpendicularly to the plane of delamination (direction X_2),

2. **Sliding mode, II**. The crack surfaces slide relatively to each other in the longitudinal direction (along the axis X_1),

3. **Tearing mode, III**. The crack surfaces slide relatively to each other in the transverse direction (along the axis X_3).

Obviously, in case of a planar delamination problem, only the first two delamination modes are considered. A cohesive-zone model (CZM), embedded in the interface finite elements by Alfano and Crisfield [2], is used in the present work and shown in Fig. 4.3 for an arbitrary interconnection α. The CZM approach assumes

that a cohesive damage zone develops near the crack tip. The bilinear diagram represents an approximation of the real physical behaviour, where the crack is not completely brittle, but the cohesive tractions $\omega_{i,\alpha}$ $(i = 1, 2)$ first increase from zero to a failure point that is represented by the cohesive strength $\omega_{01,\alpha}$, at which they reach a maximum before they gradually decrease back to zero following the post peak softening behaviour, which results in complete separation (see Fig. 4.3). According to (4.12), index 1 is associated with tangential delamination (mode II) index 1, while for normal delamination (mode I) index 2 is used. For mode II delamination (see Fig. 4.3.a) the constitutive law is assumed as same independent of the direction of the delamination, while for mode I, delamination can occur only in case of tension (see Fig. 4.3 b). In case of compression, no penetration physically exists, which means that the corresponding stiffness is infinite. However, in the present model this stiffness is taken as equal to the one taken in tension. The latter is needed to monitor the stress in the direction orthogonal to the axis X_1 and, when they exceed the mode I strength, to utilise the damage law given in Fig. 4.3 b. Obviously, this stiffness must be high enough to prevent interpenetration of the crack faces. However, an overly high value can lead to numerical problems. Several guidelines have been proposed for obtaining the penalty stiffness of a cohesive element (see e.g. [68]). The energy release rate criterion of linear elastic fracture mechanics (LEFM) for crack propagation [8] is indirectly used by equating the areas under the traction-relative displacement diagram to the critical energy release rates $G_{c1,\alpha}$ and $G_{c2,\alpha}$ (see Fig. 4.3) as

$$G_{ci,\alpha} = \frac{1}{2}\omega_{0i,\alpha}d_{ci,\alpha}, \tag{4.13}$$

where $i = 1, 2$ and α denotes an interconnection in case of multiple interconnections.

The current state of delamination is expressed using a parameter which combines delamination in both modes as

$$\beta_\alpha(\tau') = \left[\left(\frac{|d_{1,\alpha}(\tau')|}{d_{01,\alpha}}\right)^\eta + \left(\frac{\langle d_{2,\alpha}(\tau')\rangle}{d_{02,\alpha}}\right)^\eta\right]^{\frac{1}{\eta}} - 1, \tag{4.14}$$
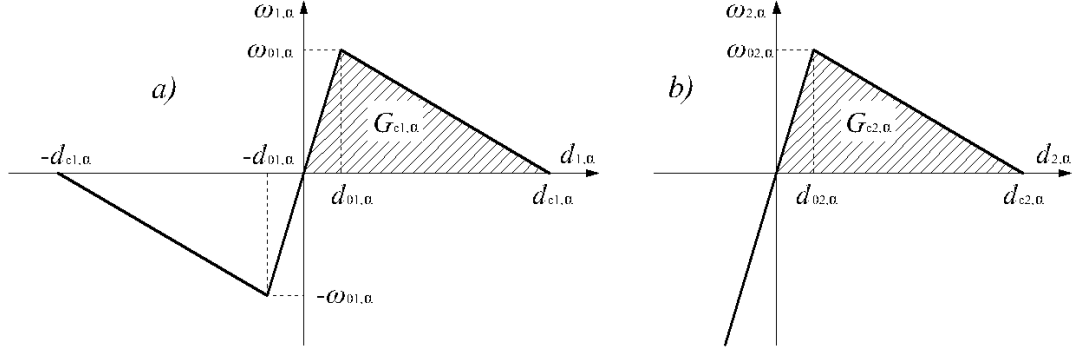
FIGURE 4.3: Constitutive law for the interconnection: a) mode II (direction 1)
i b) mode I (direction 2)

where in the present work $\eta = 2$ is used, τ' is the pseudo-time variable and $\langle \bullet \rangle$ is the McCauley bracket defined as

$$\langle x \rangle = \begin{cases} x & \text{if } x \geq 0, \\ 0 & \text{if } x < 0 \end{cases}. \tag{4.15}$$

Expression (4.14) determines the current state of delamination for single-mode ($d_{1,\alpha}$ or $d_{2,\alpha}$ equals zero) as well as for the coupled, mixed-mode delamination, where the overall damage at the interconnection is affected by both modes. This means that an interface element which is completely damaged in one mode has no bearing capacity in the other mode either. Damage of the interconnection is irreversible, thus, for a pseudo-time parameter τ, the maximum rate of delamination in the pseudo-time history is expressed as

$$\overline{\beta}_\alpha(\tau) = \max_{0 \leq \tau' \leq \tau} \beta_\alpha(\tau'). \tag{4.16}$$

An example of the relative displacement history with the corresponding traction response is shown in Fig. 4.4. After reaching the value d^*, for decreasing values of $d_{i,\alpha}$ an elastic unloading occurs with a reduced stiffness represented by the secant from the current point on the softening branch to the origin. Such unloading is specific to damage models, and is notably different to the plasticity models, where an amount of deformation (the plastic deformation) also remains irreversible. After the critical value of the relative displacement has been reached, the traction vanishes as a consequence of the total damage of the interconnection.

The tractions at the interconnection $\boldsymbol{\omega}_\alpha = \langle \omega_{\alpha,1} \quad \omega_{\alpha,2} \rangle^\mathsf{T}$ are calculated according
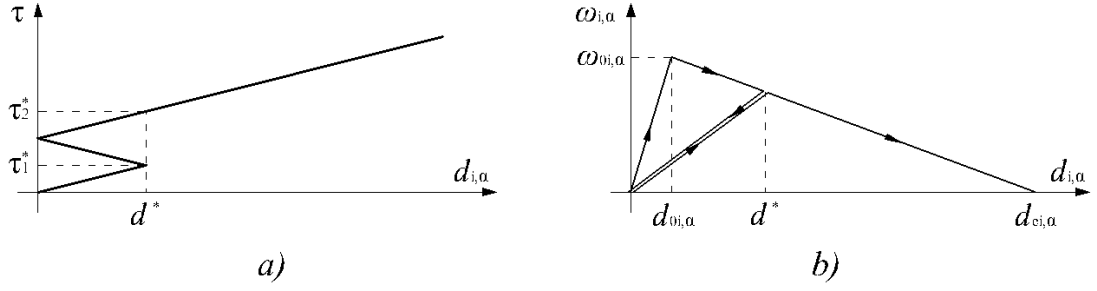
66

FIGURE 4.4: Relative displacement-pseudo time diagram (a) and the corresponding traction response (b)

to the following constitutive law:

$$
\boldsymbol{\omega}_\alpha = \begin{cases} \boldsymbol{S}_\alpha \boldsymbol{d}_\alpha & \text{if } \overline{\beta}_\alpha \leq 0, \\ \left[\boldsymbol{I} - \boldsymbol{G}_\alpha\right] \boldsymbol{S}_\alpha \boldsymbol{d}_\alpha & \text{if } \overline{\beta}_\alpha > 0, \end{cases} \tag{4.17}
$$

where

$$
\boldsymbol{S}_\alpha = \begin{bmatrix} S_{1,\alpha} & 0 \\ 0 & S_{2,\alpha} \end{bmatrix}, \quad S_{i,\alpha} = \frac{\omega_{0i,\alpha}}{d_{0i,\alpha}}, \quad \boldsymbol{G}_\alpha = \begin{bmatrix} g_{1,\alpha} & 0 \\ 0 & \langle \mathrm{sgn}(d_{2,\alpha}) \rangle g_{2,\alpha} \end{bmatrix},
$$

$$
g_{i,\alpha} = \min\left\{ 1, \frac{d_{ci,\alpha}}{d_{ci,\alpha} - d_{0i,\alpha}} \frac{\overline{\beta}_\alpha}{1 + \overline{\beta}_\alpha} \right\} \quad i = 1, 2. \tag{4.18}
$$

The case $\overline{\beta}_\alpha \leq 0$ corresponds to the linear-elastic behaviour of the interconnection, while $\overline{\beta}_\alpha > 0$ indicates the ongoing delamination and damage process at the interconnection. Parameter $g_{i,\alpha} \in \langle 0, 1]$ indicates the degree of the damage, where $g_{i,\alpha} = 1$ means that total damage of the interconnection has occurred and the connection between layers is completely lost (total delamination - $\boldsymbol{\omega}_\alpha = \boldsymbol{0}$). Matrix $\boldsymbol{S}_\alpha$ defines the interconnection stiffness for the linear elastic range for both directions, where parameter $S_{2,\alpha}$ represents the penalty stiffness parameter for mode I. Factor $\langle \mathrm{sgn}(d_{2,\alpha}) \rangle$ in the $\boldsymbol{G}_\alpha$ matrix assures that after the delamination has started ($\overline{\beta}_\alpha > 0$), the penetration between layers is partially prevented depending on the penalty stiffness parameter contained in matrix $\boldsymbol{S}_\alpha$ (see Fig. 4.3.b). The proposed constitutive law (4.17), for the case of single-mode delamination ($\omega_{1,\alpha} = 0$ or $\omega_{2,\alpha} = 0$) reduces to expressions which exactly describe the behaviour shown in Fig. 4.3.a) and 4.3.b) for modes II and I, respectively, with unloading as shown in Fig. 4.4.

4.3.3.3 Equilibrium equations

Equilibrium equations for the interconnection are again derived from the principle of virtual work as

$$V_\alpha^C = b_\alpha \int_0^L \overline{\boldsymbol{d}}_\alpha \cdot \boldsymbol{\omega}_\alpha \mathrm{d}X_1, \tag{4.19}$$

where V_α^C denotes the virtual work of internal forces of the interconnection α. According to (4.12), virtual relative displacements of the interconnection become

$$\overline{\boldsymbol{d}}_\alpha = \boldsymbol{\Lambda}_0 \left(\overline{\boldsymbol{u}}_{i+1} - \overline{\boldsymbol{u}}_i + \overline{\theta}_{i+1} a_{i+1} \boldsymbol{t}_{01} + \overline{\theta}_i (h_i - a_i) \boldsymbol{t}_{01} \right) = \boldsymbol{\Lambda}_0 \boldsymbol{B}_\alpha \overline{\boldsymbol{p}}_{C,\alpha} \tag{4.20}$$

where

$$\boldsymbol{B}_\alpha = \begin{bmatrix} -\boldsymbol{I} & \boldsymbol{t}_{01}(h_i - a_i) & \boldsymbol{I} & \boldsymbol{t}_{01} a_{i+1} \end{bmatrix}, \quad \overline{\boldsymbol{p}}_{C,\alpha} = \left\{ \begin{array}{c} \overline{\boldsymbol{p}}_i \\ \overline{\boldsymbol{p}}_{i+1} \end{array} \right\}, \quad i = \alpha. \tag{4.21}$$

Expression (4.19) can be now written as

$$V_\alpha^C = b_\alpha \int_0^L \overline{\boldsymbol{p}}_{C,\alpha}^\mathsf{T} \boldsymbol{B}_\alpha^\mathsf{T} \boldsymbol{\Lambda}_0^\mathsf{T} \boldsymbol{\omega}_\alpha \mathrm{d}X_1. \tag{4.22}$$

Since expression (4.22) is non-linear in terms of the basic unknown function, the virtual functions are interpolated and according to (4.10) the following expression is obtained

$$\overline{\boldsymbol{p}}_{C,\alpha} = \left\{ \begin{array}{c} \overline{\boldsymbol{p}}_i \\ \overline{\boldsymbol{p}}_{i+1} \end{array} \right\} \doteq \sum_{j=1}^N \begin{bmatrix} \boldsymbol{P}_{i,j} \\ \boldsymbol{P}_{i+1,j} \end{bmatrix} \overline{\boldsymbol{p}}_{G,j} = \sum_{j=1}^N \boldsymbol{R}_{\alpha,j} \overline{\boldsymbol{p}}_{G,j}, \tag{4.23}$$

which transforms expression (4.22) into

$$V_\alpha^C = \sum_{j=1}^N \overline{\boldsymbol{p}}_{G,j}^\mathsf{T} b_\alpha \int_0^L \boldsymbol{R}_{j,\alpha}^\mathsf{T} \boldsymbol{B}_\alpha^\mathsf{T} \boldsymbol{\Lambda}_0^\mathsf{T} \boldsymbol{\omega}_\alpha \mathrm{d}X_1 = \sum_{j=1}^N \overline{\boldsymbol{p}}_{G,j}^\mathsf{T} \boldsymbol{g}_{\alpha,j}^C, \tag{4.24}$$

where $\boldsymbol{g}_{\alpha,j}^C$ is the nodal vector of residual forces for the interconnection α which will be later introduced to the global equilibrium equation of the multi-layer beam with interconnection.

4.4   Solution procedure

To solve the system of governing equations for the multi-layer beam with inter-connection the vector of residual forces and the tangent stiffness matrix have to be determined. The problem is then solved numerically which is explained in detail in the following sections.

4.4.1   Determination of the vector of residual forces and the tangent stiffness matrix

Total virtual work for the multi-layer beam analysed is composed by the virtual work of n layers (4.11) and the virtual work of $n-1$ interconnections (4.24) and it can be written as

$$V^{TOT} = \sum_{i=1}^{n} \left[V_i^L + (1-\delta_{in}) V_i^C \right] = \sum_{j=1}^{N} \overline{\boldsymbol{p}}_{G,j}^{\mathsf{T}} \sum_{i=1}^{n} \left[\boldsymbol{g}_{i,j}^L + (1-\delta_{in}) \boldsymbol{g}_{i,j}^C \right]. \tag{4.25}$$

Since the total virtual work for the multi-layer beam must equal zero ($V^{TOT} = 0$) and the choice of the test parameters $\overline{\boldsymbol{p}}_{G,j}$ is arbitrary it follows that

$$\boldsymbol{g}_j = \sum_{i=1}^{n} \left[\boldsymbol{g}_{i,j}^L + (1-\delta_{in}) \boldsymbol{g}_{i,j}^C \right] = \boldsymbol{0}, \tag{4.26}$$

where $\boldsymbol{g}_j$ is the nodal vector of residual forces for the multi-layer beam which is composed of the nodal vector of internal forces $\boldsymbol{q}_j^{int}$ and the nodal vector of external forces $\boldsymbol{q}_j^{ext}$ as

$$\boldsymbol{g}_j = \boldsymbol{q}_j^{int} - \boldsymbol{q}_j^{ext} = \boldsymbol{0} \tag{4.27}$$

where

$$\boldsymbol{q}_j^{int} = \sum_{i=1}^{n} \left(\int_0^L (\boldsymbol{D}\boldsymbol{P}_{i,j})^{\mathsf{T}} \boldsymbol{L}^{\mathsf{T}} \begin{Bmatrix} \boldsymbol{N}_i \\ M_i \end{Bmatrix} \mathrm{d}X_1 + (1-\delta_{in})b_i \int_0^L (\boldsymbol{\Lambda}_0 \boldsymbol{B}_i \boldsymbol{R}_{i,j})^{\mathsf{T}} \boldsymbol{\omega}_i \mathrm{d}X_1 \right),$$

$$\boldsymbol{q}_j^{ext} = \sum_{i=1}^{n} \left(\int_0^L \boldsymbol{P}_{i,j}^{\mathsf{T}} \begin{Bmatrix} \boldsymbol{f}_i \\ w_i \end{Bmatrix} \mathrm{d}X_1 + \boldsymbol{P}_{i,j}^{\mathsf{T}}(0) \begin{Bmatrix} \boldsymbol{F}_{i,0} \\ W_{i,0} \end{Bmatrix} + \boldsymbol{P}_{i,j}^{\mathsf{T}}(L) \begin{Bmatrix} \boldsymbol{F}_{i,L} \\ W_{i,L} \end{Bmatrix} \right). \tag{4.28}$$

Expression (4.27) represents the equilibrium equation for the multilayer beam at the node-level and is highly non-linear and not solvable analytically in terms of the basic unknown functions. Thus, in order to solve the problem numerically, the nodal vector of residual forces is expanded in Talyor's series up to a linear term as in (3.44), and since the unknown function are contained only in the nodal vector of internal forces

$$\Delta \boldsymbol{q}_j^{ext} = \boldsymbol{0} \text{ and } \Delta \boldsymbol{g}_j = \Delta \boldsymbol{q}_j^{int}. \tag{4.29}$$

The unknown functions are contained in $\boldsymbol{N}_i$ and M_i which are linearised as

$$\begin{Bmatrix} \Delta \boldsymbol{N}_i \\ \Delta M_i \end{Bmatrix} = \boldsymbol{C}_i \begin{Bmatrix} \Delta \boldsymbol{\gamma}_i \\ \Delta \kappa_i \end{Bmatrix} = \boldsymbol{C}_i \begin{Bmatrix} \boldsymbol{\Lambda}_0^{\mathsf{T}} \left(\Delta \boldsymbol{u}_i' - \Delta \theta_i \boldsymbol{t}_{02} \right) \\ \Delta \theta_i' \end{Bmatrix} = \boldsymbol{C}_i \boldsymbol{L} (\boldsymbol{D} \Delta \boldsymbol{p}_i), \tag{4.30}$$

where $\boldsymbol{L}$ and $\boldsymbol{D}$ are given in (4.7) and $\Delta \boldsymbol{p}_i = \langle \Delta \boldsymbol{u}_i \quad \Delta \theta_i \rangle^{\mathsf{T}}$, and in the vector of contact tractions $\boldsymbol{\omega}_i$ which is linearised as

$$\Delta \boldsymbol{\omega}_i = \begin{cases} \boldsymbol{S}_i \Delta \boldsymbol{d}_i & \text{if } \overline{\beta}_i \leq 0, \\ (\boldsymbol{I} - \boldsymbol{G}_i) \, \boldsymbol{S}_i \Delta \boldsymbol{d}_i & \text{if } \overline{\beta}_i > 0 \text{ and } \beta_i < \overline{\beta}_i, \\ (\boldsymbol{I} - \boldsymbol{G}_i) \, \boldsymbol{S}_i \Delta \boldsymbol{d}_i - \Delta \boldsymbol{G}_i \boldsymbol{S}_i \boldsymbol{d}_i & \text{if } \overline{\beta}_i > 0 \text{ and } \beta_i = \overline{\beta}_i. \end{cases} \tag{4.31}$$

Linearisation of the vector of the relative displacements at the interconnection $\boldsymbol{d}_i$ is obtained analogously as in (4.20) and (4.23), thus

$$\Delta \boldsymbol{d}_i = \boldsymbol{\Lambda}_0 \boldsymbol{B}_i \Delta \boldsymbol{p}_{C,i} = \boldsymbol{\Lambda}_0 \boldsymbol{B}_i \sum_{k=1}^{N} \boldsymbol{R}_{i,k} \Delta \boldsymbol{p}_{G,k}, \tag{4.32}$$

where $\Delta \boldsymbol{p}_{G,k} = \langle \Delta \boldsymbol{p}_{1,k} \quad \Delta \boldsymbol{p}_{2,k} \quad \dots \quad \Delta \boldsymbol{p}_{n,k} \rangle^{\mathsf{T}}$. To linearise $\boldsymbol{G}_i$ first the parameter $\overline{\beta}_i$ has to be linearised as

$$\Delta \overline{\beta}_i = \frac{1}{\eta} \left[\left(\frac{|d_{1,\alpha}|}{d_{01,\alpha}} \right)^{\eta} + \left(\frac{\langle d_{2,\alpha} \rangle}{d_{02,\alpha}} \right)^{\eta} \right]^{\frac{1}{\eta} - 1} \Delta \left[\left(\frac{|d_{1,\alpha}|}{d_{01,\alpha}} \right)^{\eta} + \left(\frac{\langle d_{2,\alpha} \rangle}{d_{02,\alpha}} \right)^{\eta} \right] =$$
$$= \left(\overline{\beta}_i + 1 \right)^{1 - \eta} \left(\frac{|d_{1,i}|^{\eta - 1}}{d_{01,i}^{\eta}} \Delta |d_{1,i}| + \frac{\langle d_{2,i} \rangle^{\eta - 1}}{d_{02,i}^{\eta}} \Delta \langle d_{1,i} \rangle \right) \tag{4.33}$$

which with

$$\Delta |d_{1,i}| = \frac{|d_{1,i}|}{d_{i,1}} \Delta d_{1,i} \text{ and } \Delta \langle d_{2,i} \rangle = \frac{\langle d_{2,i} \rangle}{d_{2,i}} \Delta d_{2,i} \tag{4.34}$$

finally gives

$$\Delta\overline{\beta}_i = \left(\overline{\beta}_i + 1\right)^{1-\eta} \boldsymbol{v}_i^\mathsf{T} \Delta\boldsymbol{d}_i \tag{4.35}$$

where

$$\boldsymbol{v}_i^\mathsf{T} = \left\langle \frac{1}{d_{1,i}}\left(\frac{|d_{1,i}|}{d_{01,i}}\right)^\eta \quad \frac{1}{d_{2,i}}\left(\frac{\langle d_{2,i}\rangle}{d_{02,i}}\right)^\eta \right\rangle \text{ and } \Delta\boldsymbol{d}_i = \begin{Bmatrix} \Delta d_{1,i} \\ \Delta d_{2,i} \end{Bmatrix}. \tag{4.36}$$

After that it can be easily shown that

$$\Delta\left(\frac{\overline{\beta}_i}{1+\overline{\beta}_i}\right) = \frac{\Delta\overline{\beta}_i}{(1+\overline{\beta}_i)^2} = \frac{1}{(1+\overline{\beta}_i)^{\eta+1}}\boldsymbol{v}_i^\mathsf{T}\Delta\boldsymbol{d}_i, \tag{4.37}$$

and

$$\Delta\boldsymbol{G}_i = \boldsymbol{J}_i\boldsymbol{v}_i^\mathsf{T}\Delta\boldsymbol{d}_i, \tag{4.38}$$

with

$$\boldsymbol{J}_i = \begin{bmatrix} \xi_{1,i} & 0 \\ 0 & \langle\mathrm{sgn}(d_{2,\alpha})\rangle\xi_{2,i} \end{bmatrix}, \ \xi_{j,i} = \frac{d_{cj,i}}{d_{cj,i}-d_{0j,i}}\frac{\mathrm{sgn}(1-g_{j,i})}{(1+\overline{\beta}_i)^{\eta+1}}, \ j=1,2. \tag{4.39}$$

Expression(4.31) can be now written as

$$\Delta\boldsymbol{\omega}_i = \boldsymbol{U}_i\Delta\boldsymbol{d}_i = \boldsymbol{U}_i\boldsymbol{\Lambda}_0\boldsymbol{B}_i\sum_{k=1}^{N}\boldsymbol{R}_{i,k}\Delta\boldsymbol{p}_{G,k}, \tag{4.40}$$

where

$$\boldsymbol{U}_i = \begin{cases} \boldsymbol{S}_i & \text{if } \overline{\beta}_i \leq 0, \\ (\boldsymbol{I}-\boldsymbol{G}_i)\,\boldsymbol{S}_i & \text{if } \overline{\beta}_i > 0 \text{ and } \boldsymbol{\beta}_i < \overline{\boldsymbol{\beta}}_i, \\ \left(\boldsymbol{I}-\boldsymbol{G}_i-\boldsymbol{J}_i\boldsymbol{d}_i\boldsymbol{v}^\mathsf{T}\right)\boldsymbol{S}_i & \text{if } \overline{\beta}_i > 0 \text{ and } \boldsymbol{\beta}_i = \overline{\boldsymbol{\beta}}_i. \end{cases} \tag{4.41}$$

Linearised nodal vector of residual forces finally becomes

$$\Delta\boldsymbol{g}_j = \sum_{k=1}^{N}\boldsymbol{K}_{j,k}\Delta\boldsymbol{p}_{G,k}, \tag{4.42}$$

where

$$\boldsymbol{K}_{j,k} = \sum_{i=1}^{n}\int_0^L \left[\boldsymbol{H}_{i,j}^\mathsf{T}\boldsymbol{C}_i\boldsymbol{H}_{i,k} + (1-\delta_{in})b_i\boldsymbol{\Omega}_{i,j}^\mathsf{T}\boldsymbol{U}_i\boldsymbol{\Omega}_{i,k}\right]\mathrm{d}X_1, \tag{4.43}$$

is nodal tangent stiffness matrix with $\boldsymbol{H}_{i,l} = \boldsymbol{L}\left(\boldsymbol{DP}_{i,l}\right)$ and $\boldsymbol{\Omega}_{i,l} = \boldsymbol{\Lambda}_0\boldsymbol{B}_i\boldsymbol{R}_{i,l}$. Equation (3.44) is solved for all nodes at the global level, thus global vector of

residual forces $\boldsymbol{g} = \{\boldsymbol{g}_j\}$ according to (4.27) and (4.28), global tangent stiffness matrix $\boldsymbol{K} = [\boldsymbol{K}_{j,k}]$ according to (4.43) and global vector of increments of the unknown functions $\Delta \boldsymbol{p} = \{\Delta \boldsymbol{p}_{G,k}\}$ are assembled using the standard finite-element assembly procedure [80] to solve the system (3.45). For integration in (4.28) and (4.43) Gauss quadrature with $N - 1$ integration points is used for the beam parts (layers) and Simpson's rule with $N + 1$ integration points is used for the interconnection parts. In reference [52] it has been shown that, for linear elements, the application of Gauss quadrature results in a coupling between the degrees of freedom of different node sets and then in a oscillation of the traction profile, for high values of the traction gradients, which is not recovered if a Newton-Cotes integration rule (like Simpson's rule) is used.

4.4.2 Solution algorithm

The algorithm presented has been implemented within the computer package *Wolfram Mathematica*. Since the governing equations of the problem are non-linear in terms of the basic unknown functions, the solution of the problem is obtained iteratively using the Newton-Raphson solution procedure. First, the input data, consisting of geometrical and material properties of layers and interconnection, mesh information (number of finite elements, number of nodes per element), loading and boundary conditions, is entered. The algorithm starts from the undeformed configuration of the system with an initial load applied and then calculates the displacements and rotations to define the deformed configuration of the system. The procedure is repeated iteratively until the equilibrium in the new configuration is obtained and $\Delta \boldsymbol{p} \approx \boldsymbol{0}$ and $\boldsymbol{g} \approx \boldsymbol{0}$, depending on the numerical tolerance chosen. After the Newton-Raphson procedure converges, a new step begins with a new load increment.

4.4.2.1 Numerical properties of the delamination model

For each element and each interconnection the relative displacements are calculated and then at each integration point of the interconnection the current stage of delamination is determined (linear-elastic behaviour, softening, unloading and

reloading with a reduced stiffness or total damage). In the case when total delamination at all integrations point within an element occurs, the adherence between the layers is lost not only at that integration point, but along the entire element in line with the basic properties of weak formulation. The total loss of adherence at an integration point will lead to very sharp snap-backs in the load-displacement diagram, which is a behaviour that cannot be captured neither with standard load- or displacement-control methods in the Newton-Rapshon solution procedure, nor with the standard arc-length procedure [13]. In the present work the modified arc-length method proposed by Hellweg and Crisfield [24] is used. The modified arc-length method is explained in detail in the next section. It has to be also emphasised that for each load step it is checked whether the current degree of delamination in the interconnection $\beta_\alpha(\tau')$ is at the maximum amount reached so far $\overline{\beta}_\alpha(\tau)$ and, depending on its value, the interconnection tractions $\boldsymbol{\omega}_\alpha$ (4.17) and the matrix $\boldsymbol{U}_\alpha$ (4.41) are obtained. Thus, the values $\overline{\beta}_\alpha(\tau)$ are saved at each load step to be compared with the values $\beta_\alpha(\tau')$ in the iterations of the next step. Vector $\boldsymbol{\omega}_\alpha$ and matrix $\boldsymbol{U}_\alpha$ are then used to calculate the vector of residual forces and the tangent stiffness matrix. As it can be seen in (4.43), the part of the tangent stiffness matrix which originates from the layers (beam-type formulation) is independent of the basic unknown functions and thus remains constant through all load steps and iterations, unlike the layers' part in the vector of residual forces in (4.28), which depends on the stress and stress-couple resultants.

4.4.2.2 Modified arc-length method

The main idea of the arc-length method is to use the arc of the curve in the load-displacement diagram in an $n_u - 1$ dimensional hyperspace (where n_u is the total number of unknown parameters) to solve the non-linear equations using the Newton-Raphson procedure. According to [13], the equilibrium equation at the global level can be written in the following form

$$\boldsymbol{g}(\boldsymbol{p}, \lambda) = \boldsymbol{q}^{int}(\boldsymbol{p}) - \lambda \boldsymbol{q}^{ext} = \boldsymbol{0}, \tag{4.44}$$

where $\boldsymbol{g}$, $\boldsymbol{q}^{int}$ and $\boldsymbol{q}^{ext}$ are the global (assembled) vectors of residual, internal and external forces, respectively, and $\boldsymbol{p} = \{\boldsymbol{p}_{G,j}\}$, $(j \in \{1, N\})$, is the global vector

of unknown parameters and λ is the load-scaling factor. The vector of external forces $\boldsymbol{q}^{ext}$ contains the initial loads on the system and remains constant during the entire iterational solution procedure. However, in each iteration external loading is adjusted using the load-scaling factor λ. Vector $\boldsymbol{g}$ can be expanded in Talyor's series up to a linear term about an existing ('old') configuration as

$$\boldsymbol{g}(\boldsymbol{p}, \lambda) = \boldsymbol{g}|_{\boldsymbol{p}_{old}} + \boldsymbol{K}|_{\boldsymbol{p}_{old}} \Delta \boldsymbol{p} - \boldsymbol{q}^{ext} \Delta \lambda = \boldsymbol{0}, \tag{4.45}$$

where $\boldsymbol{p}_{old}$ is the global vector of unknown functions corresponding to the 'old' (last known, not necessarily equilibrium) configuration. If $\Delta \boldsymbol{p}$ is written in the following form

$$\Delta \boldsymbol{p} = \Delta \boldsymbol{p}_I + \Delta \lambda \Delta \boldsymbol{p}_{II}, \tag{4.46}$$

expression (4.45) becomes

$$\boldsymbol{K}|_{\boldsymbol{p}_{old}} \Delta \boldsymbol{p}_I + \Delta \lambda \boldsymbol{K}|_{\boldsymbol{p}_{old}} \delta \boldsymbol{p}_{II} = -\boldsymbol{g}|_{\boldsymbol{p}_{old}} + \Delta \lambda \boldsymbol{q}^{ext}, \tag{4.47}$$

which can be split into

$$\Delta \boldsymbol{p}_I = - \left(\boldsymbol{K}|_{\boldsymbol{p}_{old}} \right)^{-1} \boldsymbol{g}|_{\boldsymbol{p}_{old}} \text{ and } \Delta \boldsymbol{p}_{II} = \left(\boldsymbol{K}|_{\boldsymbol{p}_{old}} \right)^{-1} \boldsymbol{q}^{ext}. \tag{4.48}$$

The cylindrical arc-length formulation, according to [13], is based on the following constraint

$$c = (\boldsymbol{p} - \boldsymbol{p}_0) \cdot (\boldsymbol{p} - \boldsymbol{p}_0), \tag{4.49}$$

where $\boldsymbol{p}_0$ is the global vector of unknown functions corresponding to the last converged equilibrium state. Expanding the expression (4.49) in Taylor's series and taking into account (4.46) gives

$$\chi_1 \Delta \lambda^2 + \chi_2 \Delta \lambda + \chi_3 = 0, \tag{4.50}$$

where

$$\chi_1 = \Delta\boldsymbol{p}_{II} \cdot \Delta\boldsymbol{p}_{II},$$

$$\chi_2 = 2\Delta\boldsymbol{p}_{II} \cdot (\boldsymbol{p} + \Delta\boldsymbol{p}_I - \boldsymbol{p}_0), \tag{4.51}$$

$$\chi_3 = (\boldsymbol{p} + \Delta\boldsymbol{p}_I - \boldsymbol{p}_0) \cdot (\boldsymbol{p} + \Delta\boldsymbol{p}_I - \boldsymbol{p}_0) - c^2.$$

Quadratic equation (4.50) in general gives two solutions and the choice of the correct solution from the two is an issue which will be explained in detail.

In the first iteration of each load step $\boldsymbol{p} = \boldsymbol{p}_0 = \boldsymbol{p}_{old}$, $\lambda = 0$ and $\boldsymbol{g}|_{\boldsymbol{p}_{old}} = \boldsymbol{0}$, but $\boldsymbol{K}|_{\boldsymbol{p}_{old}}$ and $\boldsymbol{q}^{ext}$ have non-zero values (like in every other iteration). Then, from (4.48) it follows that $\Delta\boldsymbol{p}_I = \boldsymbol{0}$ and $\Delta\boldsymbol{p}_{II} \neq \boldsymbol{0}$, from (4.51) it follows that $\chi_2 = 0$, $\chi_3 = -c^2$ and from (4.50), finally, it follows that

$$\Delta\lambda = \pm\frac{c}{\|\Delta\boldsymbol{p}_{II}\|}. \tag{4.52}$$

Choosing the sign of $\Delta\lambda$ for the next iteration in the first load step is done according to the intention of increasing or decreasing the initial load given in $\boldsymbol{q}^{ext}$. In the following load steps, when either load increase or decrease can occur, the positive sign in (4.52) is chosen if tangent stiffness matrix is positively definite, otherwise (in case of at least one negative eigenvalue in the tangent stiffness matrix) the negative sign is chosen. With the correct sign of $\Delta\lambda$, new values $\boldsymbol{p} = \boldsymbol{p}_{old} + \Delta\boldsymbol{p}$, where $\Delta\boldsymbol{p} = \Delta\boldsymbol{p}_I + \Delta\lambda\Delta\boldsymbol{p}_{II}$, are obtained for the next iteration.

In the following iterations $\boldsymbol{g}|_{\boldsymbol{p}_{old}}$, $\boldsymbol{K}|_{\boldsymbol{p}_{old}}$, and after that, $\Delta\boldsymbol{p}_I$ and $\boldsymbol{p}_{II}$ are evaluated (and in general all have non-zero values), which again leads to equation (4.50), but this time with $\chi_2 \neq 0$. This equation, in general, can have real or complex solutions. In the case of complex solutions the arc-length parameter c has to be reduced and the load step repeated. A case of a single real solution practically never occurs due to a numerical round-off in the solution of equations and, in case of two real solutions, choosing the correct one becomes an issue of fundamental importance. Choosing the wrong real solution can cause the procedure to double back on its tracks (i.e. converge to an already known configuration). The criterion for choosing the proper real solution in the arc-length method makes the main difference between the standard and the modified arc-length method. In both

methods, two solutions for the vector of unknown functions are calculated as

$$\boldsymbol{p}^{(1)} = \boldsymbol{p}_0 + \Delta\boldsymbol{p}_I + \Delta\lambda_1\Delta\boldsymbol{p}_{II},$$

$$\boldsymbol{p}^{(2)} = \boldsymbol{p}_0 + \Delta\boldsymbol{p}_I + \Delta\lambda_2\Delta\boldsymbol{p}_{II}, \tag{4.53}$$

where $\Delta\lambda_1$ and $\Delta\lambda_2$ are the first and the second solution of equation (4.50), respectively. The standard arc-length method uses the incremental vector of displacements between two last equilibrium configurations, $\boldsymbol{p}_\mu - \boldsymbol{p}_{\mu-1}$, and the incremental vectors of displacement between the two new configurations and the last equilibrium configuration, $\boldsymbol{p}^{(1)} - \boldsymbol{p}_\mu$, and, $\boldsymbol{p}^{(2)} - \boldsymbol{p}_\mu$, where μ denotes the last equilibrium configuration. It is assumed that the correct solution $\Delta\lambda_i$ is the one which gives the smallest scalar product $\varphi_i = (\boldsymbol{p}^{(i)} - \boldsymbol{p}_\mu) \cdot (\boldsymbol{p}_\mu - \boldsymbol{p}_{\mu-1})$, for $i = 1, 2$. This may be interpreted as finding the solution with a minimum 'angle' φ_i between $(\boldsymbol{p}^{(i)} - \boldsymbol{p}_\mu)$ and $(\boldsymbol{p}_\mu - \boldsymbol{p}_{\mu-1})$ in the solution hyper-space [13]. For an imaginary one-degree-of-freedom problem the idea is illustrated in Fig. 4.5.
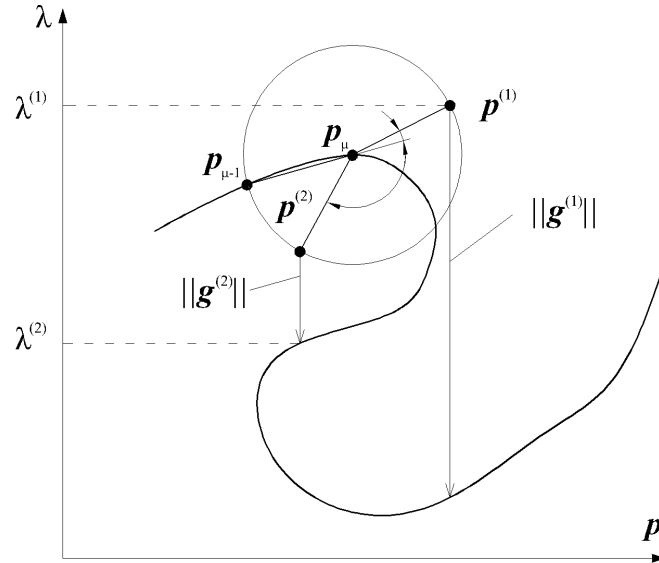
FIGURE 4.5: Difference between the standard and the modified arc-length method

In the vicinity of very sharp snap-backs, the method of selecting the solution according to the minimum angle criterion often fails due to the steepness of the load-displacement curve (see Fig. 4.5). The modified arc-length method, on the other hand, takes a different strategy. For both solutions (4.53) the global vector of residual forces (and the global tangent stiffness matrix) are calculated. If the Euclidian norm of the first global vector of residual forces is less than the

required tolerance, the first solution has converged and the next step initiates. If the required tolerance is not achieved, the increments of the vector of unknown functions, the vector of residual forces and the tangent stiffness matrix for the first solution are saved. The maximum degrees of delamination at the integration points $\overline{\beta}_\alpha(\tau)$ in all elements and all interconnections are saved as well. Then the second solution from (4.53) is used to calculate the vector of residual forces (and the tangent stiffness matrix) again. If the Euclidian norm of the second global vector of residual forces is less than the required tolerance, the second solution is taken and the next step initiates. In case that the norm does not satisfy this condition, the first and the second norm of the global vector of residual forces are compared and the solution with the lower residual norm is taken. Fig. 4.5 illustrates the reasoning behind this idea.

4.4.2.3 Fixed vs. adaptive arc-length

It is also possible do begin each load step with the same arc-length parameter c or to modify it depending on a desired criterion, like, for instance [2],

$$c_{i+1} = \sqrt{\frac{N_{it}^d}{N_{it}^p}} c_i, \tag{4.54}$$

where N_{it}^p is the number of iterations needed for convergence at increment i and N_{it}^d is a user-defined 'desired' number of iterations. This is a very effective tool to reduce the computational time because large load steps are thus taken always as the convergence is good. On the other hand, setting non-realistically small N_{it}^d can lead to a continuous reduction of c and the computational time that tends to infinity. Thus, N_{it}^d has to be carefully chosen depending on the problem analysed. However, if the intention is to plot an accurate load-displacement diagram, the best option is to have a well chosen constant arc-length c, rather than the adaptive arc-length which may skip many interesting highly-curved regions in the load-displacement diagram.

4.5 Numerical examples

In this section the presented model is tested for mode I, mode II and mixed-mode delamination.

4.5.1 Mode I delamination example

This example is the standard test for mode I delamination known as the *Double cantilever beam (DCB) test.* The specimen [2] is shown in Fig. 4.6 with the corresponding geometrical properties (the width of the beam is 20 mm), boundary conditions and the loading which causes the notch to open vertically and then propagate to the left-hand side of the beam as the interconnection delaminates in pure mode I.
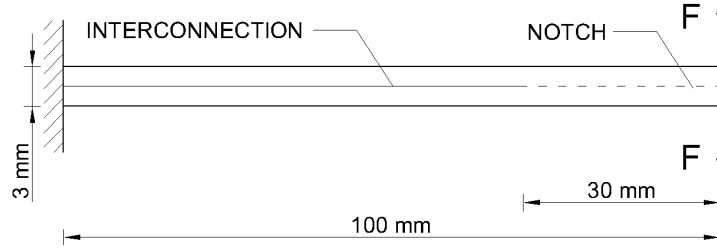
FIGURE 4.6: Test specimen for the DCB test

In the original example [2], orthotropic material data is given, with two Young's moduli, one shear modulus and two Poisson's coefficients, which for the beam constitutive model (3.21) is reduced only to $E_i = 135.3$ GPa, $G_i = 5.2$ GPa, (the beam is modelled as a two-layer beam where $i = 1, 2$). For the interconnection (index α is omitted since there is only one interconnection) $G_{cj} = 0.28$ N/mm, $d_{0j} = 10^{-7}$ mm and $t_{0j} = 57$ MPa, $j = 1, 2$. From these values the penalty stiffness parameters are computed according to (4.18) as $S_j = \omega_{0j}/d_{0j} = 5.7 \cdot 10^8$ N/mm^3, while the relative displacement at which complete delamination occurs is according to (4.13) $d_{cj} = 2G_{cj}/t_{0j} = 9.825 \cdot 10^{-3}$ mm. The results of the analysis for various FE meshes are presented in Fig. 4.7 where the relation between the applied force and the vertical displacement at the free end has been shown. The beam is modelled as a two-layered beam which is connected with the interconnection only between the clamped end and the notch. The beam and the interconnection are

78

divided in finite elements of equal length. Thus, for 100 beam finite elements 70 interconnection finite elements are used and this number has been doubled three times until the finest mesh of 800 beam finite elements and 560 interconnection finite elements has been obtained. The total number of degrees of freedom is 606 for the 100 element mesh, 1206 for the 200 element mesh, 2406 for the 200 elements mesh and 4806 for the 800 element mesh. On the other hand, in [2] a rectangular mesh of 4×400 eight-node plane strain (Q8) elements and 280 six-node interface elements (INT6) has been adopted, resulting with 11218 degrees of freedom. Using significantly less degrees of freedom the beam model gives satisfactory accuracy in comparison with plane strain finite element model and analytical solution (see Fig. 4.7). Derivation of the analytical closed-form solution for mode I delamination is presented in Appendix B. It can be easily shown that the maximum value of the force for the analytical solution is 68.87 N (intersection between the first linear branch and the curved branch), while the minimum value is 20.66 N (intersection between the curved branch and the second linear branch).
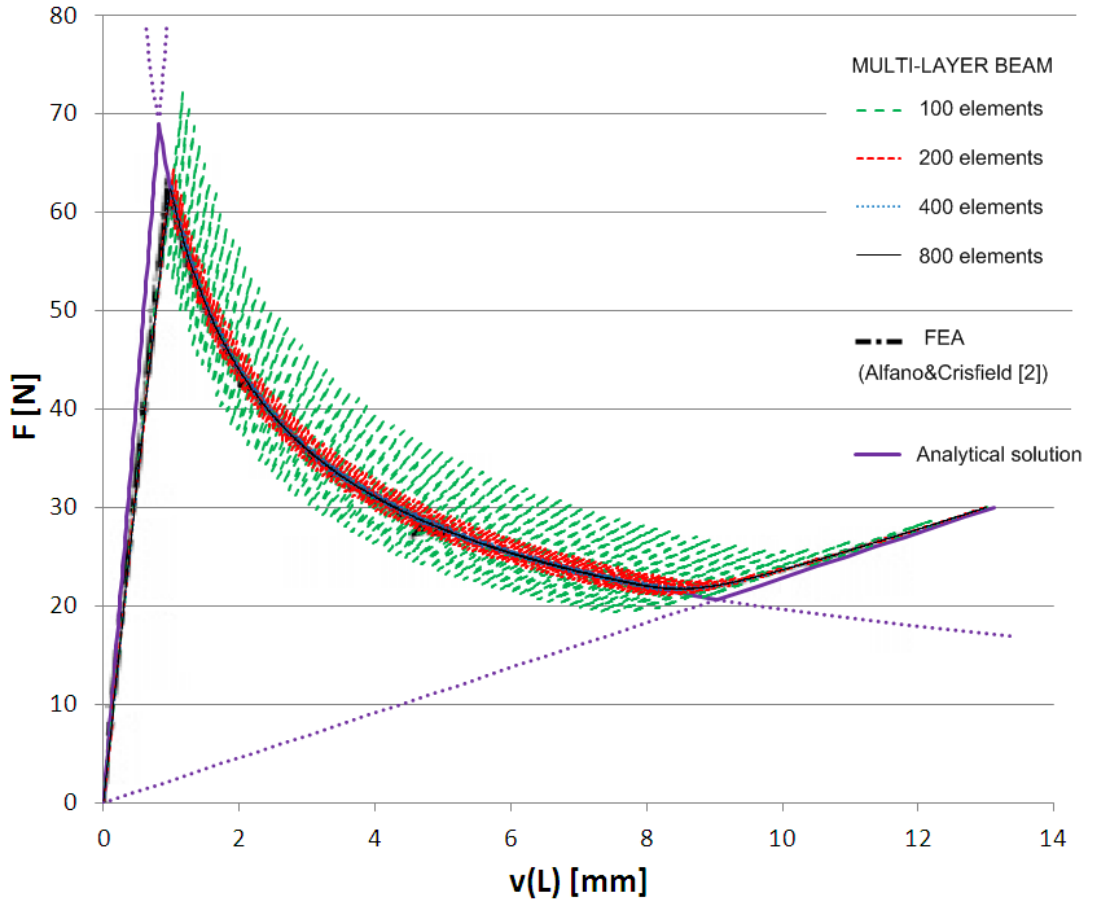
FIGURE 4.7: DCB test results for various FE meshes

The results are compared with the results from [2] and [36], where plane stress 2D finite elements were used, and show very good agreement. The liner-elastic part of behaviour of the system can be clearly observed, although, before the peak of the diagram, a slight softening (which is hard to distinguish graphically) occurs due to the start of the damage process in the integration points near the notch. For this reason the multi-layer beam solution in this part of the diagram shows a slightly softer behaviour in comparison with the analytical solution (see Fig. 4.7). The peak is reached when the interconnection at the first integration point (the one nearest to the notch) is completely lost (total damage). As the crack propagates from the notch to the clamped end, a decrease in overall stiffness of the system can be observed, which after a specific point ($F \approx 22$ N and $v(L) \approx 9$ mm), stabilises meaning that the interconnection is almost completely damaged and the stiffness of the system approximately equals the stiffness of the beam layers. It has to be emphasised that at the end of the presented test, total damage still did not occur at all integration points. It can be also seen that, depending on the meshing, oscillations around the exact solution during the delamination process occur. This phenomenon is mentioned earlier and is caused by the discretisation in numerical integration which is obviously mesh dependent. A closer look at the peak of the diagram is shown in Fig. 4.8 where it can be observed that for all meshes a certain amount of oscillations around the exact solution is obtained, but the phenomenon is reduced by increasing the number of integration points through an increased number of finite elements.

4.5.2   Mode II delamination example

The example presented next was proposed by Mi *et al.* [38] and its geometrical properties are shown in Fig. 4.9, with width of the beam $b_i = 1$ mm ($i = 1, 2$, beam is again modelled as a two-layer beam) and a variable notch length a_0. Material properties of the beam are $E_i = 135300$ N/mm^2, $G_i = 54120$ N/mm^2, while for the interconnection $Gcj = 4.0$ N/mm, $t_{0j} = 57$ N/mm^2 and $d_{0j} = 10^{-7}$ mm, $j = 1, 2$. In the same manner as in the previous numerical example, $d_{cj} = 0.14$ mm and $S_j = 5.7 \cdot 10^8$ N/mm^3 are obtained.
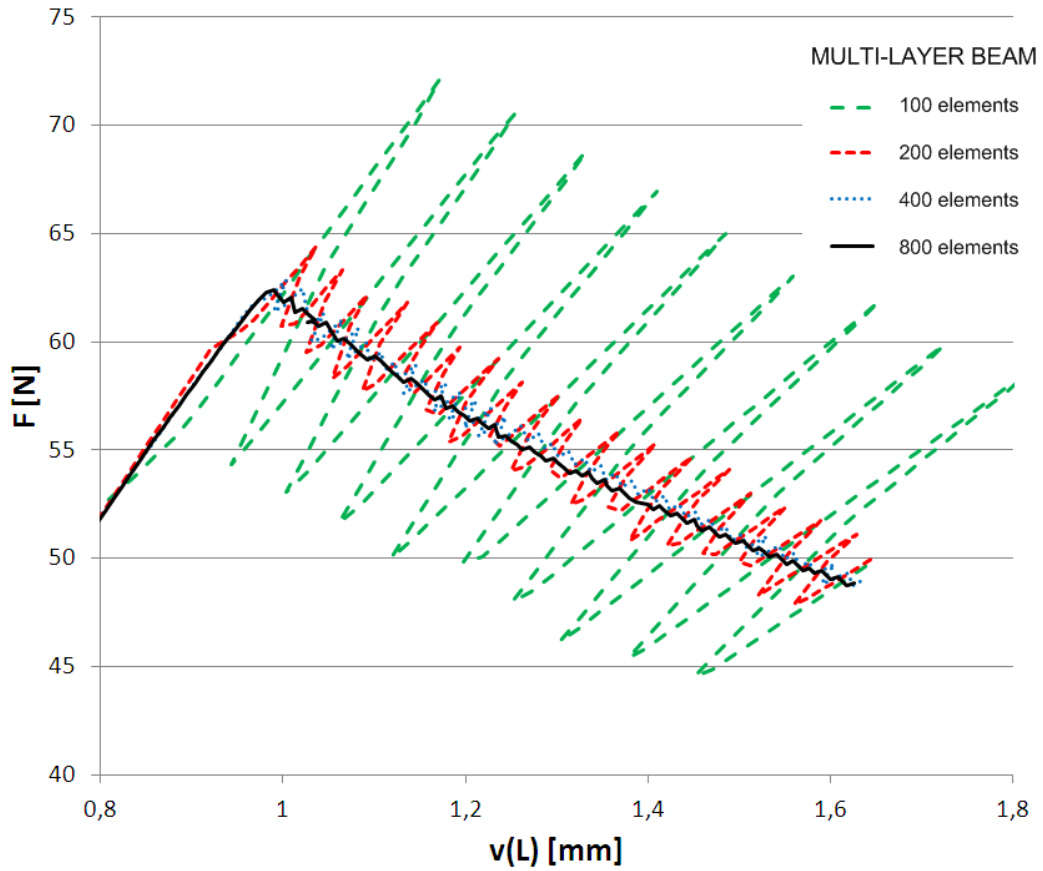
FIGURE 4.8: Mesh dependence on the DCB test results for various FE meshes
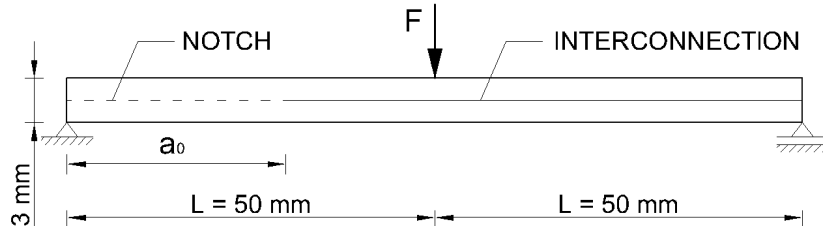
FIGURE 4.9: Test specimen for the mode II delamination test

The force F causes the two layers of the beam to slip against each other causing the pure mode II delamination at the interconnection. Obviously, penetration between the layers must be suppressed which is by default done by the mixed-mode interconnection finite elements, while the notch is modelled using interconnection elements with zero stiffness in mode II and a high penalty stiffness S_2 in mode I . The results presented in Fig. 4.10 show the load - midspan deflection relationship. Mesh dependence in this example is less pronounced than in the mode I example, and it can be observed that even for rather coarse meshes the results are very close to the converged ones. Similar behaviour as in the previous example can be noted in the linear elastic range, with a decrease in overall stiffness after the peak

load has been reached and subsequent hardening eventually leading to a linear-elastic behaviour with completely damaged interconnection. The results presented in this work show a very good accordance with the results presented in [38] which were obtained using the 2D plane stress finite elements for the bulk material. It can be also noticed that the results obtained with the multi-layer beam model, compared with the numerical results presented in [38], show better agreement (almost coincide) with the analytical results for the delaminations (derivation of the analytical solution is presented in Appendix B). Since in [38] the mesh data for the FEA solution has not been provided, the comparison between the total number of degrees of freedom for the beam and the plane finite element model is not presented.
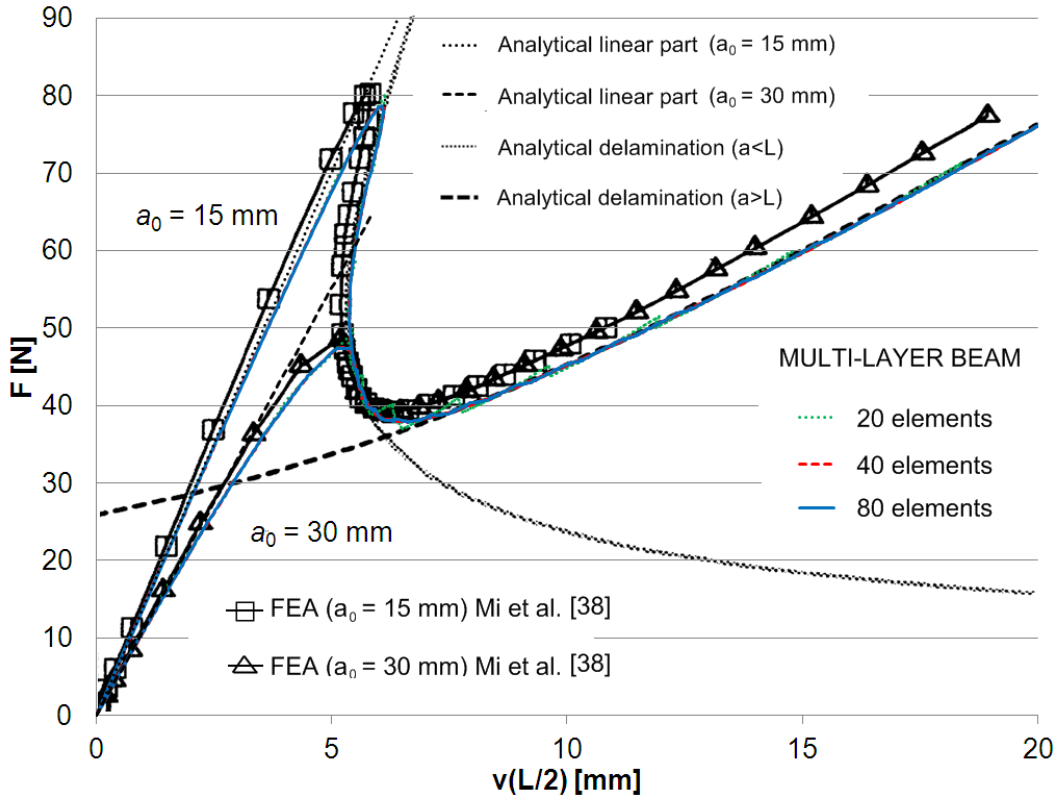
FIGURE 4.10: Load - midspan deflection diagram for the mode II delamination test

4.5.3 Single mixed-mode delamination example

This example, proposed by Mi *et al.* [38], too, is very similar to the mode II delamination example and is shown in Fig. 4.11. Geometrical properties, as well as the material properties for the interconnection, are the same as in the mode II

delamination example, except that the results are given only for $a_0 = 30$ mm. The material properties for the bulk material in [38] are given as for the orthotropic material, with two Young's moduli, one shear modulus and two Poisson's coefficients, while in the present model only the Young's modulus in the longitudinal direction and the shear modulus in the corresponding transverse direction are used as $E_i = 135300$ N/m^2 and $G_i = 5200$ N/mm^2, $i = 1, 2$. In this example two forces $F_1 = 0.4535 F_2$ and F_2 are applied to the system. The force F_2, as in the previous example, causes a pure mode II delamination at the interconnection, while the force F_1 causes a pure mode I delamination. When both forces are acting on the system, the mixed-mode delamination at the interconnection is caused.
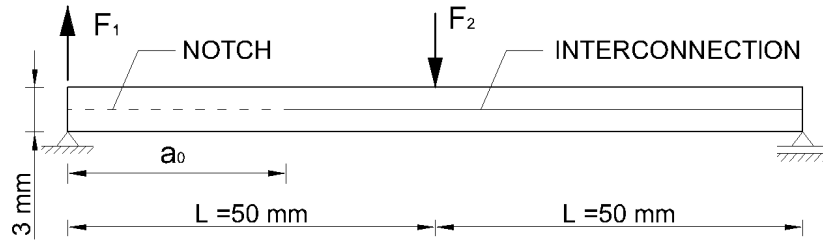
FIGURE 4.11: Test specimen for the mixed-mode delamination test

The results of the test are plotted in Fig. 4.12, showing the relationship between the load F_1 and the vertical displacement at the left-hand side of the beam. Similar behaviour as in the two previous examples can be observed, considering the shape of the diagram and the meshing influence on the results. The results from the multi-layer beam model agree very well with the numerical results from [38], where 2D plane-stress finite elements and two criteria (linear $\eta = 2$ and eliptical $\eta = 4$) for the mixed-mode delamination parameter (4.14) were used. In the presented multi-layer beam model only linear criterion with $\eta = 2$ has been used, and considering that the numerical results in [38] are obtained for an orthotropic material model, the agreement of the results is more than satisfactory. The analytical results for delamination [38] also show excellent agreement with the numerical results. It has to be added, however, that in contrast to the earlier single-mode analytical solutions, there exist different interpretations of the mixed-mode analytical model, see e.g. [65].
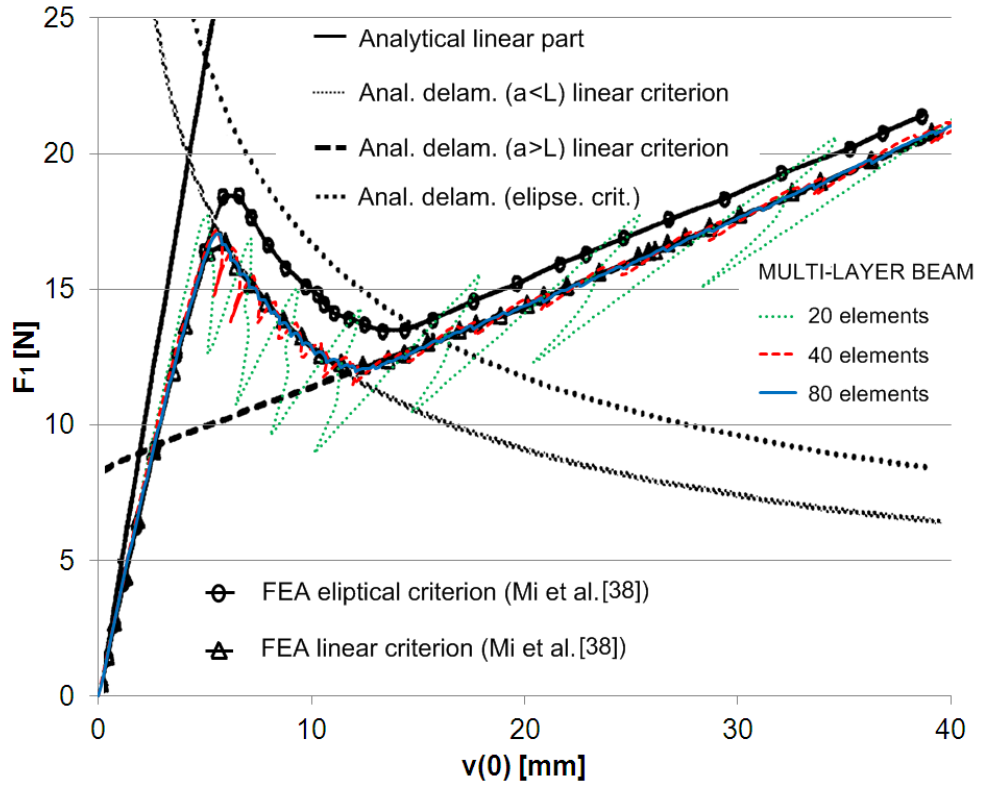
FIGURE 4.12: Load - vertical displacement at the left-hand side diagram for the mixed-mode delamination test

4.5.4 Double mixed-mode delamination example

Based on an experimental investigation of a multi-layered specimen manufactured from HTA913 carbon-epoxy material, numerical models are presented by Robinson *et al.* [49] and later by Alfano and Crisfield [2]. The specimen is supported only at the bottom of the left-hand side with a vertical force F acting at the top of the left-hand side causing a crack to propagate first as a continuation of the upper initial crack only, but later along both initial cracks simultaneously (see Fig. 4.13). The HTA913 specimen is made of 18 layers of equal thickness, where the initial cracks are located between the 10th and the 11th layer and between the 12th and the 13th layer (counted from the bottom). Since it is assumed that all the other interlayer connections are rigid, a multi-layer beam model is specified as having three layers and two interconnections. The geometry of the specimen is shown in Fig. 4.13, where $a = 20$ mm, $H = 3.18$ mm and width $B = 20$ mm.

Orthotropic material properties for HTA913 given in [49] are adapted for the beam model as $E_i = 115.0$ GPa, $G_i = 4.5$ GPa, $(i = 1, 2, 3)$, whereas for the
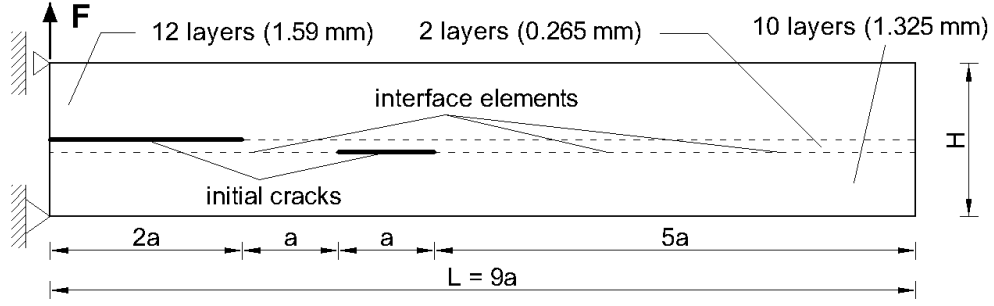
FIGURE 4.13: Specimen for the double mixed-mode delamination

interconnection, according to [2], material properties $G_{c1,\alpha} = 0.80$ N/mm, $G_{c2,\alpha} = 0.33$ N/mm, $\omega_{01,\alpha} = 7.0$ MPa, $\omega_{02,\alpha} = 3.3$ MPa and $d_{0j,\alpha}/d_{cj,\alpha} = 10^{-6}$, where $\alpha = 1, 2$ and $j = 1, 2$, are used. It can be further derived that $d_{c1,\alpha} = 2G_{c1,\alpha}/\omega_{01,\alpha} = 0.23$ mm, $d_{c2,\alpha} = 2G_{c2,\alpha}/\omega_{02,\alpha} = 0.2$ mm, $d_{01,\alpha} = 2.3 \cdot 10^{-7}$ mm, $d_{02,\alpha} = 2 \cdot 10^{-7}$ mm, $S_{1,\alpha} = t_{01,\alpha}/\omega_{01,\alpha} = 3.06 \cdot 10^7$ N/mm³ and $S_{2,\alpha} = t_{02,\alpha}/\omega_{02,\alpha} = 1.65 \cdot 10^7$ N/mm³.

In Fig. 4.14 a comparison between the multi-layer beam model and the model proposed by Alfano and Crisfield [2] is shown. The vertical displacement of the top layer at the left-hand side of the beam is plotted against the applied load F. Alfano and Crisfield have used a 3×360 QM4 + 680 INT4 mesh with a total of 4322 degrees of freedom and the tangent predictor for the solution (see [2] for more details). On the other hand, for the multi-layer beam model, two meshes with two-node beam finite elements and INT4 interface elements are adopted. 3-point Newton-Cotes integration is used for the INT4 interface elements. The first mesh with 180 finite elements uses 1629 degrees of freedom, while the second mesh with 360 finite elements uses 3249 degrees of freedom. It can be noted that the results obtained using the multi-layer beam model show excellent agreement with the converged solution using 2D othotropic plane-strain finite elements and use significantly less degrees of freedom.

The results shown in Fig. 4.14 are obtained using the model where reference axes of all three layer coincide with their centroidal axes ($a_i = h_i/2$, $i = 1, 2, 3$). However, changing the position of reference axes of the layers has an influence on the results, which is shown in Fig. 4.15. The first position is as mentioned, while in the second position the reference axis of the middle layer is positioned in the middle of the beam (i.e. on top of this layer, $a_2 = h_2$) and the two remaining reference axes are
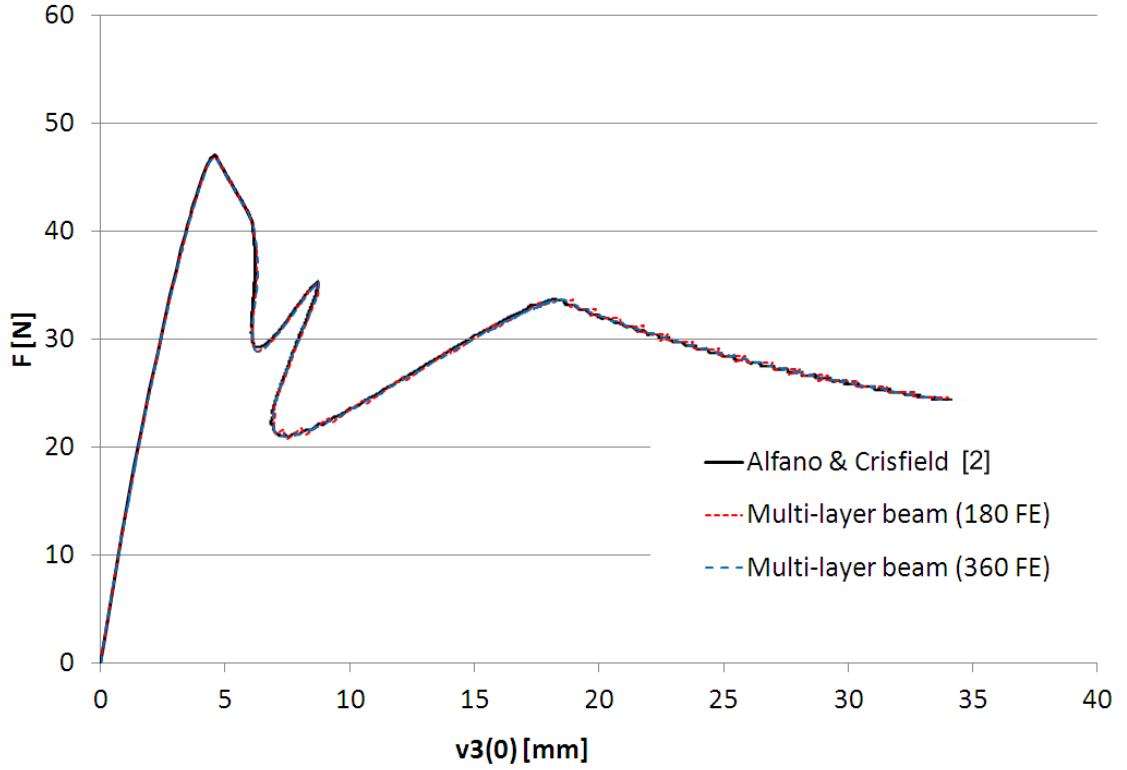
FIGURE 4.14: Comparison of the results for the double mixed-mode delamination example

positioned symmetrically with respect to the middle axis with $a_1 = a_3 = H/4$. The third position is the same as the second, only that the reference axis of the second layer now coincides with the reference axis of the third layer and $a_2 = (h_2 - h_1)/2$. Other positions, such as a position where all reference axes lay on the centroidal line, cause numerical problems and no acceptable solutions can be obtained. At this point of investigation we only recommend to keep the reference axes of the layers always in line with their centroidal axes in order to obtain the desired results. However, more investigation on the influence of the reference axes position on the results is planned in order to propose an optimal position of the layers' reference axes.

In the work which follows Reference [2], Alfano and Crisfield, have examined the influence of variation of some interface material parameters, while keeping the energy release rate constant, on the results of the same double mixed-mode delamination problem (see [3] for details). Three sets of material properties used in this comparison are presented in Table 4.1. It can be observed that all the three sets have identical energy release rates $G_{cj,\alpha}$ and penalty stiffness parameters $S_{j,\alpha}$, where $j = 1, 2$, but other quantities relevant for the interconnection significantly
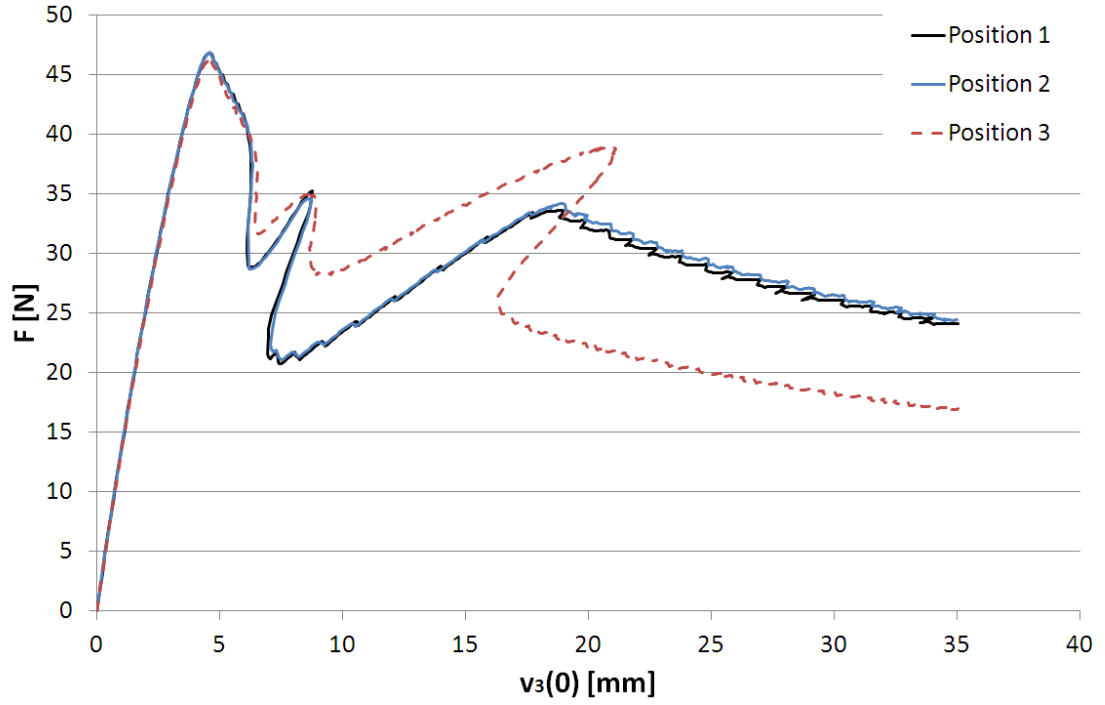
FIGURE 4.15: Influence of the position of the layers' reference axes on the results

differ. This means that the area under the relative displacement-contact traction diagram in Fig. 4.3, as well as the slope of the linear-elastic branch remains the same in all three cases, but the peak contact traction $\omega_{0j,\alpha}$ and maximum relative displacement $d_{cj,\alpha}$ are different.

TABLE 4.1: Three sets of material properties for the interconnection for the double mixed-mode delamination example

Case	$G_{c1,\alpha}$ [N/mm]	$G_{c1,\alpha}$ [N/mm]	$d_{0j,\alpha}/d_{cj,\alpha}$	$\omega_{01,\alpha}$ [MPa]	$\omega_{02,\alpha}$ [MPa]	$d_{0j,\alpha}$ [mm]	$d_{cj,\alpha}$ [mm]	$S_{1,\alpha}$ [N/mm^3]	$S_{2,\alpha}$ [N/mm^3]
A	0.8	0.33	$5 \cdot 10^{-5}$	8.0	3.3	$1 \cdot 10^{-5}$	0.2	$8 \cdot 10^5$	$3.3 \cdot 10^5$
B	0.8	0.33	$1.25 \cdot 10^{-3}$	40.0	16.5	$5 \cdot 10^{-5}$	0.04	$8 \cdot 10^5$	$3.3 \cdot 10^5$
C	0.8	0.33	$5 \cdot 10^{-3}$	80.0	33.0	$1 \cdot 10^{-4}$	0.02	$8 \cdot 10^5$	$3.3 \cdot 10^5$

In this example, two different non-uniform finite element meshes are used. The horizontal domain is divided in five zones. The first zone, according to Fig. 4.13, is near the left-hand side of the beam with the initial crack along the upper interface ($\alpha = 2$), while the second zone covers the initially uncracked part of the beam between the two initial cracks, and the third zone covers the region of the second initial crack, which has been placed along the lower interface ($\alpha = 1$). The initially undamaged right-hand part of the beam is divided in two zones, zone 4, where delamination is expected, and zone 5, where no delamination is expected. In contrast to the previous example (see Fig. 4.13), this part of the beam in this

example is 70 mm long. However, this difference does not influence the results as long as cracks remain sufficiently distant from the right-hand end of the specimen. The lengths of the meshing zones, along with the number of finite elements for both meshes are given in Table 4.2.

TABLE 4.2: Two finite element meshes for the double mixed-mode delamination example with different material properties for the interconnection

	Zone 1	Zone 2	Zone 3	Zone 4	Zone 5	Total
Length [mm]	40	20	20	50	20	150
Initial crack	$\alpha = 2$	none	$\alpha = 1$	none	none	
Mesh 1 / No. of FE	2	20	20	50	5	97
Mesh 2 / No. of FE	4	40	40	100	5	189

In this example, in contrast to the one previously presented, interface elements with no contact tractions, except in compression in mode I, are used at the notches. This feature gives more realistic behaviour of the model (penetration between layers at the notches is almost completely prevented) so the second peak in Fig. 4.14 ($v_3(0) \approx 9$ mm and $F \approx 35$ N), which is obviously a non-physical artefact of the model, disappears. Compression tractions in this example can occur only at the bottom notch in which they grow as the upper crack approaches it, but as soon as the upper crack reaches the horizontal position of the start of the bottom notch, delamination and crack propagation in the bottom notch starts, too. After that, the upper crack propagation is slowed down, while the bottom crack propagates more rapidly. In [3], no interface elements are inserted between the middle and the bottom layer in meshing zones 1 and 2, i.e. the left-hand side of the bottom interconnection is assumed to be absolutely rigid, which is justified, since the results show that the bottom crack propagates only to the right. In the present work, interface elements with 100 times higher values of penalty stiffness parameters are used at the left-hand side of the bottom interface.

In Fig. 4.16, a comparison between the multi-layer beam model and the model proposed by Alfano and Crisfield [3], which uses 2D plane-strain finite elements with interface elements, is shown. As in [3], mesh 1 is used for case A, while mesh 2 is used for cases B and C according to Table 4.2. Three-node beam finite elements and six-node interface elements (INT6) are used in the multi-layer beam model. 3-point Newton-Cotes integration is used for the interface elements. Using 97 QPSN8 finite elements per layer with INT6 interface elements at the interconnections, as

did Alfano and Crisfield [3], results in 2938 degrees of freedom for case A, while using 189 QPSN8 finite elements per layer with INT6 interface elements at the interconnections results in 5510 degrees of freedom for cases B and C. On the other hand, using the presented multi-layer beam model according to Table 4.2 gives 1755 degrees of freedom for mesh 1 (case A) and 3411 degrees of freedom for mesh 2 (cases B and C). Even though the total number of degrees of freedom is considerably reduced, the multi-layer beam model still gives results that, for the most critical part of the load-displacement diagram, show an excellent agreement with the results presented by Alfano and Crisfield [3] (see Fig. 4.16). It can be also noted that the cases B and C show better agreement with the experimental results [49].

Oscillations, typical for finite element analysis of delamination problems, however, can still be noted in the diagram, especially in the final softening branch. Using mesh 1 for the case A, a very small amount of oscillations occurs, while using a finer mesh 2 for the cases B and especially C, oscillations become more pronounced. Thus it can be concluded that the influence of material parameters of the interconnection has even bigger influence on the oscillations of the results than the meshing itself. Compared to the plane-strain finite element formulation [3], the present model shows larger oscillations which can be reduced using numerical integration of higher order (more integration points).

In Fig. 4.17 a comparison of the results obtained using different order of Newton-Cotes numerical integration is shown for the last part of the diagram. It can be noted that using 4 integration points instead of 3, the oscillations reduce considerably and the results are much closer to those proposed by Alfano and Crisfield [3]. On the other hand, further increase in number of integration points does not lead to any significant improvement of the results. It has to be emphasized that results in Fig. 4.17 correspond to the FE mesh with 20 elements (instead of 40) in the second zone according to Table 4.2, which however does not have any significant influence in this part of diagram.
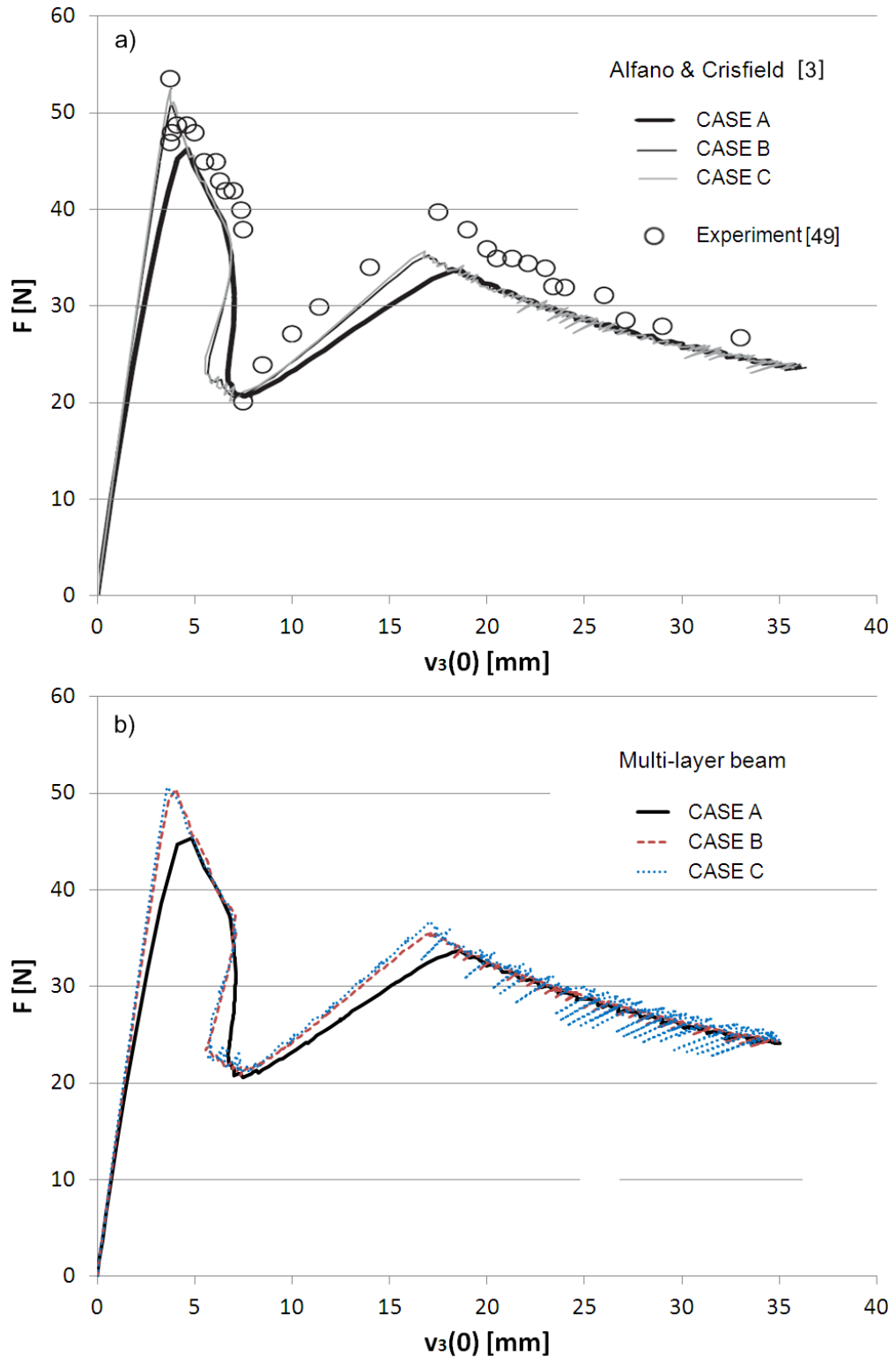
FIGURE 4.16: Results for different cases of material properties of the interconnection: a) plane-strain finite element model from literature, and b) multi-layer beam model

4.6 Conclusions

In the present work a multi-layer beam with interconnection allowing for delamination between layers has been presented. The bulk material is modelled using
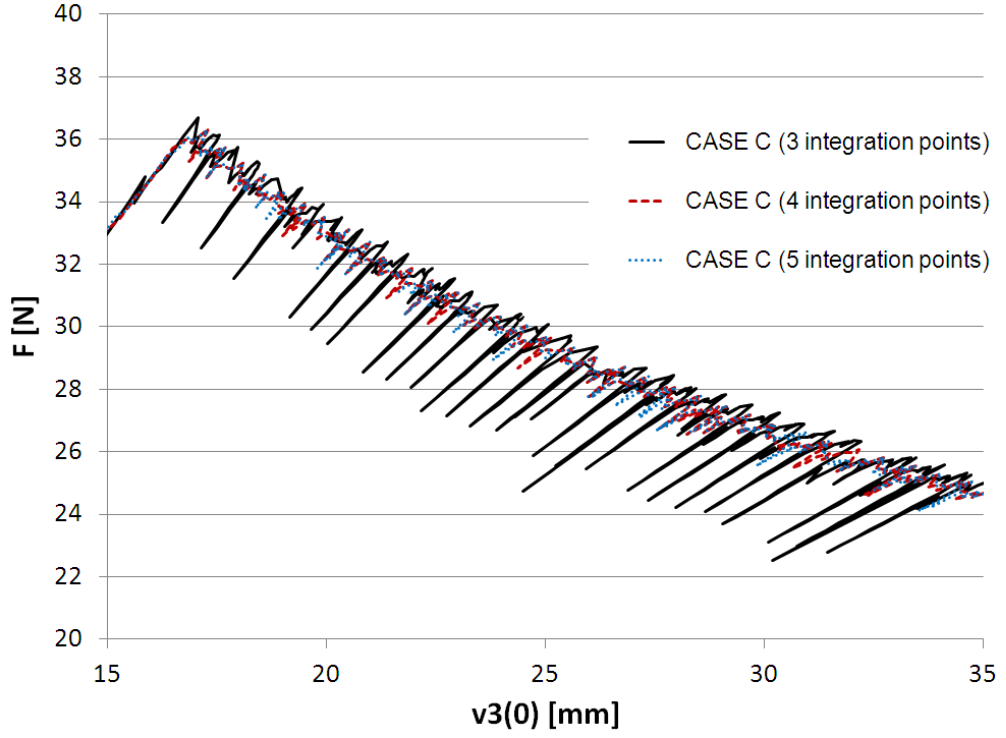
FIGURE 4.17: Comparison of the results for different order of numerical integration

beam finite elements, while the cohesive-zone model incorporated into the interface elements proposed by Alfano and Crisfield [2] is used for the interconnection. Modelling the bulk material structure as beams, in comparison with commonly used 2D plane-stress finite elements, reduces the total number of unknown functions, which is one of the biggest benefits of the presented model. The results of the numerical examples presented in the present work agree very well with the results from the literature (which use 2D plane-stress finite elements for the bulk material).

5 CONCLUSIONS AND FUTURE WORK

In this thesis several aspects of modelling multi-layer plane structures using the beam theory have been presented. They can be systematised in three basic parts:

1. analytical solution of geometrically and materially linear problem of multi-layer beam with compliant interconnections

2. finite element formulation for geometrically exact multi-layer beam with a rigid interlayer connection

3. finite element formulation for geometrically linear multi-layer beam with non-linear material law at the interconnection

In the first part, the differential equations for different conditions at the interconnection have been derived and the solution procedure has been proposed. Influence of different interlayer conditions on the mechanical behaviour of layered beams has been studied on a couple of numerical examples. It has been shown that by varying interconnection stiffnesses in tangential and normal direction, the mechanical behaviour of composite beam is always between two limits states: a composite beam with completely rigid connection (which is often used in engineering practice) and a composite beam with no connection. One of the shortcomings of the models which allow for the interlayer uplift is the lack of ability to prevent the penetration between the adjacent layers in case of compressive normal tractions at the interconnection. However, the presented analytical solution is very useful for the analysis of layered composite structures where small deformations and rotations occur, and material behaviour is in the linear-elastic range, as is often the case in applications in civil engineering.

The finite element formulation from the second part is particularly appropriate for modelling homogeneous beams using the multi-layer discretization, perhaps more than for modelling the composite beams where usually a certain amount of

interlayer slip or/and uplift occurs. However, if the stiffness of the interconnection is considerably greater than the stiffness of the bulk material and the displacements and rotations are not small, this model can be successfully utilised. In the presented numerical examples, which include warping of the cross-section, it has been shown that in comparison with the models using 2D finite elements, for comparable meshes, the multi-layer beam model proposed uses significantly less degrees of freedom and gives results with satisfactory accuracy. One of the main disadvantages of the multi-layer beam model in this comparison is the transverse incompressibility, which is included in the basic beam theory. Transverse deformability could be eventually introduced by using some higher order beam theories or by inserting deformable interconnections of finite thickness between the layers.

In the third part, a mixed-mode delamination problem has been examined using beam finite elements for the bulk material, which, to the best of author's knowledge, has not been presented yet in the literature. A very detailed description of the solution procedure (modified arc-length method), which is necessary to obtain convergence is such problems, is presented. In comparison with commonly used 2D finite elements, the beam finite elements for the bulk material give good accuracy of the results with less degrees of freedom. Although in the present work only examples with a single interconnection between two layers have been shown, the presented model can be used in case of multi-layer beams with multiple interconnections. It is also possible to extend this model to a geometrically non-linear analysis. The main issue which in this case remains is how to define the matrix $\mathbf{\Lambda}_\alpha$ from (4.12) in an appropriate manner. Such a model would allow to analyse problems with large deformations and rotations, such as peel test. The model may be easily extended to a uniaxial materially non-linear constitutive law for the bulk material. Also, further analyses of the influence of the layers' reference axes position on the results are needed.

List of Figures

List of Tables

Appendix A

Linearization of the nodal vector of residual forces for the geometrically non-linear multi-layer beam with a rigid interconnection

The linearisation of the nodal vector of residual forces is performed as

$$
\Delta \boldsymbol{g}_j = \sum_{i=1}^{n} \left\{ \int_0^L \boldsymbol{\Psi}_j^{\mathsf{T}} \left[\Delta \boldsymbol{B}_i^{\mathsf{T}} \left(\boldsymbol{D}_i^{\mathsf{T}} \begin{Bmatrix} \boldsymbol{n}_i \\ n_{i,3} \end{Bmatrix} - \begin{Bmatrix} \boldsymbol{f}_i \\ w_i \end{Bmatrix} \right) + \boldsymbol{B}_i^{\mathsf{T}} \left(\Delta \boldsymbol{D}_i^{\mathsf{T}} \begin{Bmatrix} \boldsymbol{n}_i \\ n_{i,3} \end{Bmatrix} + \right. \right. \right.
$$

$$
\left. \left. \left. + \boldsymbol{D}_i^{\mathsf{T}} \Delta \boldsymbol{L}_i^{\mathsf{T}} \boldsymbol{C}_i \begin{Bmatrix} \boldsymbol{\gamma}_i \\ \kappa_i \end{Bmatrix} + \boldsymbol{D}_i^{\mathsf{T}} \boldsymbol{L}_i^{\mathsf{T}} \boldsymbol{C}_i \begin{Bmatrix} \Delta \boldsymbol{\gamma}_i \\ \Delta \kappa_i \end{Bmatrix} \right) \right] \mathrm{d}X_1 - \right.
$$

$$
\left. - \left(\delta_{j,1} \Delta \boldsymbol{B}_{i,0}^{\mathsf{T}} \begin{Bmatrix} \boldsymbol{F}_{i,0} \\ W_{i,0} \end{Bmatrix} + \delta_{j,N} \Delta \boldsymbol{B}_{i,L}^{\mathsf{T}} \begin{Bmatrix} \boldsymbol{F}_{i,L} \\ W_{i,L} \end{Bmatrix} \right) \right\}, \tag{A.1}
$$

where

$$
\begin{Bmatrix} \boldsymbol{n}_i \\ n_{i,3} \end{Bmatrix} = \boldsymbol{L}_i^{\mathsf{T}} \boldsymbol{C}_i \begin{Bmatrix} \boldsymbol{\gamma}_i \\ \kappa_i \end{Bmatrix}, \tag{A.2}
$$

and the interpolation functions in $\boldsymbol{\Psi}_j$ are assumed to be configuration-independent. The linearized matrices and vectors are

$$
\Delta \boldsymbol{B}_i = \begin{bmatrix} 0\boldsymbol{I} & \boldsymbol{0} & \dots & \boldsymbol{0} & -\Delta\theta_\zeta d_{i,\zeta} \boldsymbol{t}_{\zeta,2} & \dots & -\Delta\theta_\xi d_{i,\xi} \boldsymbol{t}_{\xi,2} & \boldsymbol{0} & \dots & \boldsymbol{0} \\ \boldsymbol{0}^{\mathsf{T}} & 0 & \dots & 0 & 0 & \dots & 0 & 0 & \dots & 0 \end{bmatrix}, \tag{A.3}
$$

$$
\Delta \boldsymbol{D}_i = \begin{bmatrix} 0\boldsymbol{I} & -\hat{\boldsymbol{t}}_3 \Delta \boldsymbol{u}_i' \\ \boldsymbol{0}^{\mathsf{T}} & 0 \end{bmatrix}, \tag{A.4}
$$

$$
\Delta \boldsymbol{L}_i^{\mathsf{T}} = \begin{bmatrix} \Delta\theta_i \hat{\boldsymbol{t}}_3 & \boldsymbol{0} \\ \boldsymbol{0}^{\mathsf{T}} & 0 \end{bmatrix} \boldsymbol{L}_i^{\mathsf{T}}, \tag{A.5}
$$

$$
\begin{Bmatrix} \Delta \boldsymbol{\gamma}_i \\ \Delta \kappa_i \end{Bmatrix} = \boldsymbol{L}_i \boldsymbol{D}_i \begin{Bmatrix} \Delta \boldsymbol{u}_i \\ \Delta \theta_i \end{Bmatrix} = \boldsymbol{L}_i \boldsymbol{D}_i \boldsymbol{B}_i \Delta \boldsymbol{p}_f, \tag{A.6}
$$

where $\Delta \boldsymbol{p}_f^\mathsf{T} = \langle \Delta \boldsymbol{u}^\mathsf{T} \quad \Delta \theta_1 \quad \ldots \quad \Delta \theta_n \rangle$. Parts of expression (A.1) are further written as

$$\Delta \boldsymbol{B}_i^\mathsf{T} \boldsymbol{D}_i^\mathsf{T} \begin{Bmatrix} \boldsymbol{n}_i \\ n_{i,3} \end{Bmatrix} = (\boldsymbol{J}_{i,1} + \boldsymbol{J}_{i,2}) \Delta \boldsymbol{p}_f, \tag{A.7}$$

$$\Delta \boldsymbol{D}_i^\mathsf{T} \begin{Bmatrix} \boldsymbol{n}_i \\ n_{i,3} \end{Bmatrix} = \boldsymbol{H}_i \boldsymbol{B}_i \Delta \boldsymbol{p}_f, \tag{A.8}$$

$$\Delta \boldsymbol{L}_i^\mathsf{T} \boldsymbol{C}_i \begin{Bmatrix} \boldsymbol{\gamma}_i \\ \kappa_i \end{Bmatrix} = \boldsymbol{P}_i \boldsymbol{B}_i \Delta \boldsymbol{p}_f, \tag{A.9}$$

$$\Delta \boldsymbol{B}_i \begin{Bmatrix} \boldsymbol{f}_i \\ w_i \end{Bmatrix} = \boldsymbol{J}_{i,f} \Delta \boldsymbol{p}_f, \tag{A.10}$$

$$\Delta \boldsymbol{B}_{i,\chi} \begin{Bmatrix} \boldsymbol{F}_{i,\chi} \\ W_{i,\chi} \end{Bmatrix} = \boldsymbol{J}_{i,\chi} \Delta \boldsymbol{p}_f, \quad \chi = 0, L \tag{A.11}$$

where

$$\boldsymbol{H}_i = \begin{bmatrix} 0\boldsymbol{I} & \boldsymbol{0} \\ -\boldsymbol{n}_i^\mathsf{T} \hat{\boldsymbol{t}}_3 \frac{\mathrm{d}}{\mathrm{d}X_1} & 0 \end{bmatrix}, \tag{A.12}$$

$$\boldsymbol{P}_i = \begin{bmatrix} 0\boldsymbol{I} & \hat{\boldsymbol{t}}_3 \boldsymbol{n}_i \\ \boldsymbol{0}^\mathsf{T} & 0 \end{bmatrix}, \tag{A.13}$$

$$\boldsymbol{J}_{i,\eta} = \begin{bmatrix} 0\boldsymbol{I} & \boldsymbol{0} & \ldots & \boldsymbol{0} & \boldsymbol{0} & \ldots & \boldsymbol{0} & \boldsymbol{0} & \ldots & \boldsymbol{0} \\ \boldsymbol{0}^\mathsf{T} & 0 & \ldots & 0 & 0 & \ldots & 0 & 0 & \ldots & 0 \\ \vdots & \vdots & \ddots & \vdots & \vdots & & \vdots & \vdots & & \vdots \\ \boldsymbol{0}^\mathsf{T} & 0 & \ldots & 0 & 0 & \ldots & 0 & 0 & \ldots & 0 \\ \boldsymbol{0}^\mathsf{T} & 0 & \ldots & 0 & \beta_{i,\zeta}^\eta & \ldots & 0 & 0 & \ldots & 0 \\ \vdots & \vdots & & \vdots & \vdots & \ddots & \vdots & \vdots & & \vdots \\ \boldsymbol{0}^\mathsf{T} & 0 & \ldots & 0 & 0 & \ldots & \beta_{i,\xi}^\eta & 0 & \ldots & 0 \\ \boldsymbol{0}^\mathsf{T} & 0 & \ldots & 0 & 0 & \ldots & 0 & 0 & \ldots & 0 \\ \vdots & \vdots & & \vdots & \vdots & & \vdots & \vdots & \ddots & \vdots \\ \boldsymbol{0}^\mathsf{T} & 0 & \ldots & 0 & 0 & \ldots & 0 & 0 & \ldots & 0 \end{bmatrix}, \quad \eta \in \{1, 2, f, 0, L\}, \tag{A.14}$$

and for $k \in \langle \zeta, \ldots, \xi \rangle$

$$\beta_{i,k}^1 = d_{i,k} \boldsymbol{n}_i^\mathsf{T} \left(\theta_k' \boldsymbol{t}_{k,1} - \boldsymbol{t}_{k,2} \frac{\mathrm{d}}{\mathrm{d}X_1} \right), \tag{A.15}$$

$$\beta_{i,k}^2 = -d_{i,k} \boldsymbol{n}_i^\mathsf{T} \boldsymbol{t}_{k,2} \frac{\mathrm{d}}{\mathrm{d}X_1}, \tag{A.16}$$

$$\beta_{i,k}^f = -d_{i,k} \boldsymbol{f}_i^\mathsf{T} \boldsymbol{t}_{k,2}, \tag{A.17}$$

$$\beta_{i,k}^\chi = -d_{i,k} \boldsymbol{F}_{i,\chi}^\mathsf{T} \boldsymbol{t}_{k,2}, \quad (\chi = 0, L). \tag{A.18}$$

The derivation of matrices $\boldsymbol{J}_{i,1}$ and $\boldsymbol{J}_{i,2}$ is explained in detail. First, using expressions (A.3) and (3.33) we can obatin

$$\Delta \boldsymbol{B}_i^\mathsf{T} \boldsymbol{D}_i^\mathsf{T} = \begin{bmatrix} 0\boldsymbol{I} & \boldsymbol{0} & \ldots & \boldsymbol{0} & \boldsymbol{\lambda}_{i,\zeta} & \ldots & \boldsymbol{\lambda}_{i,\xi} & \boldsymbol{0} & \ldots & \boldsymbol{0} \\ \boldsymbol{0}^\mathsf{T} & 0 & \ldots & 0 & 0 & \ldots & 0 & 0 & \ldots & 0 \end{bmatrix}^\mathsf{T} = \boldsymbol{Y}_i^\mathsf{T} \tag{A.19}$$

where for $k \in \langle \zeta \ldots \xi \rangle$

$$\boldsymbol{\lambda}_{i,k} = \Delta\theta_k d_{i,k} \left(\theta_k' \boldsymbol{t}_{k,1} - \boldsymbol{t}_{k,2} \frac{\mathrm{d}}{\mathrm{d}X_1} \right) - \Delta\theta_k' d_{i,k} \boldsymbol{t}_{k,2}. \tag{A.20}$$

Matrix $\boldsymbol{Y}_i$ is then split into two parts, first one, $\boldsymbol{Y}_{1,i}$, containing the terms with $\Delta\theta_j$, and the second one, $\boldsymbol{Y}_{2,i}$, containing the term with $\Delta\theta_j'$. Thus, expession (A.7) can be written as

$$\Delta \boldsymbol{B}_i^\mathsf{T} \boldsymbol{D}_i^\mathsf{T} \begin{Bmatrix} \boldsymbol{n}_i \\ n_{i,3} \end{Bmatrix} = (\boldsymbol{Y}_{i,1} + \boldsymbol{Y}_{i,2})^\mathsf{T} \begin{Bmatrix} \boldsymbol{n}_i \\ n_{i,3} \end{Bmatrix} = (\boldsymbol{J}_{i,1} + \boldsymbol{J}_{i,2}) \Delta \boldsymbol{p}_f \tag{A.21}$$

from where it can be clearly seen that the coefficients $\beta_{i,k}^1$ and $\beta_{i,k}^2$ from matrices $\boldsymbol{J}_{i,1}$ and $\boldsymbol{J}_{i,2}$ (see expressions (A.12), (A.15) and (A.16)) are derived from the first and the second part of $\boldsymbol{\lambda}_{i,k}$ (A.20). The differential operator in (A.16) originates from $\Delta\theta_k'$ in expression (A.20). The coefficients $\beta_{i,k}^f$ and $\beta_{i,k}^\chi$ are computed analogously. The differential operator in matrix $\boldsymbol{J}_{1,i}$ is operating on the matrix $\boldsymbol{\Psi}_j$, while in matrices $\boldsymbol{J}_{2,i}$ and $\boldsymbol{H}_i$ it is operating on the vector $\Delta \boldsymbol{p}_f$. Matrices $\boldsymbol{J}_{1,0}$ and $\boldsymbol{J}_{1,L}$ are evaluated for $X_1 = 0$ and $X_1 = L$, respectively. By substituting

expressions (A.12)-(A.14) into (A.1) we obtain

$$\Delta \boldsymbol{g}_j = \sum_{i=1}^{n} \left\{ \int_0^L \boldsymbol{\Psi}_j^{\mathsf{T}} \left[(\boldsymbol{J}_{i,1} + \boldsymbol{J}_{i,2}) - \boldsymbol{J}_{i,f} + \boldsymbol{B}_i^{\mathsf{T}} \left(\boldsymbol{H}_i \boldsymbol{B}_i + \boldsymbol{D}_i^{\mathsf{T}} \boldsymbol{P}_i \boldsymbol{B}_i + \right. \right. \right.$$
$$\left. \left. \left. + \boldsymbol{D}_i^{\mathsf{T}} \boldsymbol{L}_i^{\mathsf{T}} \boldsymbol{C}_i \boldsymbol{L}_i \boldsymbol{D}_i \boldsymbol{B}_i \right) \right] \Delta \boldsymbol{p}_f \mathrm{d} X_1 - (\delta_{j,1} \boldsymbol{J}_{i,0} + \delta_{j,N} \boldsymbol{J}_{i,L}) \Delta \boldsymbol{p}_f \right\}. \quad \text{(A.22)}$$

We further interpolate the linear increments $\Delta \boldsymbol{p}_f$ using the same interpolation as for the test functions, i.e.

$$\Delta \boldsymbol{p}_f = \left\{ \begin{array}{c} \Delta \boldsymbol{u}(X_1) \\ \Delta \theta_1(X_1) \\ \vdots \\ \Delta \theta_n(X_1) \end{array} \right\} = \sum_{k=1}^{N} \boldsymbol{\Psi}_k(X_1) \left\{ \begin{array}{c} \Delta \boldsymbol{u}_k \\ \Delta \theta_{1,k} \\ \vdots \\ \Delta \theta_{n,k} \end{array} \right\} = \sum_{k=1}^{N} \boldsymbol{\Psi}_k(X_1) \Delta \boldsymbol{p}_k, \quad \text{(A.23)}$$

to obtain

$$\Delta \boldsymbol{g}_j = \sum_{k=1}^{N} \boldsymbol{K}_{j,k} \Delta \boldsymbol{p}_k, \quad \text{(A.24)}$$

where

$$\boldsymbol{K}_{j,k} = \sum_{i=1}^{n} \left(\int_0^L \left\{ \left(\boldsymbol{\Psi}_j^{\mathsf{T}} \boldsymbol{J}_{i,1} \right) \boldsymbol{\Psi}_k + \boldsymbol{\Psi}_j^{\mathsf{T}} \left[(\boldsymbol{J}_{i,2} \boldsymbol{\Psi}_k) - \boldsymbol{J}_{f,i} \boldsymbol{\Psi}_k + \boldsymbol{B}_i^{\mathsf{T}} \left(\boldsymbol{H}_i \boldsymbol{B}_i \boldsymbol{\Psi}_k \right) \right] + \right. \right.$$
$$\left. + \left(\boldsymbol{D}_i \boldsymbol{B}_i \boldsymbol{\Psi}_j \right)^{\mathsf{T}} \left[\boldsymbol{P}_i \boldsymbol{B}_i \boldsymbol{\Psi}_k + \boldsymbol{L}_i^{\mathsf{T}} \boldsymbol{C}_i \boldsymbol{L}_i \left(\boldsymbol{D}_i \boldsymbol{B}_i \boldsymbol{\Psi}_k \right) \right] \right\} \mathrm{d} X_1 - \quad \text{(A.25)}$$
$$\left. - \delta_{j,1} \delta_{k,1} \boldsymbol{J}_{i,0} - \delta_{j,N} \delta_{k,N} \boldsymbol{J}_{i,L} \right),$$

are $(2+n) \times (2+n)$ nodal stiffness matrices which are assembled into an element tangent stiffness matrix of dimensions $N(2+n) \times N(2+n)$ as $\boldsymbol{K} = [\boldsymbol{K}_{j,k}]$. In expression (A.25) some matrices are grouped in parentheses to emphasize and separate the action of the differential operators. For integration in (A.25) we use

$$\boldsymbol{\Psi}_k = \mu_k \boldsymbol{I}_{3\times3}, \quad \text{(A.26)}$$

where μ_k is the Lagrangian polynomial of order $N-1$ with $\mu_k(X_{1,l}) = \delta_{kl}$ and $\boldsymbol{I}_{3\times3}$ is a 3×3 identity matrix. Also, we perform the Gaussian quadrature with $N-1$ integration points in order to avoid shear-locking [61].

Appendix B

Closed-form solutions for mode I and mode II delamination

B.1 Mode I delamination

Closed-form solution for mode I delamination is derived for a double cantilever beam with initial crack according to Fig. 4.6. The deflection of the upper layer at the free end, $v_2(L)$, which is due to the symmetry of the system opposite to the deflection of the bottom layer, $v_1(L)$, before the interconnection is damaged and the initial crack propagates to the left reads

$$v_2(L) = -v_1(L) = \frac{Fa_0^3}{3EI},$$ (B.1)

where F is the force applied to each layer at the free end, a_0 is the length of the initial crack and EI is the bending stiffness of each layer. This solution corresponds with the linear branch of the analytical solution shown in Fig. 4.7.

When the damage of the interconnection starts and the crack propagates to the left $(a > a_0)$, strain energy due to bending of each layer at the crack tip is released. The crack will propagate when the strain energy rate per a unit of crack area reaches the critical energy release for mode I delamination. The strain energy rate at a crack tip reads

$$d\Phi = \frac{M^2(a)da}{2EI} = \frac{F^2a^2da}{EI}.$$ (B.2)

The critical energy release for mode I delamination can be thus expressed as

$$G_{Ic} = \frac{d\Phi}{bda} = \frac{F^2a^2}{bEI},$$ (B.3)

where b is the width of the beam. The deflection of the free end of the upper layer with the crack tip of the ongoing delamination can be then expressed as

$$v_2(L) = \frac{Fa^3}{3EI} = \frac{F}{3EI}\left(\frac{G_{Ic}bEI}{F^2}\right)^{\frac{3}{2}}, \tag{B.4}$$

where again $v_1(L) = -v_2(L)$. This solution corresponds to the curved branch of the analytical solution shown in Fig. 4.7. When the interconnection is completely damaged each layer acts individually as a cantilever beam and the tip displacement reads

$$v_2(L) = -v_1(L) = \frac{FL^3}{3EI}, \tag{B.5}$$

which is represented by the second linear branch in the diagram in Fig. 4.7.

B.2   Mode II delamination

Closed-form solution for the mode II delamination is derived for the simply supported beam with a concentrated force at the midspan and an initial crack at the left-hand side as shown in Fig. 4.9. Vertical deflection at the midspan for such a beam before the delamination process has started reads

$$v(L) = v_1(L) = v_2(L) = \frac{F}{96EI}(2L^3 + 3a_0^3), \tag{B.6}$$

where L is half of the length of the beam according to Fig. 4.9, a_0 is the initial crack length and EI is the bending stiffness of one layer of the cracked beam.

In case of ongoing delamination up to the point where the crack reaches the midspan ($a < L$), the strain energy rate equals the difference between the strain energy rates of the beam with a damaged cross-section (bending stiffness $2EI$) and the beam with an undamaged cross-section (bending stiffness $8EI$), which can be written as

$$\mathrm{d}\Phi = \frac{M^2(a)\mathrm{d}a}{2}\left(\frac{1}{2EI} - \frac{1}{8EI}\right) = \frac{3}{16}\frac{M^2(a)\mathrm{d}a}{EI} = \frac{3}{16}\frac{\left(\frac{F}{2}a\right)^2\mathrm{d}a}{EI}. \tag{B.7}$$

When this rate per unit of crack area reaches the critical energy release for mode II delamination the crack will propagate. In this case, therefore,

$$G_{IIc} = \frac{d\Phi}{bda} = \frac{3}{64}\frac{F^2a^2}{bEI}. \tag{B.8}$$

From (B.7) and (B.8), the midspan deflection for ongoing delamination and $a < L$ can be then obtained as

$$v(L) = \frac{F}{96EI}(2L^3 + 3a^3) = \frac{F}{96EI}\left[2L^3 + \frac{(64G_{IIc}bEI)^{\frac{3}{2}}}{\sqrt{3}F^3}\right]. \tag{B.9}$$

This solution is shown as analytical delamination $(a < L)$ in Fig. 4.10.

When $a > L$ the midspan deflection of the beam reads

$$v(L) = \frac{F}{24EI}\left[2L^3 - 6\left(L - \frac{a}{2}\right)^3\right]. \tag{B.10}$$

Since the moment at the crack tip now reads

$$M(a) = \frac{F}{2}a - F(a - L) = F\left(L - \frac{a}{2}\right), \tag{B.11}$$

the strain energy rate as

$$d\Phi = \frac{3}{16}\frac{M^2(a)da}{EI} = \frac{3}{16}\frac{F^2\left(L - \frac{a}{2}\right)^2 da}{EI}, \tag{B.12}$$

and the critical energy release for mode II delamination is

$$G_{IIc} = \frac{d\Phi}{bda} = \frac{3}{16}\frac{F^2\left(L - \frac{a}{2}\right)^2}{bEI}. \tag{B.13}$$

Thus, the midspan deflection for ongoing delamination while $a > L$ is obtained by substituting a from (B.13) in (B.10) eventually giving

$$v(L) = \frac{F}{24EI}\left[2L^3 - \frac{(64G_{IIc}bEI)^{\frac{3}{2}}}{4\sqrt{3}F^3}\right], \tag{B.14}$$

This solution is shown as analytical delamination $(a > L)$ in Fig. 4.10.

When the beam is completely damaged $(a = 2L)$ the midspan deflection reads

$$v(L) = \frac{FL^3}{12EI} \tag{B.15}$$

Bibliography

[1] A. Adekola. Partial interaction between elastically connected elements of a composite beam. *Int. J. Solids Struct.*, 4(11):1125–1135, 1968.

[2] G. Alfano and M. A. Crisfield. Finite element interface models for the delamination analysis of laminated composites: mechanical and computational issues. *Int. J. Numer. Meth. Eng.*, 50(7):1701–1736, 2001.

[3] G. Alfano and M. A. Crisfield. Solution strategies for the delamination analysis based on a combination of local-control arc-length and line searches. *Int. J. Numer. Meth. Eng.*, 58:999–1048, 2003.

[4] M. M. Attard and G. W. Hunt. Sandwich column buckling - a hyperelastic formulation. *Int. J. Solids Struct.*, 45(21):5540–5555, 2008.

[5] J. R. Barber. *Elasticity, 2nd Edition*. Kluwer Academic Publishers, Dordecht, 2004.

[6] J. Bareisis. Stiffness and strength of multilayer beams. *J. Compos. Mater.*, 40(6):515–531, 2006.

[7] G. I. Barenblatt. The formation of equilibrium cracks during brittle fracture - general ideas and hypothesis, axially symmetric cracks. *Prikl. Math. Mekh. (Sec. 12.2)*, 23(3):434–444, 1959.

[8] Z. Bažant and L. Cedolin. *Stability of Structures*. Dover, 2003.

[9] C. V. Campbell. Lamina, laminaset, bed and bedset. *Sedimentology*, 8(1): 7–26, 1967.

[10] E. Carrera, G. Giunta, and M. Petrolo. *Beam Structures: Classical and Advanced Theories*. Wiley, Chichester, England, 2011.

[11] N. Challamel and U. A. Girhammar. Boundary-layer effect in composite beams with interlayer slip. *J. Aerosp. Eng.*, 24:199–209, 2011.

[12] G. R. Cowper. The shear coefficient in Timoshenko's beam theory. *J. Appl. Mech.*, 33(2):335–340, 1966.

[13] M. A. Crisfield. *Non-Linear Finite Element Anaylsis of Solids and Structures*, volume 1. Wiley, Chichester, England, 1996.

[14] G.A.O. Davies, D. Hitchings, and J. Ankersen. Predicting delamination and debonding in modern aerospace composite structures. 66(6):846–854, 2006.

[15] R. de Borst. Numerical aspects of cohesive-zone models. *Eng. Fract. Mech.*, 70(14):1743–1757, 2003.

[16] A. B. de Morais. Novel cohesive beam model for the end-notched flexure (enf) specimen. *Eng. Fract. Mech.*, 78:3017–3029, 2011.

[17] A. B. de Morais. Mode i cohesive zone model for delamination in composite beams. *Eng. Fract. Mech.*, 109:236–245, 2013.

[18] A. Eijo, E. Oñate, and S. Oller. A numerical model of delamination in composite laminated beams using the lrz beam element based on refined zigzag theory. *Composite Structures*, 104:270–280, 2013.

[19] Y. Frostig. Classical and high-order computational models in the analysis of modern sandwich panels. *Compos. Part B-Eng.*, 34:83–100, 2003.

[20] F. Gara, P. Ranzi, and G. Leoni. Displacement-based formulations for composite beams with longitudinal slip and vertical uplift. *Int. J. Numer. Meth. Eng.*, 65:1197–1220, 2006.

[21] U. A. Girhammar and D. H. Pan. Exact static analysis of partially composite beams and beam-columns. *Int. J. Mech. Sci.*, 49:239–255, 2007.

[22] A. A. Griffith. The phenomena of rupture and flow in solids. *Philosophical Transactions of the Royal Society of London*, A 221:163–198, 1921.

[23] C. M. Harvey and S. Wang. Mixed-mode partition theories for one-dimensional delamination in laminated composite beams. *Eng. Fract. Mech.*, 96:737–759, 2012.

[24] H. B. Hellweg and M. A. Crisfield. A new arc-length method for handling sharp snap-backs. *Computers and Structures*, 66(5):705–709, 1998.

[25] A. Hillerborg, M. Modéer, and P. E. Petersson. Analysis of crack formation and crack growth in concrete by means of fracture mechanics and finite elements. *Cement and Concrete Research (Sec. 12.2)*, 6:773–782, 1976.

[26] K. D. Hjelmstad. *Fundamentals of structural mechanics.* Springer-Verlag, New York, 2nd edition, 2005.

[27] T. Hozjan, M. Saje, S. Srpčič, and I. Planinc. Geometrically and materially non-linear analysis of planar composite structures with an interlayer slip. *Comput. Struct.*, 114:1–17, 2013.

[28] H. Irschik and J. Gerstmayr. A continuum mechanics based derivation of reissner's large-displacement finite-strain beam theory: the case of plane deformations of originally straight bernoulli-euler beams. *Acta Mech.*, 206(1-2): 1–21, 2009.

[29] H. Irschik and J. Gerstmayr. A continuum-mechanics interpretation of reissner's non-linear shear-deformable beam theory. *Math. Comp. Mod. Dyn. Syst.*, 17(1):19–29, 2011.

[30] G. Jelenić. Finite element discretisation of 3D solids and 3D beams obtained by constraining the continuum. Technical report, Imperial College London, Department of Aeronautics, Aero Report 2004-01, 2004.

[31] K. S. Kim and N. Aravas. Elastoplastic analysis of the peel test. *International Journal of Solids and Structures*, 24:417–435, 1988.

[32] A. Kroflič, I. Planinc, M. Saje, and B. Čas. Analytical solution of two-layer beam including interlayer slip and uplift. *Struct. Eng. Mech.*, 34(6):667–683, 2010.

[33] A. Kroflič, I. Planinc M. Saje, G. Turk, and B. Čas. Non-linear analysis of two-layer timber beams considering interlayer slip and uplift. *Eng. Struct.*, 32:1617–1630, 2010.

[34] A. Kroflič, M. Saje, and I. Planinc. Non-linear analysis of two-layer beams with interlayer slip and uplift. *Comput. Struct.*, 89(23-24):2414–2424, 2011.

[35] A. Kryžanowski, S. Schnabl, G. Turk, and I. Planinc. Exact slip-buckling analysis of two-layer composite columns. *Int. J. Solids Struct.*, 46:2929–2938, 2009.

[36] N. Lustig. Delamination of plane stress structures using interface elements. *Osnove nelinearne mehanike, Problem sheet no. 2, Faculty of Civil Engineering, University of Rijeka*, 2013.

[37] W. J. McCutheon. Stiffness of framing members with partial composite action. *J. Struct. Eng. - ASCE*, 112(7):1623–1637, 1986.

[38] Y. Mi, M. A. Crisfield, G. A. O. Davies, and H.B. Hellweg. Progressive delamination using interface elements. *Journal of Composite Structures*, 32 (14):1246–1272, 1998.

[39] N. T. Nguyen, D. J. Oehlers, and M. A. Bradford. An analytical model for reinforced concrete beams with bolted side plates accounting for longitudinal and transverse partial interaction. *Int. J. Solids Struct.*, 38:6985–6996, 2001.

[40] R. W. Ogden. *Non-linear Elastic Deformations*. Dover, New York, 1997.

[41] E. Papa and G. Jelenić. Exact solution for 3d timoshenko beam problem using linked interpolation of arbitrary order. *Arch. Appl. Mech.*, 81:171–183, 2011.

[42] E. Papa Dukić, G. Jelenić, and M. Gaćeša. Configuration-dependent interpolation in higher-order 2d beam finite elements. *Finite Elem. Anal. Des.*, 78: 47–61, 2014.

[43] A. Pegoretti, L. Fambri, G. Zappini, and M. Bianchetti. Finite element analysis of a glass fibre reinforced composite endodontic post. *Biomaterials*, 23 (13):2667–2682, 2002.

[44] L. Perko. *Differential equations and dynamical systems*. Springer-Verlag, New York, 3rd edition, 2001.

[45] L. Poorter, L. Bongers, and F. Bongers. Architecture of 54 moist-forest tree species: traits, trade-offs, and functional groups. *Ecology*, 87:1289–1301, 2006.

[46] G. Ranzi, F. Gara, and P. Ansourian. General method of analysis for composite beams with longitudinal and transverse partial interaction. *Comput. Struct.*, 84:2373–2384, 2006.

[47] G. Ranzi, A. Dall'Asta, L. Ragni, and A. Zona. A geometric nonlinear model for composite beams with partial interaction. *Eng. Struct.*, 32:1384–1396, 2010.

[48] E. Reissner. On one-dimensional finite-strain beam theory; the plane problem. *J. Appl. Math. Phys. (ZAMP)*, 23(5):795–804, 1972.

[49] P. Robinson, T. Besant, and D. Hitchings. Delamination growth prediction using a finite element approach. In J.G. Williams and A. Pavon, editors, *Fracture of Polymers, Composites and Adhesives*, pages 135–147. Elsevier, Amsterdam, 2000.

[50] C. H. Roche and M. L. Accorsi. A new finite element for global modelling of delaminations in laminated beams. *Finite Elements in Analysis and Design*, 31:165–177, 1998.

[51] B. V. Sankar. A finite element for modelling delaminations in composite beams. *Computers and Structures*, 38(2):239–246, 1991.

[52] J. C. J. Schellekens and R. De Borst. On the numerical integration of interface elements. *Int. J. Numer. Meth. Eng.*, 36(1):43–66, 1993.

[53] S. Schnabl and I. Planinc. The influence of boundary conditions and axial deformability on buckling behavior of two-layer composite columns with interlayer slip. *Eng. Struct.*, 32(10):3103–3111, 2010.

[54] S. Schnabl and I. Planinc. The effect of transverse shear deformation on the buckling of two-layer composite columns with interlayer slip. *Int. J. Nonlinear Mech.*, 46(3):543–553, 2011.

[55] S. Schnabl and I. Planinc. Exact buckling loads of two-layer composite reissner's columns with interlayer slip and uplift. *Int. J. Solids Struct.*, 50(1): 30–37, 2013.

[56] S. Schnabl, I. Planinc, M. Saje, B. Čas, and G. Turk. An analytical model of layered continuous beams with partial interaction. *Struct. Eng. Mech.*, 22 (3):263–278, 2006.

[57] S. Schnabl, M. Saje, G. Turk, and I. Planinc. Analytical solution of two-layer beam taking into account interlayer slip and shear deformation. *J. Struct. Eng., ASCE*, 133(6):886–894, 2007.

[58] M. Schoenberg and F. Muir. A calculus for finely layered anisotropic media. *Geophysics*, 54(5):581–589, 1989.

[59] J. C. Simo and M. S. Rifai. A class of mixed assumed strain methods and a method of incompatible modes. *Int. J. Num. Meth. Eng.*, 29:1595–1638, 1990.

[60] J. C. Simo and R. L. Taylor. Quasi-incompressible finite elasticity in principal stretches: continuum basis and numerical algorithms. *Comp. Meth. Appl. Mech. Eng.*, 85:273–310, 1991.

[61] J. C. Simo and L. Vu-Quoc. On the dynamics of flexible beams under large overall motions - the plane case: Part i and ii. *J. Appl. Mech.*, 53(4):849–863, 1986.

[62] J. C. Simo and L. Vu-Quoc. A geometrically exact rod model incorporating shear and torsion-warping deformation. *Int. J. Solids Struct.*, 27(3):371–393, 1991.

[63] J. B. M. Sousa Jr. and A. R. da Silva. Analytical and numerical analysis of multilayered beams with interlayer slip. *Eng. Struct.*, 32:1671–1680, 2010.

[64] W. Tan and T. A. Desai. Microscale multilayer cocultures for biomimetic blood vessels. *J. Biomed. Mater. Res. A*, 72A(2):146–160, 2005.

[65] R.T. Tenchev and B.G. Falzon. A correction to the analytical solution of the mixed-mode bending (mmb) problem. *Comp. Sci. Tech.*, 67:662–668, 2007.

[66] S. P. Timoshenko. *Strength of Materials, Part I, Elementary Theory and Problems.* D. Van Nostrand Compan, New York, 2nd edition, 1940.

[67] S. P. Timoshenko and J. N. Goodier. *Theory of Elasticity.* McGraw-Hill, New York, 1951.

[68] A. Turon, C.G. Dávila, P.P. Camanho, and J. Costa. An engineering solution for mesh size effects in the simulation of delamination using cohesive zone models. *Eng. Fract. Mech.*, 74(10):1665–1682, 2007.

[69] K. Yu. Volokh and A. Needleman. Buckling of sandwich beams with compliant interfaces. *Compos. Struct.*, 80:1329–1335, 2002.

[70] P. Šćulac, G. Jelenić, and L. Škec. Kinematics of layered reinforced-concrete planar beam finite elements with embedded transversal cracking. *Int. J. Solids Struct.*, 51:74–92, 2014.

[71] L. Škec and G. Jelenić. Analysis of a geometrically exact multi-layer beam with a rigid interlayer connection. *Acta Mech.*, 225(2):523–541, 2014.

[72] L. Škec, S. Schnabl, I. Planinc, and G. Jelenić. Analytical modelling of multilayer beams with compliant interfaces. *Struct. Eng. Mech.*, 44(4):465–485, 2012.

[73] L. Škec, A. Bjelanović, and G. Jelenić. Glued timber-concrete beams - analytical and numerical models for assesment of composite action. *Eng. Rev.*, 33(1):41–49, 2013.

[74] L. Vu-Quoc and H. Deng. Galerkin projection for geometrically exact sandwich beams allowing for ply drop-off. *J. Appl. Mech.*, 62:479–488, 1995.

[75] L. Vu-Quoc and I. K. Ebcioğlu. General multilayer geometrically-exact beams and 1-d plates with piecewise linear section deformation. *J. Appl. Math. Mech. (ZAMM)*, 76(7):391–409, 1996.

[76] L. Vu-Quoc, H. Deng, and I. K. Ebcioğlu. Multilayer beams: A geometrically exact formulation. *J. Nonlinear Sci.*, 6:239–270, 1996.

[77] S. Wang and C. M. Harvey. Mixed mode partition theories for one dimensional fracture. *Eng. Fract. Mech.*, 79:329–352, 2012.

[78] D. Xie and A. M. Waas. Discrete cohesive zone model for mixed-mode fracture using finite element analysis. *Eng. Fract. Mech.*, 73(13):1783–1796, 2006.

[79] O. C. Zienkiewicz and R. L. Taylor. *The Finite Element Method for Solid and Structural Mechanics.* Butterworth-Heinemann, Oxford, UK, 2005.

[80] O. C. Zienkiewicz, R. L. Taylor, and J. Z. Zhu. *The Finite Element Method. Its Basis & Fundamentals.* Butterworth-Heinemann, Oxford, UK, 2005.